Finite element simulation techniques for incompressible fluid-structure interaction with applications to bio-engineering and optimization

---

Dissertation
zur Erlangung des Grades eines
Doktors der Naturwissenschaften

Der Fakultät für Mathematik der
Technischen Universität Dortmund
vorgelegt von

Mudassar Razzaq

Finite element simulation techniques for nonlinear incompressible fluid-structure interaction with applications to bio-engineering and optimization

Mudassar Razzaq

Dissertation eingereicht am: 16. 02. 2011
Tag der mündlichen Prüfung: 15. 06. 2011

Mitglieder der Prüfungskommission

Prof. Dr. Stefan Turek (1. Gutachter, Betreuer)
Prof. Dr. Heribert Blum (2. Gutachter)
Prof. Dr. Matthias Röger
Prof. Dr. Rudolf Scharlau
Dr. Abderrahim Ouazzi

Abstract

Numerical techniques for solving the problem of fluid-structure interaction with an elastic material in a laminar incompressible viscous flow are described. An Arbitrary Lagrangian-Eulerian (ALE) formulation is employed in a fully coupled monolithic way, considering the problem as one continuum. The mathematical description and the numerical schemes are designed in such a way that more complicated constitutive relations (and more realistic for biomechanics applications) for the fluid as well as the structural part can be easily incorporated. We utilize the well-known Q_2P_1 finite element pair for discretization in space to gain high accuracy and perform as time-stepping the 2nd order Crank-Nicholson, resp., Fractional-Step-θ-scheme for both solid and fluid parts. The resulting nonlinear discretized algebraic system is solved by a Newton method which approximates the Jacobian matrices by a divided differences approach, and the resulting linear systems are solved by iterative solvers, preferably of Krylov-multigrid type.

For validation and evaluation of the accuracy of the proposed methodology, we present corresponding results for a new set of FSI benchmarking configurations which describe the self-induced elastic deformation of a beam attached to a cylinder in laminar channel flow, allowing stationary as well as periodically oscillating deformations. Then, as an example for fluid-structure interaction (FSI) in biomedical problems, the influence of endovascular stent implantation onto cerebral aneurysm hemodynamics is numerically investigated. The aim is to study the interaction of the elastic walls of the aneurysm with the geometrical shape of the implanted stent structure for prototypical 2D configurations. This study can be seen as a basic step towards the understanding of the resulting complex flow phenomena so that in future aneurysm rupture shall be suppressed by an optimal setting for the implanted stent geometry.

Keywords: Fluid-structure interaction (FSI), monolithic FEM, ALE, multigrid, incompressible laminar flow, bio-engineering, optimization, benchmarking.

To my son
Zoizz Mudassar

Acknowledgments

I am sincerely grateful to my supervisor Prof. Dr. Stefan Turek, for his support, encourage, and motivation throughout my research work which enabled me to develop an understanding of the subject. As my teacher and mentor, he guided me into the wonderful world of scientific research. I am greatly indebted for his availability, inspiration, criticism and optimism while keeping an enjoyable working atmosphere. His professional and editorial advice was essential to the completion of this thesis. I thank him for sharing with me his unstoppable taste for turning ideas into practical innovations.

I would like to express my appreciation to my co-advisor Dr. J. Hron. I feel very fortunate to work closely with him. He paved the way for me during the initial phase of my PhD studies to deepen my understanding of the monolithic Arbitrary Lagrangian Eulerian (ALE) formulation of the Fluid-Structure Interaction (FSI) problems and implementation of the numerical techniques to treat the problems.

Reflecting back on this enjoyable and painful PhD journey, my experience at TU Dortmund would not have been such a pleasurable one without the presence of all the people working here. I would like to express my heartiest regards and blessings to people like S. Buijssen, C. Becker for administrative support, M. A. Kashid, O. Scherbinina, R. Mahmood, E. Bayraktar, and M. Nickeean for sharing and bearing me in same room time to time and all those people who helped, supported and accompanied. I would also like to thank Dr. D. Kuzmin and Dr M. Möller for offering series of lecture on CFD related topics and their availability and willingness for discussions. My thanks will go also to Dr. A. Ouazzi who shared wonderful thoughts on almost all topics radiantly.

No one has been more important to me in the pursuit of my degree than my family. I am unable to find appropriate words to say thanks to my parents. They emphasized, took care and provided an atmosphere so that I can spent my time on education and sports equally. They are always with me in every endeavor. Especially, my wife and sweet son Zoizz, who make my each day worthwhile, without their love and patience it would have been much harder to keep up the motivation to finish this thesis.

Finally, I would like to express my gratitude to the Higher Education Commission (HEC) of Pakistan for providing the funding and the German Research Association (DFG), funding the project as part of FOR493 and TRR30, for their financial support of the work.

Dortmund, February 15, 2011

Mudassar Razzaq

Contents

Tell me and I will forget. Show me, and I may not remember. Involve me, and I will understand.

-Native American Saying

1

Introduction

This chapter is the foundation of this thesis. It introduces and motivates the broad context of the importance of the research and series of problems in the area of Fluid-Structure Interaction (FSI). It will establish and highlight the grounding for the next chapters. A birds eye view of the research contributions and the overall organization of this thesis will be given towards the end of the chapter.

1.1 Orientation

Fluid flows encounters in everyday life from the time of existence of mankind and even beyond. Blood, water are the one of the main source of existence of human being and other living creatures. Approximately, a human body contains 55-60% of water in adult male and female. Also, two third of the very own Earth consist of water. Water is the simplest and without shadow of doubt most important fluid which is categorized as Newtonian fluid that means its stress depends linearly on the deformation rate with a constant velocity.

The fluid mechanics is the branch of science which discusses the fluid flow behavior, governed by Partial Differential Equations (PDE) which represent conservation laws for the mass, momentum and energy. With the invent of digital computers, Computational Fluid Dynamics (CFD) came into existence which is an art of replacing such PDE systems by sets of algebraic equations and solve them numerically with appropriate numerical methods.

Structural mechanics is another discipline of Engineering in which the deformation or displacement of solid materials are analytically studied and material laws and a wide range of dynamical properties modeled. Moreover, the computational structural mechanics (CSM) has also achieved a great advance independently from the CFD.

In almost every physical system, interactions between movable or deformable structures with internal or external fluid flow can be observed. This behavior is known in literature as fluid-structure interaction (FSI) and has been one of the most investigated and most intensively studied coupled problems. Many examples of this multi-field/multi-physics phenomena can be found in practice which is an actual main focus in CFD development. In this undertaken research special cases of coupled problem will be investigated,- the fluid-structure interaction (FSI) problems.

The combined solution of fluid structure interaction problems demands extraordinary efforts as it is schematically shown in Figure. 1.1

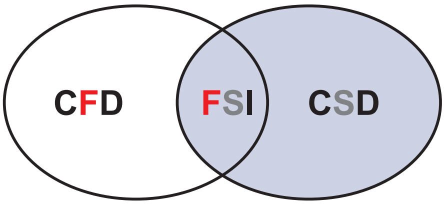

Figure 1.1: FSI problem - lies in between the fluid (CFD) and structural (CSD) dynamics problems

This thesis has only one author, which is common for a PhD thesis, and the author decided to address reader as using first person plural ”we” over first person singular ”I” for humility. If the presented contributed results are jointly compiled then ”we” indicates a group of authors, otherwise explicitly stated.

Almost all the calculations made for the formulated fluid structure interaction (FSI) system of equations in this thesis were performed using the Finite Element Method (FEM) package Featflow (Finite element analysis tool for flow problems). A comprehensive survey, a complete introduction and rigorous guide to this open source software can be found and downloaded at **`http:/www.featflow.de`**.

1.2 Research Applications and Goals

In recent years, encouraging progress has been made in the numerical simulation of Fluid-Structure Interaction (FSI) problems and continue to be the focus of much attention. The significant applications in various areas considering an elastic or inelastic structure surrounded by or conveying a fluid can be found in the following broad engineering disciplines:

- Aerodynamics
- Aeroelasticity
- Civil engineering
- Biomechanics
- Hemodynamics
- Meteorological phenomena
- Hydroelasticity

Such multi-physics problems ranging from water penetration of off-shore structures, modeling submarines motion, parachute modeling, interaction of the various objects with the surroundings (air, water, structures), blood flow in arteries, environmental hazards, airfoil fluttering, rain, wind, floods involve more than one physical effect.

Fluid Structure Interaction problems, involving the coupling of unsteady fluid flow and structure motion, arise in many fields of engineering, as well as in many other sciences, e.g. medicine. From previous experience one can conclude that the mechanisms which lead the vibrations of flexible structures immersed in flowing fluids to become self-excited are very sensitive to the mechanical properties of the structure as well as to the properties of the incoming fluid and very difficult to predict.

One major application is blood flow through human arteries (flow through the heart flaps, flow in the heart chambers). The local hemodynamics, and temporal wall shear stress gradient is important in understanding the mechanisms leading to various complications in cardiovascular function. Many clinical treatments can be studied in detail only if a reliable model describing the response of arterial walls to the pulsatile blood flow is considered [51].

The multigrid FSI simulation to calculate for Fluid-Structure Interaction Optimization is another application. Often we have an optimization problem under the constraint of a strong fluid-structure coupling. This state - consisting of velocity, pressure and deformation - shall be achieved by the optimal control of a certain part of the FSI system. Possible values that may be influenced are the material of the elastic solid or a certain inflow control on a part of the outer boundary. Although this advancement makes it possible to consider the optimization of FSI based systems, the development of efficient simulation-based optimization techniques for the optimal design of FSI systems is still in its beginning stage.

In this research work we seek to validate and evaluate the accuracy and performance of the proposed methodology, for a new set of FSI benchmark configurations which describe the self-induced elastic deformation of a beam attached to a cylinder in laminar channel flow, allowing stationary as well as periodically oscillating deformations and compare the results with experimental values from a corresponding benchmarking experiment.

Additionally, this benchmarking scenario is to extend the validated FSI benchmark configurations to optimization problems such that minimal drag/lift values of the elastic object, minimal pressure loss or minimal non-stationary oscillations through boundary control of the inflow, change of geometry or optimal control of volume forces can be reached. The main design aim for the presented fluid structure interaction optimization problem is to minimize the lift on the beam with the help of boundary control of inflow data. The simulation is based on the described FSI1 configuration. Then, as an example of FSI in biomedical problems, the influence of endovascular stent implantation onto cerebral aneurysm hemodynamics is numerically investigated. The aim is to study the interaction of the elastic walls of the aneurysm with the geometrical shape of the implanted stent structure for prototypical 2D configurations, propose corresponding more realistic material law for vessels and put into action the nonlinear flow model (power-law) and analysis with emphasis on hemodynamical applications aneurysm successfully. This study can be seen as a basic step towards the understanding of the resulting complex flow phenomena so that in future aneurysm rupture shall be suppressed by an optimal setting for the implanted stent geometry.

Hence, the action of the dynamic fluid forces on the elastic/inelastic boundaries and the deformation of the flow domain caused by the structural displacements are modeled. The structure is made of an isotropic elastic material, where linear and geometrically nonlinear models are used for small and finite deformations, respectively.

1.3 Challenges and Motivation

Fluid-structure interaction physical processes are very complex, nonlinear in nature and can not be solved analytically. In fact experimental setups are essential to provide reliable data. However, these are generally associated with enormous costs, which is why the demand for numerical simulations as development tool is increasing rapidly.

Both problems of viscous fluid flow and of elastic body deformation have been studied separately for many years in great detail. But there are many problems encountered in real life where an interaction between those two medias is of great importance.

In bioengineering, modeling FSI in the blood circulatory system is a vast and complex mathematical subject; even a simplified description of the vessel wall mechanics assuming homogeneous linearly elastic behavior leads to complicated numerical strategies with challenging stability and convergence properties. To devise an accurate model for the mechanical behavior of arterial walls that will lead to numerical methods producing computational solutions in an acceptable time is more complicated without introducing simplifications. There have been several different approaches to the problem of fluid-structure interaction in blood flow dynamics in local arterial environments and to predict vessel wall deformation. Arterial walls are anisotropic and heterogeneous, composed of layers with different biomechanical characteristics [51], [78], [105]. A variety of different models has been suggested in the literature to model the mechanical behavior of arteries [4], [3], [9], [51],[78], [105], [132]. They range from the detailed description of each of the layers to the average description of the total mechanical response of the vessel wall assuming homogeneous, linearly elastic behavior, special geometry, symmetry and periodicity.

Similarly, typical cases are the areas of biomedical fluids which include the influence of hemodynamic factors in blood vessels, cerebral aneurysm hemodynamics and blood flow interaction with elastic veins [2, 129, 46]. A fluid-structure model with the wall modeled as a thin shell was used to model the left heart ventricle, and similarly, to model the flow in collapsible tubes in [32, 33, 105, 103, 68, 69]. In reality the thickness of the wall can be significant and very important and it is very hard to predict the material property of wall thickness. For example in arteries the wall thickness can be up to 30% of the diameter and its local thickening can be the cause of an aneurysm creation. In this thesis, we allow the walls of the aneurysm to be elastic and hence deforming with the flow field in the vessel. Moreover, we examine several configurations for stent geometries which clearly influence the flow behavior inside of the aneurysm such that a very different elastic displacement of the walls is observed, too. We demonstrate that either the elastic modeling of the aneurysm walls as well as the proper description of the geometrical details of the shape of the aneurysm and particularly of the stents is of great importance if the complex interaction between structure and fluid shall be quantitatively analyzed, especially with more realistic blood flow models and anisotropic constitutive laws of the elastic walls. In this study, we restrict at the moment to 2D prototypical numerical studies of aneurysm configurations which is due to an easier presentation and the computational time needed to solve the problem. In all these cases we have to deal with large deformations of a deformable solid interacting with an unsteady, often periodic, fluid flow.

With the continuous increase of processing power of computers, these problems have attracted more and more interest of the researchers. However, either the experimental setting is too complicated for the computational tool or the numerical setting is not feasible for experiment. There are still challenging questions in FSI research, ranging from mathematical modeling, numerical discretization up to implementation into software tools. Increased efforts in numerical research and development are presently being observed to develop models and coupling strategies.

1.4 Research Methodology

In the past decades the computational fluid dynamics (CFD) has developed many efficient methods which provide a qualitative (and some time even quantitative) numerical solution of various fluid dynamics problems. Many commercial programs have been created, tested on benchmark settings and successfully applied to diverse complex fluid dynamics problems. Traditionally, the governing equations have been derived using Eulerian (spatial) description. In literature, from a numerical point of view the finite volume discretization has been preferred because of its conservative properties. Similarly finite element discretization methods are equally utilized.

Many structural dynamics solvers have been developed to solve various structural dynamics phenomenon. The modeling of a wide range of material laws and structural properties has been made possible by creating special finite elements holding desired features. Contrarily to the fluid dynamics, the Lagrangian (material) description has been selected for the governing equations.

The possibilities of numerical solution of the coupled FSI problem include the numerical solutions of the fluid and the structural parts by partitioned or monolithic way. In the case of their combination some mixed description (usually referred to as the Arbitrary Lagrangian-Eulerian description or ALE) has been used which brings additional nonlinearity into the resulting equations. The development of tools for modeling various fluid-structure interaction problems is still an uphill challenge.

Fluid-structure interaction problems solving approaches can be divided into weakly (separated) and strongly coupled approaches, based on the their data exchange.

In the separated coupling approach, the coupled problem is partitioned into fluid and structural parts and then solved separately. The partitioned analysis of coupled systems has been introduced by Park and Fellipa [100].

Contrarily, in a strongly coupled strategies both parts of the FSI problem are solved monolithically. That means, one system of equations is arrived after discretizing the governing fluid and structural equations and taking into account the boundary conditions on the interface. Hence, the whole FSI problem is solved at once using a monolithic ALE approach.

Obviously, both approaches have advantages and disadvantages. In Figure 1.4, they are referred with regard to their flexibility and stability as well as the needed programming robustness.

One solution strategy is to decouple the problem into the fluid part and structure part, which is known as separated or partitioned approach. The main advantage of the separated coupling approach is that for each of those parts it uses some well established, efficient and well validated finite element based numerical method of solution and the interaction is introduced as external boundary conditions or volume forces in each of

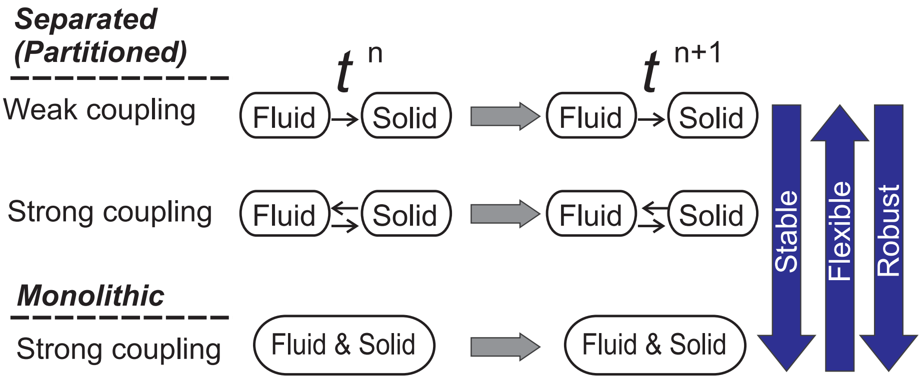

Figure 1.2: Coupling strategies for multi-physics FSI problems

the subproblems. The drawback of a partitioned approach is that the treatment of the interface and the interaction is often problematic. Although they are flexible, less programming efforts required but due to the explicit nature of this coupling convergence problems may often arise. Consequently, there is a restriction on the choice of the time-step even if implicit time-stepping schemes are used by the two solvers.

Contrarily, the strong coupling approaches are more difficult to formulate and to program. Normally, the simultaneous solution of the whole FSI problem necessitates reformulation of the systems of equations and confines the choice of the numerical methods to be applied. Additionally, special approaches may be needed for modeling the nonlinearities in each of the physical parts. Valuable programming efforts are required to create and validate a program applicable to wide range of problems. However, there are no approximation errors and convergence problems in this approach due to the data convey between the fluid and structural parts.

The approach which will be put into action in the present study is a monolithic strong coupling strategy. This considered strong coupling strategy of an implicit type is more stable although difficult to program than the separated coupling approach that is more flexible but connected with convergence problems. With regard to flexibility we opted for stability and robustness, it seems to be a good compromise between the separated and the strong coupling approaches.

In this thesis, we investigated and developed a new numerical techniques for solving the problem of fluid structure interaction of a compressible/incompressible elastic material in a laminar incompressible viscous flow in a fully coupled monolithic way. We formulated the implicit set of equations via Arbitrary Lagrangian-Eulerian (ALE) approach. We discretized the flow problem in two space dimensions by utilizing the high order finite element Q_2 (Taylor-Hood family) for velocity $\mathbf{V}$ and displacement $\mathbf{U}$ approximation and P_1 element for the pressure p approximation to maintain high accuracy, in a standard FEM approach, after applying a standard implicit one-step time-stepping schemes in the non-stationary case. The used Q_2P_1 element pair satisfies the well known LBB-stability condition.

It is found evident by an example of FSI benchmark that this element pair has acceptable grid independent results for steady state as well as for oscillatory benchmark cases.

For instance, for $Re = 20$, it is shown in Figure. 1.4.

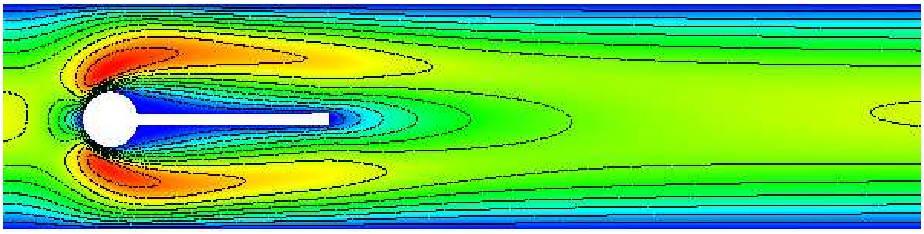

Figure 1.3: FSI Benchmark: $Re = 20$, drag= 14.2943, lift= 0.76375

The resulting discrete nonlinear system for the triplet $(\mathbf{U}, \mathbf{V}, p)$ is solved by utilizing outer quasi-Newton iterations using the line search also known as the method of Rothe (method of lines, or method of semi discretization) [83] in a fully coupled monolithic way. This technique is considered as the most robust iteration technique which may give quadratic convergence. Due to finite element method, the sparsity pattern of the Jacobian matrix is known in advance and computed by divided difference approach.

Inside one Newton step, the solution of the linear subsystem is the most time consuming part of the solution process in terms of the CPU time [122, 128]. One choice for this sparse systems is to put into action a direct solver like UMFPACK [40]. This choice provides very robust linear solvers but its memory and CPU time requirements are too high for larger systems, for instance it allows nearly $20,0000$ unknowns in acceptable time.

Similarly, large linear subproblems can be solved by Krylov-space methods (BiCGStab, GMRes [8]) with suitable preconditioners. One possibility is the ILU preconditioner with special treatment of the saddle point character of our system, where we allow certain fill-in for the zero diagonal blocks [22].

As an alternative, we also utilize a standard geometric multigrid approach based on a hierarchy of grids obtained by successive regular refinement of a given coarse mesh. The complete multigrid iteration is performed in the standard defect-correction setup with the V or F-type cycle. While a direct sparse solver [40] is used for the coarse grid solution, on finer levels a fixed number (2 or 4) of iterations by local MPSC schemes (Vanka-like smoother) [122, 130, 75] with canonical grid transfer routines is put into action which results in high efficiency and robustness. The mathematical description and the numerical schemes are designed in such a way that more complicated constitutive relations can be easily incorporated. We perform numerical comparisons for different time stepping schemes, like the well known classical Fractional step θ-scheme, Backward Euler and Crank Nicholson schemes for fluid structure interaction.

1.5 Summary of Contributions

The scientific research flourishes only by group efforts. Importantly, without the joint work within the Featflow group most of the publications would not have been possible at all. So, to begin with this section, the author pays gratitude to all collaborators, co-authors and their contribution is gratefully acknowledged.

During the pursuit of this thesis, the author has published and contributed to a number of peer reviewed book chapters and intermediate results have been presented at international conferences and published in peer-reviewed proceeding volume and is been in review for journal publication.

We contributed results for the special benchmark settings for fluid-structure interaction problems which have been initiated and developed as collaborative project in the DFG Research Unit 493 formed by group of universities at Germany. The results are already published in [124, 125]. Also, the complete descriptions, the parameter settings and simulation results can be found in [124, 125, 123] and downloaded from `http:/www.featflow.de/en/fsi_benchmark.html`.

Our first journal article has been accepted for publication [108]. A chapter in the textbook titled ”Advances in Mathematical Fluid Mechanics” has been published in late 2010 [109], co-written by Dr. Jaroslav Hron and Prof. Dr. Stefan Turek. In this paper, we present numerical studies on different mesh types. Numerical results are provided for all time stepping schemes which show very reproducible symmetrical two–dimensional swiveling motions. These numerical tests show that the solution is independent of the mesh type and mesh refinement level. Preliminary results for the experimental benchmark configuration are shown to see the qualitative behavior of the elastic beam for a high velocity profile fluid.

Another paper as a chapter, in the textbook titled ”Fundamental Trends in Fluid-Structure Interaction” is published [111], which centers around the use of Arbitrary Lagrangian Eulerian formulation in the numerical context. As an application, the influence of endovascular stent implantation onto cerebral aneurysm hydrodynamics is investigated. This chapter has been co-written by Dr. Jaroslav Hron and Prof. Dr. Stefan Turek.

One paper titled ”Numerical simulation of fluid-structure interaction with application to aneurysm hemodynamics” is published in international conference proceeding for ”Fluid-Structure Interaction. Theory, Numerics and Applications” [110].

Additionally, we proposed and contributed a numerical benchmark scenario titled ”A numerical set-up for benchmarking and optimization of fluid-structure interaction” and provided all the data to validate codes to a Design Test Case Database workshop `http://jucri.jyu.fi` initiated by the university of Jyväskylä, Finland. Annual participations have been made.

1.6 Thesis Outline

Each chapter begins with a self introduction. Moreover, the contents of the thesis are organized as follows.

Chapter 2 will present the mathematical description and modeling of the multi physical phenomena depicting the fluid structure interaction (FSI) with all necessary theoretical descriptions and mathematical formulas. This chapter will provide a conceptual background that will enable the reader to understand and appreciate the contributions described in the remaining chapters. It will also gives a comprehensive overview over the basic principles of continuum mechanics needed for the mathematical description of a monolithic-ALE formulation.

Chapter 3 will discuss and suggest the FEM, time discretization aspects for the system of equations arise for the FSI modeling in a monolithic way. Besides suggesting the methodology of solution, a brief overview of the mathematical preliminaries, simulation environment, will expound upon implementation of the method. It will also discuss the FEM discretization related issues comprehensively to the problem and in general.

Chapter 4 will design the monolithic numerical scheme and implement it to the highly nonlinear FSI problem in a way that several realistic complicated constitutive relations will be used. It will explain the aspects of nonlinear as well as linear solvers in respect of their efficiency and robustness. It will also provide insight to the iterative solvers like Krylov-subspace solver and multigrid solver in general as well as specific to the problem undertaken.

Chapter 5 will be divided into three sections. The section 1 presents the simulation results to the governing saddle point system for the FSI benchmark settings successfully in respect of efficiency and robustness. The second part discusses the experiment benchmark flow and shows agreeable results. The numerical results and conclusions for aneurysm hemodynamics applications are presented at the end. The objective of this chapter is to give a consistent and clear description of the methods to make a reproduction of the simulation results possible for the benchmark settings.

Chapter 6 will extend the FSI benchmark scenario given in chapter 5, into the topic of utmost importance, optimization. It is employed to the optimization of fluid structure interaction problem, at the moment only for stationary case and we are in search for applying for the non-stationary case in the for seen future. This chapter will address the important issue of optimization in the realm of FSI.

Chapter 7 is the concluding chapter presenting a brief commentary on the impact of the various contributions and will provide a collective overview of the general advantages presented by them in the overall studies of the FSI in different techniques. It will give directions for future research initiatives by highlighting some of the open key issues. The conclusions will be drawn and recommendations will be made for future work at the end.

Part I

A Monolithic ALE-FEM Fluid-Structure Interaction Solver

The very ink with which history is written is merely fluid prejudice.

Mark Twain

2

Mathematical Modeling

Every physical occurrence can be presented mathematically for further studies. To start with, this chapter will present mandatory mathematical preliminaries and basic principles of continuum mechanics needed for the mathematical description of fluid flows and its interaction with the solid, namely fluid structure interaction, a multi-physics discipline. The necessary theoretical background that will enable the reader to appreciate the work will be presented before hand. The formulation of the physical problem, small details about Eulerian, Lagrangian descriptions, then the very own used Arbitrary Lagrangian Eulerian (in short ALE) description is formulated for the FSI problem, followed by the necessary constitutive equations.

2.1 Overview

In this work, the problem of viscous fluid flow interacting with an elastic body which is being deformed by the fluid action is considered. Such a problem is encountered in many real life applications of great importance. Typical examples of this type of problem are the areas of biomedical fluids which include the influence of hemodynamic factors in blood vessels, cerebral aneurysm hemodynamics, joint lubrication and deformable cartilage and blood flow interaction with elastic veins [2, 129, 46, 119, 120]. A fluid-structure model with the wall modeled as a thin shell was used to model the left heart ventricle and, similarly, to model the flow in collapsible tubes in [32, 33, 105, 103, 68, 69].

At present there is no analytical result proving well-posedness of the fluid-structure interaction between a viscous incompressible Newtonian fluid and a hyperelastic material or structure problem without assuming additional simplifying assumptions, such as the smallness of the data, periodic boundary conditions, rigidity in elastic shells or plates [131, 63, 24, 30, 34]. Thus, the well-posedness of the fluid-structure interaction of blood flow conveying to (elastic or viscoelastic) arteries is still an open problem even with these simplifications.

In [61] the well-posedness of an unsteady fluid-structure interaction between a viscous incompressible Newtonian fluid modelled by the Navier-Stokes equations and a viscoelastic structure problem is studied. They consider a structure as a collection of rigid moving bodies and fluid domain depends on time and is defined by the position of the structure.

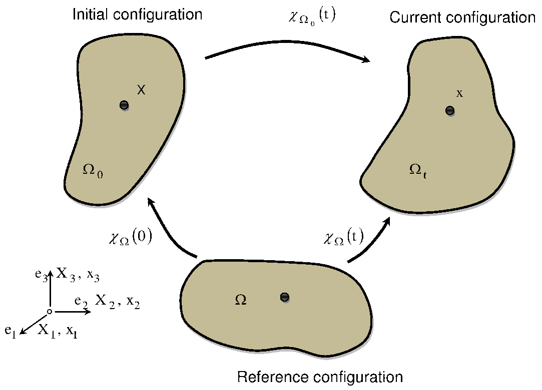

Figure 2.1: Sketch of the referential domain Ω, initial Ω_0 and current state Ω_t and relations between them. The identification $\Omega \equiv \Omega_0$ is adopted in this text.

The important basic ideas, kinematic definitions are not invented rather presented in this chapter, are based on [87, 71, 72, 43, 42, 90, 98]. For basic introduction and complete reference of continuum theory see [64, 121, 67]. Its application in biomechanics are presented in [51] for example. We will mention in the following sections the basic continuum theory related to the work presented in this thesis and setup used in this work.

2.2 Continuum Theory

In continuum mechanics, we are interested in material bodies that can undergo motions and deformations regardless of mass and force. We use the method of continuum mechanics as a powerful and effective tool to explain various physical phenomena successfully without detailed knowledge of the complexity of their internal (micro) structure. Of course prediction based on macroscopic studies are not exact but good enough for the design of machine elements in engineering. The basic ingredients of continuum mechanics, the study of motion and deformation (kinematics), stress, and fundamental physical laws governing the motion of a continuum (balance laws) are presented in the similar order based on [29, 64].

2.2.1 Kinematic Descriptions

Let $\Omega \subset \mathbb{R}^3$ be a reference (undeformed) configuration of a given body, possibly an abstract one. Let $\Omega_t \subset \mathbb{R}^3$ be a current (deformed) configuration of this body at time t. Then there is a one-to-one, uniquely invertible, sufficiently smooth[1] mapping χ_Ω of the reference (undeformed) configuration Ω to the current (deformed) configuration

$$\chi_\Omega : \Omega \times [0,T] \mapsto \Omega_t,$$

---

[1] The mapping χ_Ω continuously differentiable in all variables up to their second derivative included.

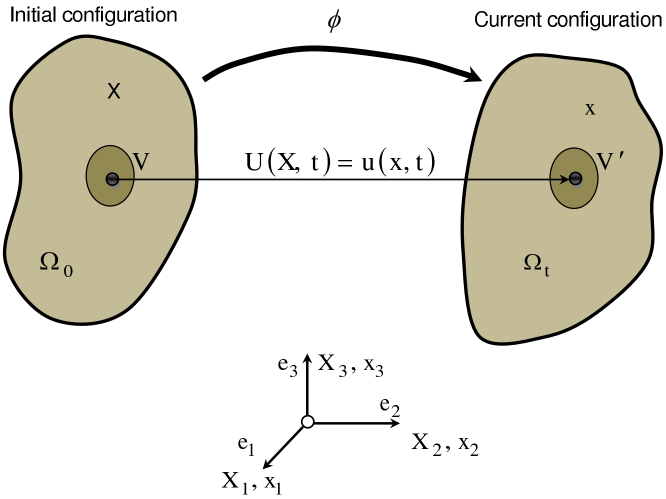

Figure 2.2: Displacement field **U** and **u** of a typical particles.

which determines the successive position of the material point, see Figure. 2.6. For our current purposes it suffices to define one reference configuration for the material point, so in further we drop the subscript Ω_0 and it will be understood that the mapping χ_Ω depends on the choice of the reference configuration Ω which can be fixed in a various ways. Here we think of Ω to be the initial (stress-free) configuration. If we denote by $\mathbf{X}$ to identify an arbitrary material point in the reference configuration Ω then the position of this point at time t is given by

$$\mathbf{x} = \chi(\mathbf{X}, t) \qquad \mathbf{X} \in \Omega,$$

where $\mathbf{x}$ is the position vector of the point in Ω_t. The mapping χ_Ω is called the deformation from Ω to Ω_t. The inverse of this one-to-one, invertible mapping χ is written as

$$\mathbf{X} = \chi^{-1}(\mathbf{x}, t) \qquad \mathbf{x} \in \Omega_t.$$

Now, the displacements vector fields in the material and spatial descriptions respectively are defined as

$$\mathbf{U}(\mathbf{X}, t) = \chi(\mathbf{X}, t) - \mathbf{X} \qquad \chi(\mathbf{X}, t) = \mathbf{U}(\mathbf{X}, t) + \mathbf{X} \tag{2.1}$$

$$\mathbf{u}(\mathbf{x}, t) = \mathbf{x} - \chi(\mathbf{x}, t) \qquad \chi(\mathbf{x}, t) = \mathbf{u}(\mathbf{x}, t) + \mathbf{x} \tag{2.2}$$

where $\mathbf{U}(\mathbf{X}, t)$ represents the displacement field of a material particle and relates its position $\mathbf{X}$ in the undeformed configuration to its position $\mathbf{x}$ in the deformed configuration at time t for all particles (illustrated in Figure 2.2), and $\mathbf{u}(\mathbf{X}, t)$ is the displacement field. $\mathbf{u}(\mathbf{x}, t)$ is a function of referential position $\mathbf{x}$ and time t, which characterizes the material description (Lagrangian form) of the displacement field. These two relations are related by

$$\mathbf{U}(\mathbf{X}, t) = \mathbf{U}[(\chi^{-\mathbf{1}}(\mathbf{X}, t), t)] = \mathbf{u}(\mathbf{x}, t),$$

It is worth mentioning that, in solid mechanics the motion and the deformation of a continuum body are, in general, described in terms of the displacement field. However, the primary field quantities in fluid mechanics describing the fundamental kinematic properties are the velocity field and the acceleration field. The velocity and acceleration fields are defined as the time derivative of the position, keeping $\mathbf{X}$ fixed which are given below respectively:

$$\mathbf{v} = \frac{\partial \chi}{\partial t}, \qquad \mathbf{a} = \frac{\partial^2 \chi}{\partial t^2}.$$

Configurations

This study is concerned with the mechanics of a body in which both mass and volume are continuous (or at least piecewise continuous) functions of continuum particles. Such a body is called continuum body or just continuum. A continuum geometrical region can be determined uniquely. The region Ω_0 with fixed particle $\mathbf{X}$ corresponds to fixed (initial) reference at time $t = 0$. The region Ω is referred to as (undeformed) fixed reference configurations of the body $\mathscr{B}$. Upper case level is employed for reference (undeformed/Lagrangian/material) configuration and lower case for current (deformed/Eulerian/spatial) configuration. Macroscopic materials are the main interest in this study.

The **Eulerian** (or spatial) description is well suited for a problem of fluid flowing through some spatially fixed region. In such a case the material particles can enter and leave the region of interest. The fundamental quantity describing the motion is the velocity vector.

On the other hand the **Lagrangian** (or referential) description is well suited for a problem of deforming a given body consisting of a fixed set of material particles. In this case the actual boundary of the body can change its shape. The fundamental quantity describing the motion in this case is the vector of displacement from the referential state. The transformations between material and spatial regions are typically called push forward and pull back operations. The **push forward** means transformation from reference to current configuration and **pull back** known as transformation from current to reference configuration.

Eulerian Description

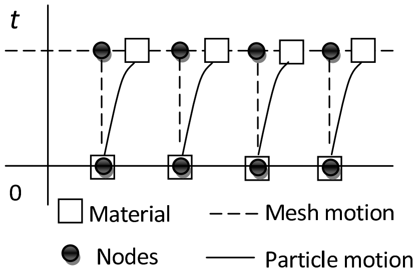

Figure 2.3: Eulerian description-1D

In the Eulerian description mesh nodes are fixed and the continuum moves relative to the mesh. Material particles move with continuum to different positions with velocity over continuum and occupied different position at different time but nodes remain at their original positions, (the 1D situation is sketched in Figure 2.3). This approach is widely used in fluid mechanics because it makes it possible to handle very strong deformation and it can be used for any discretization techniques like finite differences , finite volume, finite element in space. The structured as well as unstructured meshes can be used. However, it is easier to use structured mesh because of fixed nodes and there is no cost for moving the mesh this makes it very attractive approach. It is mainly applied to simulate compressible, turbulent fluid flows. It is simple, robust but on the other hand one need to dealt with imprecise interface and numerical instability for the connective terms.

Now, let us adopt following useful notations for some derivatives in the Eulerian description. Any field quantity φ with values in some vector space Y (i.e. scalar, vector or tensor valued) can be expressed as a function of the spatial position $\mathbf{x} \in \mathbb{R}^3$

$$\varphi = \tilde{\varphi}(\mathbf{x}, t) : \Omega_t \times [0, T] \mapsto Y.$$

Then we define following notations for the derivatives of the field φ

$$\begin{aligned} \frac{\partial \varphi}{\partial t} &:= \frac{\partial \tilde{\varphi}}{\partial t}, \\ \nabla \varphi = \frac{\partial \varphi}{\partial \mathbf{x}} &:= \frac{\partial \tilde{\varphi}}{\partial \mathbf{x}}. \end{aligned}$$

Lagrangian Description

In the Lagrangian description mesh nodes follow the motion of material particles coordinates, i.e. mesh nodes are connected to same material point permanently. It is mainly used in the structural mechanics. Discretization is done widely by finite element methods.
The main application of this description is to study the vehicle crash tests and metal formation processes. Easy tracking of free surfaces and interfaces between different material is possible. However, Inability to handle strong deformations which results in mesh tangling, frequent re-meshing required, expensive projection of data needed and loss of accuracy often arise.

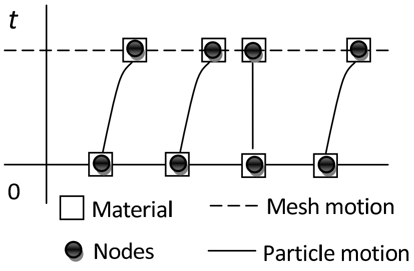

Figure 2.4: Lagrangian description-1D

In the case of Lagrangian description we consider the quantity φ to be defined on the reference configuration Ω, then for any $\mathbf{X} \in \Omega$ we can express the quantity φ as

$$\varphi = \overline{\varphi}(\mathbf{X}, t) : \Omega \times [0, T] \mapsto Y,$$

and we define the derivatives of the field φ as

$$\frac{d\varphi}{dt} := \frac{\partial \overline{\varphi}}{\partial t}, \tag{2.3}$$

$$\operatorname{Grad} \varphi = \frac{\partial \varphi}{\partial \mathbf{X}} := \frac{\partial \overline{\varphi}}{\partial \mathbf{X}}. \tag{2.4}$$

Since the material particle coincide with the same mesh nodes when motion takes place. In Lagrangian description there is no convective effects which means material derivative becomes a simple time derivative 2.3. A history of orientation of motion is intact in this description (see [21] for deeper understandings).

Arbitrary Lagrangian Eulerian Description

The Arbitrary Lagrangian Eulerian description is a more general description that embeds the advantages of the two description documented before. In this description, mesh nodes may be fixed or move in prescribed fashion (with the continuum or relative to continuum) but mesh is allowed to move independently. After each time step the mesh is updated and, in the spirit of the updated Lagrangian description i.e. $\Omega = \Omega(t^n)$, the finite element solution is performed using the current or most recent mesh configuration (see for details [118]).

The Arbitrary Lagrangian Eulerian description was first introduced by Noh [96] addressing the hydrodynamics problem in the finite difference context. The method was also used by Hert et al. [70], Pracht [102] in the finite difference analysis. It was later adopted and developed in finite element format for fluid-structure interaction and for free surface flow problems by Belyteschko [14, 12, 15, 17, 16, 13], Donea [43, 42], Hughes [76, 77], Liu [90, 89] and their companions. More recently, the ALE concepts was applied to nonlinear solid mechanics and contact problems by Haber [65], Liu et al. [88] Benson [18], Ghosh and Kikuchi [54] and others. This approach is well suited for problems with fluid-fluid, fluid-solid, solid-solid interaction. As we know that Eulerian methods work well for fluid mechanics and Lagrangian methods are well suited for structural mechanics and if we consider fluid structure interaction problem we have solid boundaries, like moving walls, which is in contact with the fluid and due to motion of the fluid it can displace then Eulerian-Lagrangian formulation is perfect. Typical applications are fluid structure interaction, all kind of problems with moving boundaries. It combines the advantages of Eulerian and Lagrangian approaches.

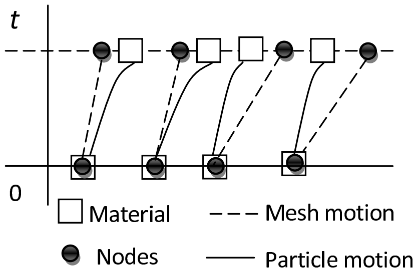

Figure 2.5: ALE mesh and particle description-1D

In the case of fluid-structure interaction problem we can still use the Lagrangian description for the deformation of the solid part. The fluid flow now takes place in a domain with boundary given by the deformation of the structure which can change in time and is influenced back by the fluid flow. The mixed ALE description of the fluid has to be used in this case. The fundamental quantity describing the motion of the fluid is still the velocity vector but the description is accompanied by a certain displacement field which describes the change of the fluid domain. This displacement field has no connection to the fluid velocity field and the purpose of its introduction is to provide a transformation of the current fluid domain and corresponding governing equations to some fixed reference domain. This method is sometimes called a **pseudo-solid mapping method** [115].

In the following, we shall describe the basic mathematical concepts underlying the ALE description and then provide the relation between all three descriptions.

In the ALE formulation, a third region $\Omega_{\mathscr{X}}$ is the reference configuration instead of Ω or Ω_t. The mapping $\zeta_{\mathscr{X}}$ from reference configuration to Eulerian configuration Ω_t, which means the motion of the mesh nodes in the spatial Eulerian region, is represented

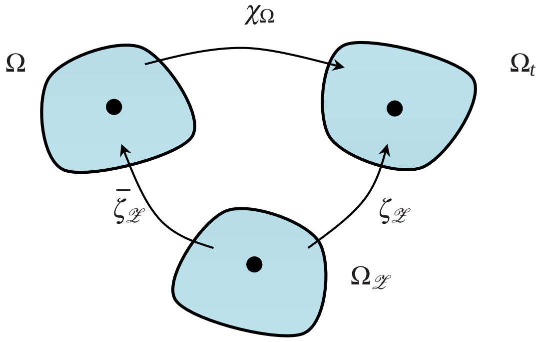

Figure 2.6: Moving computational region $\Omega_{\mathscr{X}}$ for ALE and regions Ω_t, Ω for Euler and Lagrangian maps respectively.

by

$$\zeta_{\mathscr{X}} : \mathscr{X} \times [0,T] \mapsto \mathscr{X}_t, \qquad \mathscr{X} \subset \Omega_{\mathscr{X}}, \qquad \mathscr{X}_t \subset \Omega_t \quad \forall t \in [0,T],$$

$$\zeta(\mathscr{X},t) = (\mathbf{x},t),$$

and its gradient is

$$\frac{\partial \zeta(\mathscr{X},t)}{\partial(\mathscr{X},t)} = \begin{pmatrix} \frac{\partial \mathbf{x}}{\partial \mathscr{X}} & \mathbf{v}_{\mathscr{X}} \\ \mathbf{0}^T & 1 \end{pmatrix},$$

where

$$\mathbf{v}_{\mathscr{X}} = \frac{\partial \zeta_{\mathscr{X}}}{\partial t},$$

is the corresponding mesh velocity involved in the $\Omega_{\mathscr{X}}$ region and $\mathbf{0}^T$ is a null row-vector. Finally, for the mapping $\bar{\zeta}_{\mathscr{X}}$ from reference configuration to Lagrangian configuration, it is suitable to represent directly its inverse $\bar{\zeta}_{\mathscr{X}}^{-1}$,

$$\bar{\zeta}_{\mathscr{X}} : \mathscr{X} \times [0,T] \mapsto \mathscr{X}, \qquad \mathscr{X} \subset \Omega_{\mathscr{X}}, \qquad \mathscr{X} \subset \Omega, \quad \forall t \in [0,T],$$

$$\bar{\zeta}(\mathscr{X},t) = (\mathbf{X},t), \qquad \text{or} \qquad (\mathscr{X},t) = \bar{\zeta}^{-1}(\mathbf{X},t),$$

and its gradient is

$$\frac{\partial \bar{\zeta}^{-1}(\mathbf{X},t)}{\partial(\mathbf{X},t)} = \begin{pmatrix} \frac{\partial \mathscr{X}}{\partial \mathbf{X}} & \mathbf{v}_{\mathbf{X}} \\ \mathbf{0}^T & 1 \end{pmatrix},$$

where $\mathbf{v}_{\mathbf{X}} = \frac{\partial \bar{\zeta}_{\mathscr{X}}}{\partial t}$ is considered as particle velocity in the reference configuration Ω. The relation between velocities $\mathbf{v}$, $\mathbf{v}_{\mathscr{X}}$ and $\mathbf{v}_{\mathbf{X}}$ can be attained by

$$\chi = \zeta \circ \bar{\zeta}^{-1}, \tag{2.5}$$

differentiating 2.5 keeping $\mathbf{X}$ fixed, it becomes

$$\frac{\partial \chi}{\partial(\mathbf{X},t)}(\mathbf{X},t) = \frac{\partial \zeta}{\partial(\mathscr{X},t)} \bar{\zeta}^{-1}(\mathbf{X},t) \frac{\partial \bar{\zeta}^{-1}}{\partial(\mathbf{X},t)}(\mathbf{X},t),$$

in matrix form

$$\begin{pmatrix} \frac{\partial \mathbf{x}}{\partial \mathbf{X}} & \mathbf{v} \\ \mathbf{0}^T & 1 \end{pmatrix} = \begin{pmatrix} \frac{\partial \mathbf{x}}{\partial \mathscr{X}} & \mathbf{v}_{\mathscr{X}} \\ \mathbf{0}^T & 1 \end{pmatrix} \begin{pmatrix} \frac{\partial \mathscr{X}}{\partial \mathbf{X}} & \mathbf{v}_{\mathbf{X}} \\ \mathbf{0}^T & 1 \end{pmatrix},$$

which furnishes after matrix multiplication,

$$\mathbf{v} = \mathbf{v}_{\mathscr{X}} + \frac{\partial \mathbf{x}}{\partial \mathscr{X}} \cdot \mathbf{v}_{\mathbf{X}},$$

with $\mathbf{v} = \frac{\partial \chi_{\mathbf{X}}}{\partial \mathbf{t}}$ is the material velocity. This equation can be rewritten as

$$\mathbf{c} := \mathbf{v} - \mathbf{v}_{\mathscr{X}} = \frac{\partial \mathbf{x}}{\partial \mathscr{X}} \mathbf{v}_{\mathbf{X}},$$

which is the relative velocity of the mesh and material particle, as seen from the spatial region. Here, $\mathbf{v}_{\mathbf{X}} = \left.\frac{\partial \mathbf{x}}{\partial t}\right|_{\mathbf{X}}$, is the particle velocity in the referential domain (as seen from the referential region). Above equation is also known as convective velocity.

1. $\mathbf{c} = \mathbf{v}_{\mathbf{X}}$ only for $\frac{\partial \mathbf{x}}{\partial \mathscr{X}} = \mathbf{I}$ which results in pure translation of continuum, i.e no deformation.
2. The Lagrangian and Eulerian descriptions are recovered under the following assumptions:
    - The Lagrangian: For $\bar{\zeta}_{\mathscr{X}} = \mathbf{I}$, reduces to $\mathbf{X} \equiv \mathscr{X}$, and material and mesh velocities material velocities coincide $\mathbf{v}_{\mathbf{X}} = \mathbf{v}$ which guaranteed no convective terms in the conservation laws, i.e. $\mathbf{v}_{\mathbf{X}} = \mathbf{c} = \mathbf{0}$.
    - Eulerian: For $\zeta_{\mathscr{X}} = \mathbf{I}$, reduces to $\mathbf{x} \equiv \mathscr{X}$, a null mesh velocity is obtained $\mathbf{v}_{\mathbf{X}} = \mathbf{0}$ which means the convective velocity $\mathbf{c}$ is identical to material velocity $\mathbf{v}$.

Material Spatial Time Derivative

The fundamental ALE relation between material time derivatives, referential time derivatives and spatial gradient is finally

$$\frac{df}{dt} = \left.\frac{\partial f}{\partial t}\right|_{\mathbf{X}} = \left.\frac{\partial f}{\partial t}\right|_{\mathbf{x}} + \mathbf{v} \cdot \nabla f = \left.\frac{\partial f}{\partial t}\right|_{\mathscr{X}} + \mathbf{c} \cdot \nabla f,$$

which can be interpreted in the usual way: the variation of the physical quantity for a given particle X is the local variation (i.e., with respect to the reference $\mathscr{X}$) plus a convective term taking into account the relative motion between the material and the reference system. This equation is equivalent to material derivative equivalent to spatial derivative but in the ALE formulation; that is, when $(\mathscr{X}, t)$ is the reference [44].
Material acceleration:

$$\mathbf{a} = \frac{d\mathbf{v}}{dt} = \left.\frac{\partial \mathbf{v}}{\partial t}\right|_{\mathbf{X}} = \left.\frac{\partial \mathbf{v}}{\partial t}\right|_{\mathbf{x}} + \mathbf{v} \cdot \nabla \mathbf{v} = \left.\frac{\partial \mathbf{v}}{\partial t}\right|_{\mathscr{X}} + \mathbf{c} \cdot \nabla \mathbf{v}.$$

Next, the mechanical fields describing the deformation and strain are defined as follows in the subsequent subsection.

2.2.2 Deformation and Strain

A continuum body which is able to change its shape under the effect of forces applied (stress) is said to be deformable and the deformation gradient with respect to the reference configuration is defined as the spatial derivative of the one-to-one, twice continuously differentiable map χ

$$\mathbf{F} = \frac{\partial \chi}{\partial \mathbf{X}} = \mathrm{Grad}\,\mathbf{x} = \begin{pmatrix} \frac{\partial \mathbf{x_1}}{\partial \mathbf{X_1}} & \frac{\partial \mathbf{x_1}}{\partial \mathbf{X_2}} & \frac{\partial \mathbf{x_1}}{\partial \mathbf{X_3}} \\ \frac{\partial \mathbf{x_2}}{\partial \mathbf{X_1}} & \frac{\partial \mathbf{x_2}}{\partial \mathbf{X_2}} & \frac{\partial \mathbf{x_2}}{\partial \mathbf{X_3}} \\ \frac{\partial \mathbf{x_3}}{\partial \mathbf{X_1}} & \frac{\partial \mathbf{x_3}}{\partial \mathbf{X_2}} & \frac{\partial \mathbf{x_3}}{\partial \mathbf{X_3}} \end{pmatrix}.$$

Local invertibility of χ needs that $\mathbf{F}$ be non-singular, which means $\det \mathbf{F} > 0$. Similarly, inverse **deformation gradient** is

$$\mathbf{F}^{-1} = \frac{\partial \chi^{-1}}{\partial \mathbf{x}} = \nabla \mathbf{X} = \begin{pmatrix} \frac{\partial \mathbf{X_1}}{\partial \mathbf{x_1}} & \frac{\partial \mathbf{X_1}}{\partial \mathbf{x_2}} & \frac{\partial \mathbf{X_1}}{\partial \mathbf{x_3}} \\ \frac{\partial \mathbf{X_2}}{\partial \mathbf{x_1}} & \frac{\partial \mathbf{X_2}}{\partial \mathbf{x_2}} & \frac{\partial \mathbf{X_2}}{\partial \mathbf{x_3}} \\ \frac{\partial \mathbf{X_3}}{\partial \mathbf{x_1}} & \frac{\partial \mathbf{X_3}}{\partial \mathbf{x_2}} & \frac{\partial \mathbf{X_3}}{\partial \mathbf{x_3}} \end{pmatrix},$$

where Grad and ∇ are the gradient operator in Ω and Ω_t, respectively. The equation

$$d\mathbf{x} = \mathbf{F}d\mathbf{X}, \tag{2.6}$$

furnishes a measure of how much the infinitesimal line element $d\mathbf{X}$ of material at the point $\mathbf{X}$ transform linearly under the deformation into the line element $d\mathbf{x}$ at $\mathbf{x}$, additionally angle and length might have changed. The determinant of $\mathbf{F}$ is denoted as J, i.e.,

$$J = \det \mathbf{F}, \tag{2.7}$$

called the Jacobian of the deformation, which is everywhere strictly positive, so that deformation mapping is orientation preserving as $\mathbf{F}$ is invertible. We then have

$$0 < J < \infty.$$

The relation between the deformation gradient and displacement gradient from equations 2.1, 2.2, are

$$\mathbf{H_X} = \mathbf{F} - \mathbf{I} \qquad \text{and} \qquad \mathbf{H_x} = \mathbf{I} - \mathbf{F}^{-1}$$

where $\mathbf{H_X} = \mathrm{Grad}\,\mathbf{u}$ and $\mathbf{H_x} = \nabla \mathbf{u}$ are the second order displacement gradient tensors in the material and spatial descriptions respectively.

The relation between the **volume element** dV of the reference configuration Ω to the volume element dv of the current configuration is related by

$$dv = JdV. \tag{2.8}$$

The deformation is called isochoric or volume preserving for

$$J = \det \mathbf{F} = 1 \tag{2.9}$$

It is mathematical requirement that $J \neq 0$, and $J > 0$ is physical requirement as volume can not have negative value. A material which satisfies 2.9 for all deformation gradients $\mathbf{F}$ is said to be incompressible.

Now, we establish the relation between the elements of **surface area** and volume transform in the material and spatial region. Let $\mathbf{dA} \equiv \mathbf{N}dA$ be a vector surface area element on $\partial\Omega$, where $\mathbf{N}$ is the outward unit normal to the surface, and $\mathbf{da} \equiv \mathbf{n}da$ the corresponding area element on $\partial\Omega_t$. Then, the area elements are related by using Nanson's formula as

$$\mathbf{n}da = \mathbf{J}\mathbf{F}^{-T}\mathbf{N}dA, \qquad \text{or} \qquad \int_{\Omega_t} \mathbf{n}da = \int_{\Omega} \mathbf{J}\mathbf{F}^{-T}\mathbf{N}dA, \tag{2.10}$$

where $\mathbf{F}^{-T} = (\mathbf{F}^{-1})^T$ and ^{T} is for transpose. Here, $\mathbf{n}$ is not in parallel with the same line element of material like $\mathbf{N}$. Recalling the definition of the cofactor matrix of an invertible matrix $\mathbf{A}$

$$\operatorname{cof}\mathbf{A} = (\det\mathbf{A})\mathbf{A}^{-T}, \tag{2.11}$$

it is possible to state Nanson's theorems on normals:

Theorem 1 *Nanson's formula: From the previous definitions*

$$\mathbf{n}d(\partial\Omega_t) = \operatorname{cof}\mathbf{F}_\chi\mathbf{N}d(\partial\Omega). \tag{2.12}$$

Proof 1 *A proof using vector calculus tools can be found in [98], p. 88. Let us consider the infinitesimal oriented surface* $\mathbf{N}d(\partial\Omega) = d\mathbf{X}^a \times d\mathbf{X}^b$ *(*$d\mathbf{X}^a$ *and* $d\mathbf{X}^b$ *lie on the tangent plane to the surface* $\partial\Omega$*, with outward normal* $\mathbf{N}$*). The inner product* $d\mathbf{X}\cdot\mathbf{N}(\partial\Omega)$*, represents the measure of the volume extruded from* $d(\partial\Omega)$ *along the infinitesimal increment* $d\mathbf{X}$*. The push forward through the map* χ *of such volume transforms according to* 2.8*:*

$$d\mathbf{x}\cdot\mathbf{n}d(\partial\Omega_t) = J_\chi(d\mathbf{X}\cdot\mathbf{N}d(\partial\Omega)), \tag{2.13}$$

where $\mathbf{n}d(\partial\Omega_t) = d\mathbf{x}^a \times d\mathbf{x}^b$, $d\mathbf{x}^a = \mathbf{F}_\chi\mathbf{X}^a$, $d\mathbf{x}^b = \mathbf{F}_\chi\mathbf{X}^b$, *and* $d\mathbf{x} = \mathbf{F}_\chi\mathbf{X}$*. Hence*

$$\begin{aligned} d\mathbf{x}\cdot\mathbf{n}d(\partial\Omega_t) =& J_\chi(d\mathbf{X}\cdot\mathbf{N}d(\partial\Omega)) \\ =& J_\chi{\mathbf{F}_\chi}^{-1}d\mathbf{x}\cdot\mathbf{N}d(\partial\Omega) \\ =& d\mathbf{x}\cdot(J_\chi{\mathbf{F}_\chi}^{-T}\mathbf{N})d(\partial\Omega) \\ =& d\mathbf{x}\cdot(\operatorname{cof}\mathbf{F}_\chi\mathbf{N})d(\partial\Omega). \end{aligned} \tag{2.14}$$

The result in 2.14 *must hold for any vector* $d\mathbf{x}$*. Since the inner product is a linear operator on a finite dimensional vector space,* 2.14 *yields* 2.12 *#.*

And also the Piola identity will be used

Theorem 2 *Piola Identity*

$$\begin{aligned} \mathbf{0} =& \operatorname{Div}(J\mathbf{F}^{-T}) \\ =& \operatorname{Div}(\operatorname{cof}\mathbf{F}), \end{aligned} \tag{2.15}$$

Proof 2 *The Piola identity can be proved in several ways, all very instructive on the type of manipulations that are commonly used in continuum mechanics. One possibility, presented next, is to apply the Gauss divergence theorem to an arbitrary constant vector field* $\mathbf{f}$ *and use Nanson's formula* 2.12*. Let* ω_x *be an open subset of* Ω_t*, thus*

$$\begin{aligned} \mathbf{0} &= \int_{\omega_\mathbf{x}\subset\Omega_t} \operatorname{div}\mathbf{f}\,dv \\ &= \int_{\partial\omega_\mathbf{x}} \mathbf{f}\cdot\mathbf{n}\,da && \textit{by Gauss divergence theorem}\\ &= \int_{\partial\omega_\mathbf{X}=\chi^{-1}(\partial\omega_\mathbf{x})} \mathbf{f}\cdot(\operatorname{cof}\mathbf{F}_\chi\mathbf{N})\,dA && \textit{by Nanson's formula} \\ &= \int_{\partial\omega_\mathbf{X}} (J_\chi \mathbf{F}_\chi{}^{-1}\mathbf{f})\cdot\mathbf{N}\,dA && \textit{by } 2.7 \textit{ and } 2.11\\ &= \int_{\omega_\mathbf{X}} \operatorname{Div}(J_\chi\mathbf{F}_\chi{}^{-1}\mathbf{f})\,dV && \textit{by Gauss divergence theorem}\end{aligned}\tag{2.16}$$

where we recall that $\mathbf{f}$ *is constant. Hence,* 2.16 *can be rewritten as*

$$\mathbf{0} = \int_{\omega_\mathbf{X}} \operatorname{Div}(J_\chi\mathbf{F}_\chi{}^{-1}\mathbf{f})\,dV = \mathbf{f}\cdot\left(\int_{\omega_\mathbf{X}} \operatorname{Div}(\operatorname{cof}\mathbf{F}_\chi)\,dV\right)\tag{2.17}$$

Recalling that $\mathbf{f}$ *is arbitrary and* χ *is smooth, and using the localization theorem in the limit of a domain* $\omega_\mathbf{X}$*,* 2.17 *implies*

$$\begin{aligned}\mathbf{0} &= \operatorname{Div}(J\mathbf{F}^{-T})\\ &= \operatorname{Div}(\operatorname{cof}\mathbf{F}),\end{aligned}\tag{2.18}$$

which concludes the proof #.

Remark 2.19 *The results just proved in theorem 1 and 2 are very useful when changing coordinates of integral formulations involving the divergence of a tensor or vector quantity from the current configuration to the corresponding configuration and vice versa.*

After manipulating with 2.6 it follows how **length elements changes**

$$|d\mathbf{x}|^2 = (\mathbf{FM})\cdot(\mathbf{FM})\,|d\mathbf{X}|^2 = (\mathbf{F}^T\mathbf{FM})\cdot\mathbf{M}\,|d\mathbf{X}|^2,$$

where $\mathbf{M}$ is a unit vector at $\mathbf{X}$ in the direction of $d\mathbf{X}$. Now, the ratio $|d\mathbf{x}|/d\mathbf{X}$ of the length of a line element in the deformed and reference configurations takes the form

$$\frac{|d\mathbf{x}|}{|d\mathbf{X}|} = |\mathbf{FM}| = [\mathbf{M}\cdot(\mathbf{F}^T\mathbf{FM})]^{1/2} \equiv \lambda(\mathbf{M}).\tag{2.20}$$

Equation 2.20 express the stretch $\lambda(\mathbf{M})$ at $\mathbf{X}$ in the direction of $d\mathbf{X}$. It is evident that it is confined to inequalities

$$0 < \lambda(\mathbf{M}) < \infty.$$

If there is no stretch in the direction $\mathbf{M}$ the $\lambda(\mathbf{M}) = 1$ which follows

$$(\mathbf{F}^T\mathbf{FM})\cdot\mathbf{M} = 1.\tag{2.21}$$

Equation 2.21 holds for all $\mathbf{M}$ in case there is no stretch in any direction which indicates that no strain occurs at $\mathbf{X}$. It follows that $\mathbf{F}^T\mathbf{F} = \mathbf{I}$, where $\mathbf{I}$ is identity tensor. An appropriate strain measure tensor as a consequence is $\mathbf{F}^T\mathbf{F} - \mathbf{I}$, since this tensor vanishes for unstrained material. This leads to another strain measure, the so called **Green-St.Venant strain tensor**

$$\mathbf{E} = \frac{1}{2}(\mathbf{F}^T\mathbf{F} - \mathbf{I}), \qquad \boxed{2.22}$$

where $1/2$ is a normalization factor.

Along with $\mathbf{F}$ and $\mathbf{E}$ it is useful to consider other related tensors. Specifically, we introduce the symmetric tensors

$$\mathbf{C} = \mathbf{F}^T\mathbf{F} \qquad \mathbf{B} = \mathbf{F}\mathbf{F}^T,$$

which are called **right and left Cauchy-Green strain (deformation) tensors** in respectively. The **rigid body deformation** is represented as

$$\chi(\mathbf{X}) = \mathbf{d} + \mathbf{Q}\mathbf{X} \quad \forall \mathbf{X} \subset \Omega$$

where $\mathbf{d}$ is some translation vector and $\mathbf{Q}$ is the rotation tensor. For body to be rigid it means there is no stretches, no changes in angle, no change in shape. Then the measure of strain i.e. deformation gradient $\mathbf{F} = \mathbf{Q}$ holds, which leads to

$$\mathbf{C} = \mathbf{F}^T\mathbf{F} = \mathbf{I}$$

In short, a deformation map χ describes a rigid body motion, if and only if its right Cauchy-Green strain tensor C is the identity matrix. From a mechanical point of view in 2.22 (the so called Green-St Vennant strain tensor) is the natural strain measure since it is zero in case of a rigid body motion. This is also good estimate to measure deformation. The Green-St.Venant strain tensor $\mathbf{E}$ can be written in terms of displacements

$$\mathbf{E} = \frac{1}{2}(\mathrm{Grad}\,\mathbf{u} + \mathrm{Grad}\,\mathbf{u}^T + \mathrm{Grad}\,\mathbf{u}^T\,\mathrm{Grad}\,\mathbf{u})$$

2.2.3 Stress Tensors and Equilibrium Equation

Axiom 1 *Cauchy stress principle*[2]*: The forces acting on the a generic material volume V of body in* Ω *can be divided into two main categories:*

1. *Body force, which reach into V from a distance, an example of such a body force is gravity.*
2. *Contact force, which is due to the contact of the surrounding surface of V with the rest of the body. Contact forces or stress is due to the mutual interaction of the particle.*

The principle then states that the action exerted at a point P and due to the material outside S is represented by a vector $\mathbf{t}$*, called stress vector, depending on P, S and* $\mathbf{t}$*, where S is any closed surface within* Ω *and let P is a point on S.*

---

[2] The Cauchy stress principle formulated by A. L . Cauchy in 1827

The stress vector **t** *has dimension of force per unit surface. Thus, if S_a denotes any surface within Ω , we have*

$$\textit{Total force exerted by the body across } S_a = \int_{S_a} \mathbf{t} dS_a$$

Remark 2.23 *Materials for which Cauchy's principle holds are also called non-polar materials (i.e., materials which are unable to sustain local torques).*

Remark 2.24 *Cauchy's principle does not specify the way in which the stress vector may depend on the surface.*

A fundamental result due to W. Noll states that *the stress vector at a point P of a surface S depends on the surface S, only through the exterior unit normal vector* **n** *to S at P*. Therefore,

$$\begin{aligned} \mathbf{t} =& \mathbf{t}(\mathbf{x}, t; \mathbf{n}), \qquad \text{or} \\ =& \mathbf{t}(\mathbf{n}) \qquad \text{where x is the position occupied by P at time t} \end{aligned}$$

Theorem 3 *Cauchy Theorem. Fluid and continuum mechanics are based on three fundamental assumptions concerning the interior forces:*

1. *interior forces act via the surface of a volume $V(t)$,*
2. *interior forces only depend on the normal direction of the surface of the volume,*
3. *interior forces are additive and continuous.*

Due to the Cauchy theorem these assumptions imply that the interior forces acting on a volume $V(t)$ must be of the form

$$\int_{\partial V} \sigma \mathbf{n} dS,$$

Here, as usual, ∂V denotes the boundary of the volume $V(t)$, **n** *is the unit outward normal, and dS denotes the surface element. The* **integral theorem of Gauss** *then yields*

$$\int_{\partial V} \sigma \mathbf{n} dS = \int_{V} \operatorname{div} \sigma dv.$$

The surface force per unit area (or stress vector) on the vector area element da is denoted by **t**. It depends on **n** followed by the formula

$$\mathbf{t} = \sigma^T \mathbf{n},$$

where σ is called the second-order Cauchy stress tensor which is independent of **n**.

$$\mathbf{t}^{(\mathbf{e}_i)} = t_j^{(\mathbf{e}_i)} \mathbf{e}_j = \sigma_{ij} \mathbf{e}_j,$$

in the matrix form

$$\sigma = \sigma_{ij} = \begin{bmatrix} \mathbf{t}^{(\mathbf{e}_1)} \\ \mathbf{t}^{(\mathbf{e}_2)} \end{bmatrix} = \begin{bmatrix} \sigma_{11} & \sigma_{12} & \sigma_{13} \\ \sigma_{21} & \sigma_{22} & \sigma_{23} \\ \sigma_{31} & \sigma_{32} & \sigma_{33} \end{bmatrix}$$

$$\equiv \begin{bmatrix} \sigma_{xx} & \sigma_{xy} & \sigma_{xz} \\ \sigma_{yx} & \sigma_{yy} & \sigma_{yz} \\ \sigma_{zx} & \sigma_{zy} & \sigma_{zz} \end{bmatrix}$$

$$\equiv \begin{bmatrix} \sigma_{x} & \tau_{xy} & \tau_{xz} \\ \tau_{yx} & \sigma_{y} & \tau_{yz} \\ \tau_{zx} & \tau_{zy} & \sigma_{z} \end{bmatrix},$$

where σ_x, σ_y and σ_z are normal stresses, and $\tau_{xy}\tau_{xz}$, τ_{yx}, τ_{yz}, τ_{zx} and σ_{zy} are shear stresses. For the 2D computations we restricted to plain strain which means $\tau_{xz} \equiv \tau_{yz} \equiv \tau_{zx} \equiv \tau_{zy} \equiv 0$ and $\sigma_z = 1$, [71]. Making use of 2.10 the force on da may be written as

$$\mathbf{t}da = \tilde{\mathbf{P}}^T \mathbf{N} dA$$

where the nominal tensor $\tilde{\mathbf{P}}$ is related to σ by

$$\tilde{\mathbf{P}} = J\mathbf{F}^{-1}\sigma$$

The **first Piola-Kirchhoff tensor** is denoted by $\mathbf{P} = \tilde{\mathbf{P}}^T$, see [64] for more detail. Unlike the Cauchy stress tensor σ, the first Piola-Kirchhoff tensor $\mathbf{P}$ is non-symmetric. Let $\mathbf{b}$ be a body force per unit mass. Then, in integral form, the equilibrium equation for the body may be written with reference to Ω or Ω_t as follows

$$\int_{\Omega_t} \rho_t \mathbf{b} dv + \int_{\partial\Omega_t} \sigma^T \mathbf{n} da = \int_{\Omega} \rho \mathbf{b} dV + \int_{\partial\Omega} \mathbf{P}\mathbf{N} dA = \mathbf{0},$$

in which it is natural to introduce the symmetric **second Piola-Kirchhoff tensor S**

$$\mathbf{S} = \tilde{\mathbf{P}}\mathbf{F}^{-T} = J\mathbf{F}^{-1}\sigma\mathbf{F}^{-T}.$$

Frame Indifference

Quantities which are independent of the observer , i.e., with respect to different frames is called frame indifference. Examples of this are mass density, temperature, heat flux vector, Cauchy stress tensor, and counter examples are velocity and acceleration fields which are not frame indifference.

Useful relations Three descriptions (Eulerian, Lagrangian, ALE) can be related to each other through following relations

$$\begin{aligned}
\bar{\varphi}(\mathbf{X},t) =& \tilde{\varphi}(\chi(\mathbf{X},t),t), \qquad \boxed{2.25}\\
\frac{d\varphi}{dt} =& \frac{\partial \varphi}{\partial t} + (\nabla\varphi)\mathbf{v}, \qquad \boxed{2.26}\\
\mathrm{Grad}\,\varphi =& (\nabla\varphi)\mathbf{F}, \qquad \boxed{2.27}\\
\int_{\Omega_t} \varphi dv =& \int_{\Omega} \varphi J dV \qquad \boxed{2.28}\\
\frac{d\mathbf{F}}{dt} =& \mathrm{Grad}\,\mathbf{v}, \qquad \boxed{2.29}\\
\frac{\partial J}{\partial \mathbf{F}} =& J\mathbf{F}^{-T}, \qquad \boxed{2.30}\\
\frac{dJ}{dt} =& J\,\mathrm{div}\,\mathbf{v}. \qquad \boxed{2.31}
\end{aligned}$$

2.3 Balance Laws

In this section we will formulate the balance relations for mass and momentum in three forms: the Eulerian, the Lagrangian and the arbitrary Eulerian-Lagrangian (ALE) description. The balance relations for energy and entropy are formulated in the Eulerian description which is sufficient for our purpose since they are used only in the specification of the constitutive relations in section 2.5.2.

For the formulation of the balance laws we will need to express a time derivatives of some integrals, using the Reynolds Transport Theorem (for short RTT) and Gauss divergence theorem. The following series of equalities obtained by using the previously stated relations will be useful

$$\begin{aligned}
\frac{d}{dt}\int_{\Omega_t} \varphi dv = \frac{d}{dt}\int_{\Omega} \varphi J dV = \int_{\Omega} \frac{d}{dt}(\varphi J)\, dV& \\
&= \int_{\Omega_t} \left(\frac{d\varphi}{dt} + \varphi\,\mathrm{div}\,\mathbf{v}\right) dv \\
&= \int_{\Omega_t} \left(\frac{\partial\varphi}{\partial t} + \mathrm{div}\,(\varphi\mathbf{v})\right) dv \qquad \text{RTT} \qquad \boxed{2.32}\\
&= \int_{\Omega_t} \frac{\partial\varphi}{\partial t} dv + \int_{\partial\Omega_t} \varphi\mathbf{v}\cdot\mathbf{n}da \qquad \text{Gauss theorem}\\
&= \frac{\partial}{\partial t}\int_{\Omega_t} \varphi dv + \int_{\partial\Omega_t} \varphi\mathbf{v}\cdot\mathbf{n}da.
\end{aligned}$$

Theorem 4 *Reynolds Transport Theorem: Consider an arbitrary volume $V \subset \Omega_t$. The following* **transport theorem** *holds for all differentiable mapping φ*

$$\frac{d}{dt}\int_{\Omega_t} \varphi dv = \int_{\Omega_t} \left(\frac{\partial\varphi}{\partial t} + \mathrm{div}\,(\varphi\mathbf{v})\right) dv \qquad \mathit{RTT} \qquad \boxed{2.33}$$

Theorem 5 *Gauss Divergence Theorem: The* **Gauss divergence theorem** *states that for all differentiable mapping* φ

$$\int_{\Omega_t} \operatorname{div}(\varphi \mathbf{v})\, dv = \int_{\partial\Omega_t} \varphi \mathbf{v} \cdot \mathbf{n} da \qquad \textit{Gauss theorem} \tag{2.34}$$

2.3.1 Balance of Mass

The mass m of a fixed region $\mathscr{P} \subset \mathbb{R}^3$ in space with the boundary $\partial\mathscr{P}$ of body $\mathscr{B}$ is

$$m(p) = \int_{\mathscr{P}} \rho(x,t) dv, \quad \mathscr{P} \subset \Omega_t \quad \text{for all } t \in [0,T],$$

where $\rho(x,t)$ is the Eulerian material density. The arbitrary volume $\mathscr{P}$ is the material control volume, which is independent of time. The fundamental principle of conservation of mass states that the continuum body does not change its position and shape in time. Then the balance of mass in the region $\mathscr{P}$ can be written as

$$\frac{d}{dt} \int_{\mathscr{P}} \rho(x,t) dv = 0, \quad \text{for all } t \in [0,T], \tag{2.35}$$

equation 2.35 is also known as conservation of mass in integral form. Making use of the Reynolds transport theorem 2.33 it becomes

$$\frac{\partial}{\partial t} \int_{\mathscr{P}} \rho dv + \int_{\partial\mathscr{P}} \rho \mathbf{v} \cdot \mathbf{n}_{\mathscr{P}} da = 0,$$

with the boundary $\partial\mathscr{P}$ and unit outward normal vector $\mathbf{n}_{\mathscr{P}}$. After applying the Gauss divergence theorem the principle of conservation of mass with respect to the spatial (Eulerian) representation can be written as

$$\int_{\mathscr{P}} [\frac{\partial \rho}{\partial t} + \operatorname{div}(\rho \mathbf{v})] dv = 0, \quad \text{for all } t \in [0,T],$$

which is global (integral) form of the conservation of mass. If all the fields are sufficiently smooth this equation can be written in local (differential) form[3] with respect to the current configuration as

$$\frac{\partial \rho}{\partial t} + \operatorname{div}(\rho \mathbf{v}) = 0. \tag{2.36}$$

It will be useful to derive the mass balance equation from the Lagrangian point of view. Let $\mathscr{Q} \subset \Omega$ be a fixed set of particles. Then the relation between the densities in reference Ω and current configuration Ω_t is established, which is given by $\rho_t J = \rho_0$.

---

[3] An equation which holds at every point of continuum and for all times, for example eq 2.36, is referred to as the local (or differential) form of that equation (local means point wise). An equation in which physical quantities over a certain region of space are integrated is referred to as the global (or integral) form of that equation; see for example equation 2.37. Consequently we may say that 2.37 is global form and 2.36 is the local form of the conservative laws of mass. In general local forms are ideally suited for approximation techniques such as the finite difference method while global forms are best to start with when the finite element method is employed.

Let $\chi(\mathscr{Q},t) \subset \Omega_t$ is a region occupied by these particles at the time t, and the balance of mass can be expressed as

$$\frac{d}{dt}\int_{\chi(\mathscr{Q},t)} \rho dv = 0, \tag{2.37}$$

which in local form with respect to the reference configuration can be written as

$$\frac{d}{dt}(\rho J) = 0. \tag{2.38}$$

In the case of arbitrary Lagrangian-Eulerian description we take a region $\mathscr{X} \in \mathbb{R}^3$ which is itself moving independently of the motion of the body. Let the motion of the control region $\mathscr{X}$ be described by a given mapping

$$\zeta_{\mathscr{X}} : \mathscr{X} \times [0,T] \mapsto \mathscr{X}_t, \qquad \mathscr{X}_t \subset \Omega_t \quad \forall t \in [0,T],$$

with the corresponding velocity $\mathbf{v}_{\mathscr{X}} = \frac{\partial \zeta_{\mathscr{X}}}{\partial t}$, deformation gradient $\mathbf{F}_{\mathscr{X}} = \frac{\partial \zeta_{\mathscr{X}}}{\partial \mathbf{X}}$ and its determinant $J_{\mathscr{X}} = \det \mathbf{F}_{\mathscr{X}}$. The balance equation can be written as

$$\frac{\partial}{\partial t}\int_{\mathscr{X}_t} \rho dv + \int_{\partial \mathscr{X}_t} \rho(\mathbf{v} - \mathbf{v}_{\mathscr{X}}) \cdot \mathbf{n}_{\mathscr{X}_t} da = 0,$$

this can be viewed as Eulerian description with moving spatial coordinate system or as a grid deformation in the context of the finite element method. In order to obtain a local form of the balance relation we need to transform the integration to the fixed spatial region $\mathscr{X}$

$$\frac{\partial}{\partial t}\int_{\mathscr{X}} \rho J_{\mathscr{X}} dv + \int_{\partial \mathscr{X}} \rho(\mathbf{v} - \mathbf{v}_{\mathscr{X}}) \cdot \mathbf{F}_{\mathscr{X}}^{-T} \mathbf{n}_{\mathscr{X}} J_{\mathscr{X}} da = 0, \tag{2.39}$$

then the local form is

$$\frac{\partial}{\partial t}(\rho J_{\mathscr{X}}) + \operatorname{div}\left(\rho J_{\mathscr{X}}(\mathbf{v} - \mathbf{v}_{\mathscr{X}})\mathbf{F}_{\mathscr{X}}^{-T}\right) = 0. \tag{2.40}$$

The two previous special formulations can be now recovered. If the region $\mathscr{X}$ is not moving in space, i.e. $\mathscr{X} = \mathscr{X}_t, \forall t \in [0,T]$, then $\zeta_{\mathscr{X}}$ is the identity mapping, $\mathbf{F}_{\mathscr{X}} = \mathbf{I}, J_{\mathscr{X}} = 1, \mathbf{v}_{\mathscr{X}} = \mathbf{0}$ and 2.40 reduces to 2.36. While if the region $\mathscr{X}$ moves exactly with the material, i.e. $\zeta_{\mathscr{X}} = \chi|_{\mathscr{X}}$ then $\mathbf{F}_{\mathscr{X}} = \mathbf{F}, J_{\mathscr{X}} = J, \mathbf{v}_{\mathscr{X}} = \mathbf{v}$ and 2.40 reduces to 2.38.

2.3.2 Balance of Linear Momentum

The balance of linear momentum is postulated in a similar way. Let σ denote the Cauchy stress tensor field, representing the surface forces per unit area, $\mathbf{f}$ be the body forces acting on the material per its unit mass. Then the balance of linear momentum in the Eulerian description equals

$$\frac{\partial}{\partial t}\int_{\mathscr{P}} \rho \mathbf{v} dv + \int_{\partial \mathscr{P}} \rho \mathbf{v} \otimes \mathbf{v} \mathbf{n}_{\mathscr{P}} da = \int_{\partial \mathscr{P}} \sigma^T \mathbf{n}_{\mathscr{P}} da + \int_{\mathscr{P}} \rho \mathbf{f} dv. \tag{2.41}$$

The local form of the linear momentum balance is

$$\frac{\partial \rho \mathbf{v}}{\partial t} + \operatorname{div}(\rho \mathbf{v} \otimes \mathbf{v}) = \operatorname{div} \sigma^T + \rho \mathbf{f}, \tag{2.42}$$

where $\mathbf{v} \otimes \mathbf{v} = (v_i v_j)_{1 \leq i,j \leq 3}$, or making use of 2.36 we arrive at

$$\rho \frac{\partial \mathbf{v}}{\partial t} + \rho (\nabla \mathbf{v}) \mathbf{v} = \operatorname{div} \sigma^T + \rho \mathbf{f}.$$

From the Lagrangian point of view the momentum balance relation is

$$\frac{d}{dt} \int_{\chi(Q,t)} \rho \mathbf{v} dv = \int_{\partial \chi(Q,t)} \sigma^T \mathbf{n}_{\chi(Q,t)} da + \int_{\chi(Q,t)} \rho \mathbf{f} dv.$$

Let us denote by $\mathbf{P} = J \sigma^T \mathbf{F}^{-T}$ the first Piola-Kirchhoff stress tensor [64], then the local form of the momentum balance is

$$\frac{d}{dt} (\rho J \mathbf{v}) = \operatorname{Div} \mathbf{P} + \rho J \mathbf{f}, \tag{2.43}$$

or using 2.38 we can write

$$\rho J \frac{d\mathbf{v}}{dt} = \operatorname{Div} \mathbf{P} + \rho J \mathbf{f}.$$

In the arbitrary Lagrangian-Eulerian formulation we obtain

$$\frac{\partial}{\partial t} \int_{\mathscr{X}_t} \rho \mathbf{v} dv + \int_{\partial \mathscr{X}_t} \rho \mathbf{v} \otimes (\mathbf{v} - \mathbf{v}_{\mathscr{X}}) \mathbf{n}_{\mathscr{X}_t} da = \int_{\partial \mathscr{X}_t} \sigma^T \mathbf{n}_{\mathscr{X}_t} da + \int_{\mathscr{X}_t} \rho \mathbf{f} dv,$$

which in the local form gives

$$\frac{\partial \rho J_{\mathscr{X}} \mathbf{v}}{\partial t} + \operatorname{div}\left(\rho J_{\mathscr{X}} \mathbf{v} \otimes (\mathbf{v} - \mathbf{v}_{\mathscr{X}}) \mathbf{F}_{\mathscr{X}}^{-T}\right) = \operatorname{div}\left(J_{\mathscr{X}} \sigma^T \mathbf{F}_{\mathscr{X}}^{-T}\right) + \rho J_{\mathscr{X}} \mathbf{f}, \tag{2.44}$$

or with the use of 2.40 we can write

$$\rho J_{\mathscr{X}} \frac{\partial \mathbf{v}}{\partial t} + \rho J_{\mathscr{X}} (\nabla \mathbf{v}) \mathbf{F}_{\mathscr{X}}^{-T} (\mathbf{v} - \mathbf{v}_{\mathscr{X}}) = \operatorname{div}\left(J_{\mathscr{X}} \sigma^T \mathbf{F}_{\mathscr{X}}^{-T}\right) + \rho J_{\mathscr{X}} \mathbf{f}.$$

2.3.3 Balance of Angular Momentum

For the angular momentum balance we assume that there are no external or internal sources of angular momentum, then it follows that the Cauchy stress tensor has to be symmetric [121], i.e.

$$\sigma = \sigma^T. \tag{2.45}$$

2.3.4 Balance of Energy

Denoting the total energy per mass as $E = e + \frac{1}{2}|\mathbf{v}|^2$, where e be the internal energy per its unit mass, $\mathbf{q}$ be the heat flux per unit area, r be the heat source per unit mass. Then, the balance of energy is stated as

$$\begin{aligned}\frac{\partial}{\partial t}\int_{\mathscr{P}} \rho E dv + \int_{\partial\mathscr{P}} \rho E \mathbf{v}\cdot\mathbf{n} da = \int_{\partial\mathscr{P}} (\sigma\mathbf{v} - \mathbf{q})\cdot\mathbf{n} da \\ + \int_{\mathscr{P}} (\rho\mathbf{f}\cdot\mathbf{v} + \rho r)\, dv.\end{aligned} \tag{2.46}$$

Making use of the mass and momentum balance equations 2.36 and 2.42 in 2.46, this gives the equation for the conservation of energy in local form as

$$\frac{\partial \rho e}{\partial t} + \operatorname{div}(\rho e\mathbf{v}) = \operatorname{tr}(\sigma\nabla\mathbf{v}) - \operatorname{div}\mathbf{q} + \rho r. \tag{2.47}$$

2.3.5 Balance of Entropy

Finally, the balance of entropy is introduced. Let η be the entropy per its unit mass, T be the temperature and s be the entropy production, then the entropy balance is

$$\frac{\partial}{\partial t}\int_{\mathscr{P}} \rho\eta dv + \int_{\partial\mathscr{P}} \rho\eta\mathbf{v}\cdot\mathbf{n} da = -\int_{\partial\mathscr{P}} \frac{\mathbf{q}}{T}\cdot\mathbf{n} da + \int_{\mathscr{P}} \left(\frac{\rho r}{T} + s\right) dv, \tag{2.48}$$

or in local form

$$\frac{\partial \rho\eta}{\partial t} + \operatorname{div}(\rho\eta\mathbf{v}) = -\operatorname{div}\frac{\mathbf{q}}{T} + \frac{\rho r}{T} + s. \tag{2.49}$$

The second law of thermodynamics says that the total entropy production is non-negative, implying

$$s \geq 0. \tag{2.50}$$

We introduce the Helmholtz potential $\Psi = e - T\eta$, then using 2.47 and 2.50 we obtain the entropy inequality in the following form

$$\eta\left(\frac{\partial \rho T}{\partial t} + \operatorname{div}(\rho T\mathbf{v})\right) + \frac{\partial \rho\Psi}{\partial t} + \operatorname{div}(\rho\Psi\mathbf{v}) + \frac{\mathbf{q}}{T}\cdot\nabla T - \operatorname{tr}(\sigma\nabla\mathbf{v}) \leq 0. \tag{2.51}$$

This inequality is used to narrow the class of constitutive relations for the stresses σ in the section 2.5.2.

2.4 Fluid Structure Interaction problem formulation

Here we make few assumptions that will allow us to deal the problem more appropriately. We will use the superscripts ^{s} and ^{f} to denote the quantities connected with the solid and fluid. Let us assume that the both materials are incompressible, which is well accepted approximation in biomechanics and denote the constant densities of each material by ρ^f, ρ^s. Further we assume all the processes to be isothermal, meaning that the temperature T is constant, which is also well accepted approximation for certain biomechanical processes.

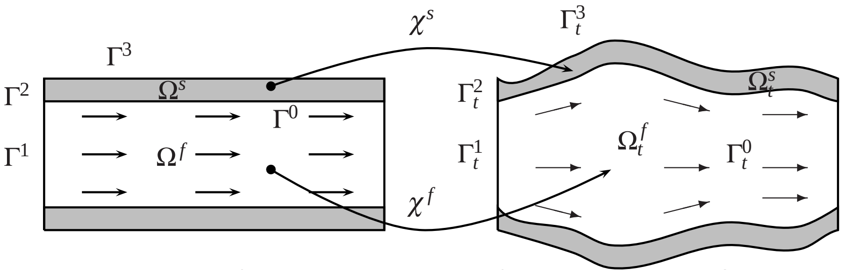

Figure 2.7: Undeformed (original) and deformed (current) configurations.

2.4.1 Monolithic Description

We denote by Ω^f_t the domain occupied by the fluid and Ω^s_t by the solid at time $t \in [0,T]$. Let $\Gamma^0_t = \bar{\Omega}^f_t \cap \bar{\Omega}^s_t$ be the part of the boundary where the solid interacts with the fluid and $\Gamma^i_t, i = 1,2,3$ be the remaining external boundaries of the solid and the fluid as depicted in Figure. 2.7.

Let the deformation of the solid part be described by the mapping χ^s

$$\chi^s : \Omega^s \times [0,T] \mapsto \Omega^s_t,$$

with the corresponding displacement $\mathbf{u}^s$ and the velocity $\mathbf{v}^s$ given by

$$\mathbf{u}^s(\mathbf{X},t) = \chi^s(\mathbf{X},t) - \mathbf{X}, \tag{2.52}$$

$$\mathbf{v}^s(\mathbf{X},t) = \frac{\partial \chi^s}{\partial t}(\mathbf{X},t). \tag{2.53}$$

The fluid flow is described by the velocity field $\mathbf{v}^f$ defined on the fluid domain Ω^f_t

$$\mathbf{v}^f(\mathbf{x},t) : \Omega^f_t \times [0,T] \mapsto \mathbb{R}^3.$$

Further we define the auxiliary mapping, denoted by ζ^f, to describe the change of the fluid domain and corresponding displacement $\mathbf{u}^f$ by

$$\zeta^f : \Omega^f \times [0,T] \mapsto \Omega^f_t, \tag{2.54}$$

$$\mathbf{u}^f(\mathbf{X},t) = \zeta^f(\mathbf{X},t) - \mathbf{X}. \tag{2.55}$$

We require that the mapping ζ^f is sufficiently smooth, one to one and has to satisfy

$$\zeta^f(\mathbf{X},t) = \chi^s(\mathbf{X},t), \quad \forall(\mathbf{X},t) \in \Gamma^0 \times [0,T]. \tag{2.56}$$

In the context of the finite element method this will describe the artificial mesh deformation inside the fluid region and it will be constructed as a solution to a suitable boundary value problem with 2.56 as the boundary condition.

The momentum and mass balance of the fluid in the time dependent fluid domain according to 2.40 and 2.44 are

$$\rho^f \frac{\partial \mathbf{v}^f}{\partial t} + \rho^f (\nabla \mathbf{v}^f)(\mathbf{v}^f - \frac{\partial \mathbf{u}^f}{\partial t}) = \operatorname{div} \sigma^f \qquad \text{in } \Omega^f_t, \tag{2.57}$$

$$\operatorname{div} \mathbf{v}^f = 0 \qquad \text{in } \Omega^f_t, \tag{2.58}$$

together with the momentum 2.42 and mass 2.36 balance of the solid in the solid domain

$$\rho^s \frac{\partial \mathbf{v}^s}{\partial t} + \rho^s (\nabla \mathbf{v}^s)\mathbf{v}^s = \operatorname{div} \sigma^s \qquad \text{in } \Omega_t^s, \tag{2.59}$$

$$\operatorname{div} \mathbf{v}^s = 0 \qquad \text{in } \Omega_t^s. \tag{2.60}$$

The interaction is due to the exchange of momentum through the common part of the boundary Γ_t^0. On this part we require that the forces are in balance, i.e.

$$\sigma^f \mathbf{n} = \sigma^s \mathbf{n} \qquad \text{on } \Gamma_t^0.$$

Further, we prescribe the no slip boundary condition for the fluid on the interface. This is expressed by

$$\mathbf{v}^f = \mathbf{v}^s \qquad \text{on } \Gamma_t^0. \tag{2.61}$$

The remaining external boundary conditions can be of the following kind. A pressure boundary condition on the fluid inflow and outflow part Γ_t^1

$$\sigma^f \mathbf{n} = p_B \mathbf{n} \text{ on } \Gamma_t^1,$$

with p_B given value. Alternatively we can prescribe a Dirichlet type boundary condition on the inflow or outflow part Γ_t^1

$$\mathbf{v}^f = \mathbf{v}_B \text{ on } \Gamma_t^1,$$

where $\mathbf{v}_B$ is given. The Dirichlet boundary condition is prescribed for the solid displacement at the part Γ_t^2

$$\mathbf{u}^s = \mathbf{0} \text{ on } \Gamma_t^2,$$

and the stress free boundary condition for the solid is applied at the part Γ_t^3

$$\sigma^s \mathbf{n} = \mathbf{0} \text{ on } \Gamma_t^3.$$

We introduce the domain $\Omega = \Omega^f \cup \Omega^s$, where Ω^f, Ω^s are the domains occupied by the fluid and solid in the initial undeformed state, and two fields defined on this domain as

$$\mathbf{u} : \Omega \times [0,T] \to \mathbb{R}^3,$$
$$\mathbf{v} : \Omega \times [0,T] \to \mathbb{R}^3,$$

such that the field $\mathbf{v}$ represents the velocity at the given point and $\mathbf{u}$ the displacement on the solid part and the artificial displacement in the fluid part, taking care of the fact that the fluid domain is changing with time,

$$\mathbf{v} = \begin{cases} \mathbf{v}^s & \text{on } \Omega^s, \\ \mathbf{v}^f & \text{on } \Omega^f, \end{cases}$$

$$\mathbf{u} = \begin{cases} \mathbf{u}^s & \text{on } \Omega^s, \\ \mathbf{u}^f & \text{on } \Omega^f. \end{cases}$$

Due to the conditions 2.56 and 2.61 both fields are continuous across the interface Γ_t^0 and we can define global quantities on Ω as the deformation gradient and its determinant

$$\begin{aligned}\mathbf{F} &= \mathbf{I} + \operatorname{Grad}\mathbf{u},\\ J &= \det\mathbf{F}.\end{aligned}$$

It remains to prescribe some relation for the mapping ζ^f. In terms of the corresponding displacement $\mathbf{u}^f$ we formulate some simple relations together with the Dirichlet boundary conditions required by 2.56, for example

$$\begin{aligned}\frac{\partial \mathbf{u}}{\partial t} &= \Delta\mathbf{u} \quad \text{"mesh moving operator"} && \text{in } \Omega^f,\\ \mathbf{u} &= \mathbf{u}^s && \text{on } \Gamma^0,\\ \mathbf{u} &= \mathbf{0} && \text{on } \Gamma^1.\end{aligned}$$

Using this notation the solid balance laws 2.59 and 2.60 can be expressed in the Lagrangian formulation with the initial configuration Ω^s as reference, cf. 2.43,

$$J\rho^s \frac{d\mathbf{v}}{dt} = \operatorname{Div}\mathbf{P}^s \qquad \text{in } \Omega^s, \tag{2.62}$$

$$J = 1 \qquad \text{in } \Omega^s. \tag{2.63}$$

The fluid equations 2.57 and 2.58 are already expressed in the arbitrary Lagrangian-Eulerian formulation with respect to the time dependent region Ω_t^f, now we transform the equations to the fixed initial region Ω^f by the mapping ζ^f defined by 2.54

$$\rho^f \frac{\partial \mathbf{v}}{\partial t} + \rho^f (\operatorname{Grad}\mathbf{v})\mathbf{F}^{-1}(\mathbf{v} - \frac{\partial \mathbf{u}}{\partial t}) = J^{-1}\operatorname{Div}(J\sigma^f F^{-T}) \qquad \text{in } \Omega^f, \tag{2.64}$$

$$\operatorname{Div}(J\mathbf{v}\mathbf{F}^{-T}) = 0 \qquad \text{in } \Omega^f. \tag{2.65}$$

The complete set of the equations can be written as

$$\frac{\partial \mathbf{u}}{\partial t} = \begin{cases} \mathbf{v} & \text{in } \Omega^s,\\ \Delta\mathbf{u} & \text{in } \Omega^f,\end{cases} \tag{2.66}$$

$$\frac{\partial \mathbf{v}}{\partial t} = \begin{cases} \frac{1}{J\rho^s}\operatorname{Div}\mathbf{P}^s & \text{in } \Omega^s,\\ -(\operatorname{Grad}\mathbf{v})\mathbf{F}^{-1}(\mathbf{v} - \frac{\partial \mathbf{u}}{\partial t}) + \frac{1}{J\rho^f}\operatorname{Div}(J\sigma^f\mathbf{F}^{-T}) & \text{in } \Omega^f,\end{cases} \tag{2.67}$$

$$0 = \begin{cases} J - 1 & \text{in } \Omega^s,\\ \operatorname{Div}(J\mathbf{v}\mathbf{F}^{-T}) & \text{in } \Omega^f,\end{cases} \tag{2.68}$$

2.4.2 Initial Condition

For time-dependent flows, a set of initial conditions at time $t = 0$ is required. We need to prescribe an initial velocity field, i.e.

$$\mathbf{u}(\mathbf{x}, 0) = \mathbf{u}_0(\mathbf{x})$$

In general, we suppose that the elastic stresses in the fluid are zero at time $t = 0$, i.e.

$$\sigma(0) = 0.$$

That means, we assume that the elastic stresses are completely relaxed at the beginning.

2.4.3 Interface Condition

The interaction is due to the exchange of momentum through the common part of the boundary Γ_t^0. The boundary conditions imposed on the blood-vessel wall interface are

$$\sigma^f n = \sigma^s n, \quad \mathbf{v}^f = \mathbf{v}^s, \quad \text{on} \quad \Gamma_t^0, \tag{2.69}$$

where n is a unit normal vector to the interface Γ_t^0. This means the no-slip condition for the flow and that the forces are in balance on the interface Γ_t^0.

2.4.4 Boundary Conditions

Boundary conditions usually come in two distinct variants, Dirichlet conditions which fixes the value of a quantity, and Neumann, also called natural, boundary conditions which specify the in- or out-flux. When modeling fluid flow, Dirichlet conditions uniquely set the velocities on a boundary. That is

$$\begin{aligned} \mathbf{u} &= \mathbf{0}, \quad \mathbf{v} = \mathbf{v}_B && \text{on } \Gamma^1, \\ \mathbf{u} &= \mathbf{0} && \text{on } \Gamma^2, \\ \sigma^s \mathbf{n} &= \mathbf{0} && \text{on } \Gamma^3. \end{aligned}$$

Usually, we set Dirichlet boundary conditions for the velocities at in flow. We have to be aware that it is not possible to simply prescribe arbitrary stress values at in flow, because they have to be consistent with the constitutive equations. Therefore, we usually assume that the elastic stresses are relaxed at in flow.

2.5 Constitutive Equations

Balance laws derived in the previous sections are more general and applicable to all possible FSI cases. For the case of deformable bodies the equations mentioned are certainly not sufficient on their own to determine the material response and are consequently incomplete. From a mathematical point of view they represent an undetermined system. Hence, we must establish additional equations in the form of appropriate constitutive laws which are furnished to specify the ideal real material in question. Constitutive relations relate forces to displacements i.e stress to strain (deformation). Constitutive equations are material dependent.

The concept of constitutive theory is to develop mathematical models representing the real behavior of physical quantity fluid (such as water, oil, air etc.) or solid (such as rubber, metal, ceramics, wood, living tissues etc.).

In this thesis, attempt is not made to conduct a comprehensive review of the large number constitutive theory, rather, only related models are discussed with possible future extensions.

Constitutive equations for fluid and solid are presented in the following subsections, the properties and restrictions accompanying expressed mathematically. However, BVP which will serve as basis for the discretization is documented in the next chapter.

2.5.1 Constitutive Equations for Fluid

As mentioned before the fluid dynamics is a part of an FSI problem. To explain the domain deformation, a moving mesh consideration within the solution of the fluid dynamics is required. In order to manage the dynamics of the fluid domain, moving meshes have to be considered.

The incompressible Newtonian fluids (gases, water, glycerin, and most liquids of low molecular weight under ordinary condition of temperature and pressure), which will be used in this study, are described by the Navier-Stokes equations derived in the ALE framework:

$$\rho^f\left(\frac{\partial \mathbf{v}^f}{\partial t} + \mathbf{v}^f \cdot \nabla \mathbf{v}^f\right) - \operatorname{div} \sigma^f = \mathbf{0}, \quad \operatorname{div} \mathbf{v}^f = \mathbf{0} \quad \text{in} \quad \Omega_t^f, \tag{2.70}$$

here, ρ^f denotes the density of the fluid and σ^f denotes the stress tensor. For incompressible Newtonian fluids the density ρ^f of the fluid will be considered to be a constant in space and time which means velocity is divergence free, i.e. $\operatorname{div} \mathbf{v}^f = \mathbf{0}$, and the stress tensor σ^f is defined by

$$\sigma^f = -p^f \mathbf{I} + \mathbf{T}, \tag{2.71}$$

where p^f is the Lagrange multiplier corresponding to the incompressibility constraint in 2.70, $\mathbf{I}$ is the identity matrix, $-p^f\mathbf{I}$ is also called the inviscid reactive component of Cauchy stress tensor. Here, $\mathbf{T}$ is the active viscous component of the Cauchy stress tensor, which is a function of deformation gradient of velocity, namely,

$$\mathbf{T} = 2\mu^f \mathbf{D},$$

where μ^f is the dynamic viscosity of the fluid and

$$\mathbf{D} = \frac{1}{2}(\nabla \mathbf{v}^f + (\nabla \mathbf{v}^f)^T),$$

is the rate of strain (deformation) tensor. In the following, an overview of what is used in different applications is given which could also be easily implemented into the code.

The Generalized Newtonian Fluid

A fluid for which $\mathbf{T}$ is independent of the history of deformation is known as the Generalized Newtonian Fluid. To derive a model, which is independent of the coordinate system, we write the viscosity η as a function of the invariants of $\mathbf{D}$. We use the symmetry of the rate of deformation tensor by noticing that every symmetric second order tensor can be diagonalized and its eigenvalues are guaranteed to be real. The three principal invariants (I_D, II_D, III_D) of $\mathbf{D}$ are the coefficients of the characteristic polynomial

$$\det(\mathbf{D} - \lambda \mathbf{I}) = -\lambda^3 + I_D\lambda^2 - II_D\lambda + III_D = 0,$$

where they can be expressed in terms of eigenvalues, λ_1, λ_2 and λ_3 of the matrix $\mathbf{D}$.

$$\begin{aligned} I_D &= \mathrm{tr}(\mathbf{D}) = \lambda_1 + \lambda_2 + \lambda_3 \\ \mathit{II}_D &= \frac{1}{2}((\mathrm{tr}\,\mathbf{D})^2 - \mathrm{tr}(\mathbf{D})^2) = \mathrm{tr}(\mathrm{cof}(\mathbf{D})) = \lambda_1\lambda_2 + \lambda_2\lambda_3 + \lambda_3\lambda_1, \\ &= \det(\mathbf{D})\,\mathrm{tr}(\mathbf{D}^{-T}) \qquad \text{if } \mathbf{D} \text{ is invertible} \\ \mathit{III}_D &= \det \mathbf{D} = \lambda_1\lambda_2\lambda_3 \end{aligned}$$

We obtain the following relation between the extra stress tensor and the rate of deformation tensor

$$\mathbf{T} = 2\eta(I_D, \mathit{II}_D, \mathit{III}_D)\mathbf{D},$$

- $I_D = 0$, for incompressible fluids. Then $\mathit{II}_D \leq 0$, $|\mathit{III}_D| \leq \frac{2}{3\sqrt{3}}(-\mathit{II}_D)^{3/2}$.
- $\mathit{III}_D = 0$ for simple shear flow.

The incompressible generalized Newtonian fluid takes the form

$$\mathbf{T} = 2\eta(\mathit{II}_D)\mathbf{D},$$

where $\eta(\cdot)$ is the (nonlinear) viscosity which may depend on the second invariant of the deformation rate tensor II_D.

This model is only suitable for the description of flows, where elastic effects are negligible and the shear-thinning effect has a strong influence on the flow behavior. Its principal usefulness is for calculating flow rates and shearing forces in steady-state simple shear flow such as tube flow, steady cone and plate flow and steady flow between concentric cylinders.

The most commonly prototypical generalized Newtonian fluids models considered are Power-law fluid model, Prandtle-Eyring model, Powell-Erying model, Cross fluid model, Carreau fluid model, Yasuda Model and Second order fluid model. Then, depending on the chosen viscosity function $\eta(\cdot)$ the following prototypical models are considered or could be considered:

Power-law Model

The most widely used form of the general viscous constitutive relation is the **power law model**, because of the number of exact solutions which can be obtained for this model which is

$$\eta(\dot{\gamma}) = K\dot{\gamma}^{\frac{n-1}{2}}, \tag{2.72}$$

where $\eta = \eta(\dot{\gamma}) = \eta(\mathit{II}_D)$ is defined as where K is called the consistency and n is the power law index, both are positive material parameters.

As well as the Newtonian fluid, the generalized Newtonian fluid has zero first and second normal stress differences, but it shows shear-thinning for $n < 1$ or shear thickening for $n > 1$. The viscosity in the limit of vanishing $\dot{\gamma}$ and in the limit of $\dot{\gamma}$ tending to infinity are,

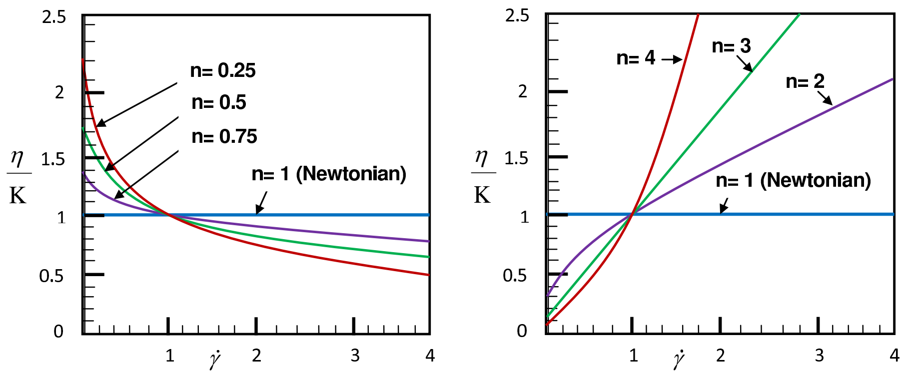

Figure 2.8: Left: Power Law Fluids for $n \leq 1$ (shear thinning or Newtonian), Right: Power Law Fluids for $n \geq 1$ (shear thickening or Newtonian).

- $n < 1:$ $\quad \lim_{\dot{\gamma}\to 0} \eta(\dot{\gamma}) = \infty, \quad \lim_{\dot{\gamma}\to\infty} \eta(\dot{\gamma}) = 0,$
- $n > 1:$ $\quad \lim_{\dot{\gamma}\to 0} \eta(\dot{\gamma}) = 0, \quad \lim_{\dot{\gamma}\to\infty} \eta(\dot{\gamma}) = \infty,$

The unboundedness of the viscosity function and the lack of a non-zero viscosity at zero shear rate does not match experimental results for real fluids and so limits the applicability of the Power-Law model. The power law model is acceptably applied to blood flow and custard flows.

Yasuda Model

Yasuda proposed a model similar to the Cross model but with an extra material constant a with which to fit the data [135]. This five parameter $(\eta_0, \eta_\infty, \lambda, n, a)$ model has sufficient flexibility to fit a wide variety of experimental $\eta(\gamma)$ curves; it has proven to be useful for numerical calculation in which one needs an analytical expression for non-Newtonian viscosity curve. The model is

$$\frac{(\eta - \eta_\infty)}{(\eta_0 - \eta_\infty)} = \frac{1}{(1 + \lambda^a \dot{\gamma})^{\frac{1-n}{2}}} \qquad (\eta_o > \eta_\infty \geq 0, \lambda > 0, n > 1), \tag{2.73}$$

here η_0 is the zero-shear-rate viscosity, η_∞ is the infinite-shear-rate viscosity, λ is a time constant, n is the power-law exponent and a is a dimensionless parameter that describes the transition region between the zero-shear-rate region and the power-law region. Several special cases of the Yasuda model are notable including the Carreau model.

Carreau Model

If a is set to 2 in 2.73, the four constant Carreau model is obtained [19]. It also displays a non-zero bounded viscosity at both upper and lower limits,

$$\frac{(\eta - \eta_\infty)}{(\eta_0 - \eta_\infty)} = \frac{1}{(1+\lambda^2\dot{\gamma})^{\frac{n-1}{2}}} \qquad (\eta_o > \eta_\infty \geq 0, \lambda > 0, n > 1), \tag{2.74}$$

Comments regarding the limiting behavior for the Cross model hold for the Yasuda model as well.

2.5.2 Constitutive Equations for Solid

The material properties of the structures are described by the constitutive equations. These equations establish the relation between the strains **E** and the stresses **S**. Here, the isotropic elastic material model of St. Venant-Kirchhof and a Neo-Hookean model will be considered. It is suitable for problems with large deformations and small strains.

In particular, a non-linear constitutive theory suitable to describe a wide range of physical phenomena in which the strain may be significantly large, i.e. finite is presented in this thesis.

Invariant of Elastic Material

A material is called **Cauchy-elastic or elastic** if the stress field at time t depends only on the state of deformation (and state of temperature) and not on the deformation history (and temperature history) i.e., $\mathbf{F}(\mathbf{X}) = \mathrm{Grad}(\chi(\mathbf{X}))$.

Remark 2.75 *Elastic or Cauchy-elastic material can also be defined via the Cauchy* σ^s *or the first Piola-Kirchhoff stress tensor* $\mathbf{P}^s$.

Remark 2.76 *The actual work done by the stress field on Cauchy-elastic material does, in general depend on deformation path.*

In the following we relate relation in terms of first Piola-Kirchhoff stress tensor $\mathbf{P}^s$. we may express the constitutive equation in general form

$$\mathbf{P}^s = g(\mathbf{F}(\mathbf{X},t),\mathbf{X}),$$

where g is referred to as the **response function** for the second Piola-Kirchhoff stress tensor.

If the first Piola-Kirchhoff stress tensor $\mathbf{P}^s$ and the reference mass density ρ_0 are independent of the position **X**, then

$$\mathbf{P}^s = g(\mathbf{F}),$$

such materials are called **homogeneous**.

We now restrict the strain energy function by a particular property that the material may possess, namely **isotropy**. This property is based on the physical idea that the response of the material, when studied is a stress-strain experiment, is the same in all directions.

We now restrict to a specific elastic material which may be described mathematically, in terms of the constitutive equation for the response function of the second Piola-Kirchhoff tensor by the relation

$$g(\mathbf{FQ}) = \mathbf{Q}^T g(\mathbf{F})\mathbf{Q},$$

which is the material isotropic condition. From the physical point of view the condition of isotropy means that the material exhibits no preferred directions, which mean stress-strain experiment, is the same in all directions irrespective of the choice of reference configuration. For a proof of this crucial relation, based on **the Rivlin-Ericksen representation theorem** see [64] pp. 233-235.

To further establish the representation of the stress tensor, we first ensure that the stress in the reference configuration, which we call the **residual stress**, is zero, i.e.

$$g(\mathbf{I}) = \mathbf{0},$$

we say that the reference configuration is stress-free.

The Green-St. Venant strain tensor $\mathbf{E} = \frac{1}{2}(\mathbf{C} - \mathbf{I})$ is responsible for the deviation of the deformation from a rigid body transformation. After considering the deviation $\hat{g}(\mathbf{I} + 2\mathbf{E}) - \hat{g}(\mathbf{I})$ by making use of Taylor expansion around $\hat{g}(\mathbf{I})$ and manipulation we arrive at (for complete description and proof see [29] Theorem 3.8-1).

$$g(\mathbf{F}) = \hat{g}(\mathbf{C}) = \tilde{g}(\mathbf{E}) = \lambda^s(tr\mathbf{E})\mathbf{I} + 2\mu^s\mathbf{E} + o(\mathbf{E}). \qquad \boxed{2.77}$$

Equation $\boxed{2.77}$ for a frame-indifferent, homogeneous, isotropic, elastic material, whose reference configuration is the natural state (i.e. where the Cauchy stress tensor is zero everywhere) leads to one of the most popular materials in actual computations, **the St.Venant-Kirchhoff material** employs the following constitutive law

$$\sigma^s = \frac{1}{J}\mathbf{F}(\lambda^s(tr\mathbf{E})\mathbf{I} + 2\mu^s\mathbf{E})\mathbf{F}^T \qquad \mathbf{S}^s = \lambda^s(tr\mathbf{E})\mathbf{I} + 2\mu^s\mathbf{E},$$

where λ^s denotes the first **Lamé coefficient**, and μ^s the **shear modulus** of the material and numerical values of the these two constants for a given material found positive by performing special deformations (pure shear, pure traction, pure compression). The material elasticity is also characterized by a set of two other parameters, the **Poisson ratio** ν^s and the **Young modulus** E. These parameters satisfy the following relations

$$\nu^s = \frac{\lambda^s}{2(\lambda^s + \mu^s)} \qquad E = \frac{\mu^s(3\lambda^s + 2\mu^2)}{(\lambda^s + \mu^s)}$$

$$\mu^s = \frac{E}{2(1 + \nu^s)} \quad \lambda^s = \frac{\nu^s E}{(1 + \nu^s)(1 - 2\nu^s)},$$

Here, from $\mu^s, \lambda^s > 0$, it implies that $\mathbf{E} > 0$ and $-1 < \nu^s < 1/2$. The limit case of $\nu^s = 1/2$ is detailed at the end of the description. The St. Venant-Kirchhof model gives identical results to the small deformation isotropic model when the displacements are truly infinitesimal. If small deformations are considered, the difference between the initial and current configurations can be neglected. In the large deformation case it is common to describe the constitutive equation using a stress-strain relation based on the Green Lagrange strain tensor $\mathbf{E}$ and the 2nd Piola-Kirchhoff stress tensor $\mathbf{S}(\mathbf{E})$ as a function of $\mathbf{E}$. However, also incompressible structures can be handled in the same way [75].

Hyperelastic Material

A hyperelastic material is defined as a subclass of an elastic material, whose response function has the form

$$\mathbf{P}^s = g(\mathbf{F}) = \frac{\partial \Psi}{\partial \mathbf{F}}.$$

A so called hyper elastic material (or in the literature often called a Green -elastic material) postulates the existence of a Helmholtz free-energy function Ψ, which is defined per unit reference volume rather per unit mass. The Helmholtz free-energy function Ψ is referred to as the strain-energy function or stored-energy function [71]. $\Psi = \Psi(\mathbf{F})$ is typical example of a scalar-valued function of one tensor variable $\mathbf{F}$, which is assumed to be continuous.

We now restrict attention to homogeneous, isotropic, frame indifferent materials in which the distributions of their internal constituents are assumed to be uniform on the continuum scale. For this type of ideal material the strain-energy function Ψ depends only upon the deformation gradient $\mathbf{F}$. One example of an approximately isotropic material with a wide range of applications is rubber.

For convenience, throughout this thesis we require that the strain-energy function vanishes in the reference configuration, i.e. $\mathbf{F} = \mathbf{I}$. We express this assumption by the normalization condition

$$\Psi = \Psi(\mathbf{I}) = 0. \tag{2.78}$$

From the physical observation we know that the strain-energy function Ψ increases with deformation. In addition to (2.78) we therefore require that

$$\Psi = \Psi(\mathbf{F}) \geq 0. \tag{2.79}$$

Relation (2.78) and (2.79) ensure that the stress in the reference configuration, which we call the residual stress, is zero. We say that the reference configuration is stress-free.

For the behavior at finite strains we require additionally that the scalar-valued function Ψ must satisfy growth conditions. This implies that Ψ tends to $+\infty$ if either $J = \det \mathbf{F}$ approaches $+\infty$ or 0^+. i.e

$$\begin{aligned} \Psi(\mathbf{F}) &\longrightarrow +\infty \qquad \text{as} \qquad \det \mathbf{F} \longrightarrow +\infty, \\ \Psi(\mathbf{F}) &\longrightarrow +\infty \qquad \text{as} \qquad \det \mathbf{F} \longrightarrow 0^+, \end{aligned}$$

physically that means that we would require an infinite amount of strain energy in order to expand a continuum body to the infinite range or to compress it to a point with vanishing volume (for further survey consult the monograph [29, 98]). We specify the Helmholtz potential Ψ and the solid stress is given by

$$\sigma^s = -p^s \mathbf{I} + \rho^s \frac{\partial \Psi}{\partial \mathbf{F}} \mathbf{F}^T, \tag{2.80}$$

the first Piola-Kirchhoff stress tensor is then given by

$$\mathbf{P}^s = -J p^s \mathbf{F}^{-T} + J \rho^s \frac{\partial \Psi}{\partial \mathbf{F}}, \tag{2.81}$$

where p^s is the Lagrange multiplier corresponding to the incompressibility constraint 2.63. The second Piola-Kirchhoff stress tensor takes the form

$$\begin{aligned} \mathbf{S}^s &= -Jp^s\mathbf{F}^{-1}\mathbf{F}^{-T} + J\rho^s\mathbf{F}^{-1}\frac{\partial \Psi}{\partial \mathbf{F}} && (2.82) \\ &= -Jp^s\mathbf{C}^{-1} + 2J\frac{\partial \Psi}{\partial \mathbf{C}}. && (2.83) \end{aligned}$$

The fundamental constitutive equations 2.80, 2.81 and 2.84 are the most general forms used to define incompressible hyperelastic materials at finite strains. The Helmholtz potential can be expressed as a function of different quantities

$$\Psi = \hat{\Psi}(\mathbf{F}) = \hat{\Psi}(\mathbf{I} + \operatorname{Grad}\mathbf{u}),$$

but due to the principle of material frame indifference the Helmholtz potential Ψ depends on the deformation only through the right Cauchy-Green deformation tensor $\mathbf{C} = \mathbf{F}^T\mathbf{F}$ [see 64]

$$\Psi = \tilde{\Psi}(\mathbf{C}). \tag{2.84}$$

A certain coerciveness condition is usually imposed on the form of the Helmholtz potential

$$\bar{\Psi}(\operatorname{Grad}\mathbf{u}(\mathbf{X},t)) \geq a\|\operatorname{Grad}\mathbf{u}(\mathbf{X},t)\|^2 - b(\mathbf{X}), \tag{2.85}$$

where a is a positive constant and $b \in L^1(\Omega^s)$.

Typical examples for the Helmholtz potential used for isotropic materials like rubber are the **Neo-Hookean** model given by

$$\tilde{\Psi} = c_1(I_C - 3),$$

or the **Mooney-Rivlin material**

$$\tilde{\Psi} = c_1(I_C - 3) + c_2(II_C - 3),$$

where $I_C = \operatorname{tr}\mathbf{C}, II_C = \frac{1}{2}((\operatorname{tr}\mathbf{C})^2 - \operatorname{tr}(\mathbf{C})^2), III_C = \det\mathbf{C}$ are the invariants of the right Cauchy-Green deformation tensor $\mathbf{C}$ and c_i are some material constants.

In the case of material anisotropy we can use

$$\tilde{\Psi} = c_1(I_C - 3) + c_2(II_C - 3) + c_3(|\mathbf{F}\mathbf{a}| - 1)^2,$$

with **a** being the preferred material direction. The term $|\mathbf{F}\mathbf{a}|$ represents the extension in the direction **a** and when rewritten as $(a \cdot \mathbf{C}a)^{\frac{1}{2}}$ we can see that it is a function of $\mathbf{C}$. In [79, 80] a similar material relation of the form

$$\tilde{\Psi} = c_1\left(\exp\left(b_1(I_C - 3)\right) - 1\right) + c_2\left(\exp\left(b_2(|\mathbf{F}\mathbf{a}| - 1)\right) - 1\right)$$

has been proposed to describe a passive behavior of the muscle tissue. Adding to any form of Ψ a term like $f(t,\mathbf{x})(|\mathbf{F}\mathbf{a}| - 1)$ one can model the active behavior of a material and then the system can be coupled with additional models of chemical and electric activation of the active response of the tissue, see [93].

2.5.3 Slightly Compressible (Nearly Incompressible) Material

A material which can undergo changes of volume is said to be **compressible** , e.g foamed elastomers are able to sustain finite strain with volume change, required $J > 0$.

A material for which volume changes require a much higher exterior work than volume preserving changes is called a **nearly incompressible** or slightly compressible material, for which the compressibility effects are small. Mathematically,

$$\det \mathbf{F} = 1.$$

In this work we will only use a neo-Hooke law in case of (nearly) incompressible material.

A Neo-Hooke incompressible material:
A Neo-Hooke material model is taken which can be used for compressible or incompressible (for $\nu^s = 1/2 \Rightarrow \lambda^s \to \infty$) material and which is described by the constitutive laws:

$$0 = -\frac{p^s}{\lambda^s} + \frac{1}{2}(J - \frac{1}{J}) \tag{2.86}$$

$$\sigma^s = -p^s \mathbf{I} + \mu^s (\mathbf{F}\mathbf{F}^T - \mathbf{I}). \tag{2.87}$$

By relation 2.86 we need to address a mixed $\mathbf{u}/p$ formulation, or simply mixed formulation, which is advantageous to deal with nearly incompressible and incompressible material at the same time through the Poisson ratio. A mixed formulation then takes the form in limiting case

$$1 = J$$

$$\sigma^s = -p^s \mathbf{I} + \mu^s (\mathbf{F}\mathbf{F}^T - \mathbf{I}).$$

In addition, the formulation can also be applied to the compressible case $(\nu^s \approx 0.4)$ or others.

A Neo-Hookean compressible material ($J = \det \mathbf{F}$)

$$\sigma^s = \lambda^s (J - \frac{1}{J})\mathbf{I} + \frac{\mu^s}{J}(\mathbf{F}\mathbf{F}^T - \mathbf{I})$$

$$\sigma^s = \lambda^s \log(\det \mathbf{F})\mathbf{I} + \frac{\mu^s}{J}(\mathbf{F}\mathbf{F}^T - \mathbf{I})$$

Remark 2.88 *Alternative formulations of the compressible Neo-Hookean model are possible (e.g.* $\sigma^s = \lambda^s \log(J)\mathbf{I} + \frac{\mu^s}{J}(\mathbf{F}\mathbf{F}^T - \mathbf{I})$ *or* $\sigma^s = \lambda^s (J-1)\mathbf{I} + \frac{\mu^s}{J}(\mathbf{F}\mathbf{F}^T - \mathbf{I})$*) which are used in literature and should have similar behavior for small volumetric changes.*

Remark 2.89 *All these models when restricted to small deformations and when linearized lead to this standard linearized Hook's compressible material formula*

$$\sigma^s = \lambda^s(\mathrm{div}\,\mathbf{u}^s)\mathbf{I} + \mu^s(\nabla\mathbf{u}^s + \nabla\mathbf{u}^{sT})$$

which is known as the Navier-Lame equations.

The St. Venant-Kirchhof model gives identical results for the small deformation isotropic model when the displacements are truly infinitesimal. If small deformations are considered, the difference between the initial and current configurations can be neglected.

Both models, the St. Venant Kirchhoff and the Neo-Hooke material model, share the isotropic and homogeneous properties, and both can be used for the computation of large deformations. However, the St. Venant Kirchhoff model does not allow for large strain computation, while the Neo-Hooke model is also valid for large strains. After linearization, both material models have to converge to the same expression, which is then valid only for small strains and small deformations.

With a suitable choice of the material parameters the entropy inequality and the balance of energy is automatically satisfied. The reduced entropy inequality is obtained from 2.51 by using the assumptions of isothermality and incompressibility

$$\rho\frac{d\Psi}{dt} - \mathrm{tr}\,(\sigma\nabla\mathbf{v}) - p\,\mathrm{div}\,\mathbf{v} \le 0. \tag{2.90}$$

For the fluid we have the constitutive equation 2.71 and $\Psi = 0$. Then to satisfy the reduced entropy inequality 2.90 it is sufficient to require

$$\mu > 0. \tag{2.91}$$

In the solid region with the hyper-elastic material assumptions 2.80 and 2.84 the left hand side of the entropy inequality 2.90 is identically equal to 0.

Mathematics are well and good but nature keeps dragging us around by the nose.

Albert Einstein

3

Discretization Methodology

In this chapter, a monolithic ALE formulation of the fluid structure interaction problem derived in chapter 2 will be numerically discretized by the standard Galerkin finite element method in space and time discretization is done via method of Rothe [83]. Before derivations, preliminary definitions will be given which are heart of the proceeding discretization schemes. The time stepping techniques which are used for the non-stationary calculations will be derived. The issues of appropriate space and time discretization techniques shall be addressed.

3.1 Finite Element Method

A finite element method is a numerical technique to obtain an approximate solution to a class of problems governed by elliptic partial differential equations known as boundary value problems as they consist of a partial differential equation and the boundary conditions. The finite element method converts the elliptic partial differential equation into a set of algebraic equations which are easy to solve. Without doubt finite element method has emerged as one of the most powerful numerical method so far devised. The history of finite element is scientifically written in [6].

Advantages of the finite element method over other numerical methods are as follows

- The finite element method can be used for any irregular shaped domain and all types of boundary conditions.
- Domains consisting of more than one material can be easily analyzed.
- Accuracy of the solution can be improved either by proper refinement of the mesh or by choosing approximation of higher degree polynomials.
- The algebraic equations can be easily generated and solved on a computer.
- A general purpose code can be developed for the analysis of a large class of problems.

The standard finite element approximations are based upon the Galerkin formulation of the method of weighted residuals. A general overview of weighted residual formulation and classical Galerkin method are presented in the subsequent sections

3.2 Weighted Residual Formulation

Let $\mathscr{L}$ denote a generic partial differential operator with homogeneous (essential) Dirichlet boundary conditions on Γ. Consider the linear model problem

$$\mathscr{L}u = f \qquad \text{in} \qquad \Omega, \tag{3.1}$$

$$u = 0 \qquad \text{on} \qquad \Gamma. \tag{3.2}$$

A solution u to the equation 3.1 is a sufficiently smooth function that means it must be continuous with continuous partial derivatives of first and second order, satisfying the homogeneous Dirichlet condition on Γ. We replace the equation 3.1 by considering the *weak* (or *variational*) form. Here, the general principles of weighted residual method is briefly described

Method of Weighted Residuals:

1. The problem in form of its residual or *error* is

   $$\mathscr{R}[u] = \mathscr{L}u - f,$$

   here, if u is the exact solution to the problem this implies $\mathscr{R}[u] = 0$, but for an approximate solution $\bar{u} \approx u$, it does not vanish. $\mathscr{R}[u]$ is called the residual or *error* that results from taking $\bar{u}$ instead of the solution u. Here, aim is to select $u \in S$ for which the residual $\mathscr{R}[u]$ is zero.

2. Multiply the residual by a suitable *weighting* (or *test*) function, integrate over the domain Ω and set equal to zero

   $$\int_\Omega w\mathscr{R}[u]\, d\Omega = 0, \qquad \forall w \in W,$$

   where W is the space of weighting functions finishing on the Dirichlet part of the boundary Γ. Mathematically it can be attained if the projection of the residual $\mathscr{R}[u]$ is orthogonal to all test functions $w \in W$. The weak solution belongs to the space S of *trial solutions* satisfying the Dirichlet boundary conditions.

3. Put the residual into the above equation to get the weak form

   $$\int_\Omega w\,(\mathscr{L}u - f)\, d\Omega = 0, \qquad \forall w \in W. \tag{3.3}$$

   Making use of Green's formula of an integration by parts and substitution of the boundary conditions leads to

   $$a(u,w) = \int_\Omega f w d\Omega, \qquad \forall w \in W. \tag{3.4}$$

Evidently, one benefit of using the weighted residual formulation 3.3 is the possibility to shift some derivatives from the trial function u onto the test function w integrating by parts using Green's formula.

3.3 Classical Galerkin Method

The Galerkin method is applicable to larger class of problems as compared to other available methods like of, Collocation, subdomain methods. More recently, Galerkin residual method and Galerkin least squares method have been used with the finite element form of trial solution to give a finite element (Galerkin) residual method.

The method of choice in this thesis for spatial discretization is the classical Galerkin method, a method which is directly applicable to the boundary value problem (BVP) irrespective of the existence of an equivalent extremal formulation. In this subsection the general procedure of classical Galerkin method based on weighted residual method is presented.

3.3.1 Galerkin Finite Element Approximation

To define the weak or variational form of BVP we need to define two classes of functions; the test or weighting functions and the trial or admissible solutions. Here these classes are defined in the context of the standard Galerkin approximation. Let us present the formal definition of function spaces for the test and trial functions for the standard Galerkin formulation.

In general, integrating the product of two functions v and w yields the so called L^2 inner product $(\cdot,\cdot)_0$ which includes the L^2 norm $\|\cdot\|_0$

$$(v,w)_0 = \int_0^1 vw dx, \quad \|v\|_0 = \sqrt{(v,v)_0}.$$

The *test* space W consists of all functions which are square integrable

$$L^2(\Omega) = \left\{ w : \int_\Omega |w|^2 d\mathbf{x} < \infty \right\},$$

have square integrable first derivatives over the domain Ω, that is,

$$H^1(\Omega) = \left\{ w \in L^2(\Omega) : \frac{\partial w}{\partial x_i} \in L^2(\Omega) \, \forall i \right\}$$

and finish on the Dirichlet part Γ_D of the boundary. Thus,

$$W = \left\{ w \in H^1(\Omega) : w = 0 \quad \text{on } \Gamma_D \right\} \equiv H^1_{\Gamma_D}(\Omega).$$

This is a so-called Sobolev space associated with the inner product

$$(u,v)_1 = \int_\Omega \left(uv + \sum_i \frac{\partial u}{\partial x_i} \frac{\partial v}{\partial x_i} \right) d\mathbf{x}$$

which induces the so-called H^1 norm

$$\|u\|_1 = \sqrt{(u,u)_1}.$$

The space of *trial* functions is similar to the test space except that the admissible functions must satisfy the Dirichlet condition on Γ_D, that is,

$$S = \left\{ u \in H^1(\Omega) : u = u_D \quad \text{on } \Gamma_D \right\}.$$

It can be viewed as a translation of the test space W so as to satisfy the Dirichlet conditions on Γ_D. Let $\bar{u}_D$ be an arbitrary function in $H^1(\Omega)$ such that $\bar{u}_D = u_D$ on Γ_D. Then, the test and trial spaces are related as follows:

$$S = W + \{\bar{u}_D\}$$

Consequently it is an affine space. For instance, for $u_D \neq 0$, the sum of two elements of S is not an element of S. However, for homogeneous boundary condition, $u_D = 0$, trial and test spaces coincide

$$W = S = H_0^1(\Omega)$$

The spaces S of trial functions and W of test functions are infinite-dimensional [1]. In order to solve the variational problem with the aid of computers the function spaces are approximated by appropriate finite dimensional subspaces $S^h \subset S$ and $W^h \subset W$, respectively. The general procedure of Galerkin finite element method is as follows.

Galerkin Finite Element Method:

1. Choose a suitable basis $\{\varphi_i(\mathbf{x})\}_{i=1}^N$ for the trial space $S^h \subset S$ such that the approximate solution is written as

   $$u_h(\mathbf{x},t) = \sum_{i=1}^{N} u_i(t)\varphi_i(\mathbf{x})$$

   Here, the basis functions $\varphi_i(\mathbf{x})$ depend only on the spatial variable. For many finite elements, the basis functions are associated with nodes $\mathbf{x}_j$ so that $u_i(t) = u_h(\mathbf{x}_i,t)$ correspond to the nodal solution value which may change in time. This separation of variables simplifies the computation of derivatives significantly. The time derivative is applied to the nodal values u_i, whereas spatial derivatives are applied to the basis functions φ_i.

   - Time derivative $$\frac{\partial u_h(\mathbf{x},t)}{\partial t} = \sum_{i=1}^{N} \frac{\partial u_i(t)}{\partial t}\varphi_i(\mathbf{x})$$
   - Solution gradient $$\nabla u_h(\mathbf{x},t) = \sum_{i=1}^{N} u_i(t)\nabla\varphi_i(\mathbf{x})$$

2. Choose a suitable basis $\{\psi_i(\mathbf{x})\}_{i=1}^N$ for the test space $W^h \subset W$. Choices are

   - $\psi_i = \varphi_i$ which corresponds to the so-called (Bubnov-) Galerkin method or classical Galerkin method which is the method of choice in this thesis.
   - $\psi_i \neq \varphi_i$ is referred to as Petrov-Galerkin method which leads to upwind-type discretizations.

For a comprehensive introduction to the theory of finite elements, see for instance the classical textbooks [36, 81] and the finite elements applications to fluid flow problems is thoroughly discussed in [44, 43, 42].

3.4 Construction of Finite Elements

The basic idea of the Finite element is to subdivide the region $\Omega \subset \mathbb{R}^n$ into subregions. In the 1D case these subregion are intervals, in 2D the subregions are triangles or quadrilaterals and tetrahedron or hexahedron in 3D. In order to compute an approximate solution u_h to the above problem by the finite element method, the computational domain is subdivided into a collection of N_E non-overlapping sub-domains Ω called elements/cells

$$\bigcup_{k=1}^{N_{\mathrm{E}}} \Omega_k \subseteq \Omega \quad \text{and} \quad \Omega_k \cap \Omega_e = 0 \quad \text{for} \quad k \neq e.$$

From the nodal coefficients $u_i(t) = u_h(\mathbf{x}_i, t)$ given at time t the solution values within each element Ω_k can be interpolated by means of local basis functions $\varphi_i^{(k)}$ such that [44]

$$u_h(\mathbf{x}, t) = \sum_{i=1}^{m} u_i(t) \varphi_i^{(k)}, \qquad \forall \mathbf{x} \in \Omega_k$$

where m denotes the number of local degrees of freedom for each element. Summing the local basis functions over all elements one obtains a set of functions $\{\varphi_i\}_{i=1}^{N_m}$ which are used to expand the approximate solution for the whole domain in terms of the nodal coefficients u_i,

$$u_h(\mathbf{x}, t) = \sum_{i=1}^{N_m} u_i(t) \varphi_i(\mathbf{x}), \qquad \forall \mathbf{x} \in \Omega$$

where N_m is the total number of degrees of freedom.

Finally we define a basis function $\varphi_i : \bar{\Omega} \to \mathbb{R}$ for each nodal point x^i in $\bar{\Omega}$, $i = 1, 2, \ldots, n$. These functions must satisfy the general properties of interpolation functions

1. The basis function φ_i takes the value 1 at node $\mathbf{x}_i$ and finishes at all the other nodal points

   $$u_h(\mathbf{x}_j, t) = \sum_{i=1}^{N_m} u_i(t) \varphi_i(\mathbf{x}_j) = u_i(t)$$

   this is followed by

   $$\varphi_i(\mathbf{x}_j) = \delta_{ij} = \begin{cases} 1 & \text{if} \quad j = i \\ 0 & \text{if} \quad j \neq i \end{cases}$$

2. The sum of local basis functions $\varphi_i^{(k)}$ should be identically one for each element Ω_k for consistency. To the global basis functions φ_i unit sums

   $$\sum_{i=1}^{N_m} \varphi_i(x) = 1 \qquad \forall x \in \Omega_k \subset \Omega \tag{3.5}$$

3. For computational efficiency, it is desirable that the local basis function $\varphi_i^{(k)}$ vanishes outside of element Ω_k to obtain a finite element approximation which leads to sparse matrices. As a consequence, the global basis function φ_i turns into a hat function with local support comprising the set of elements meeting at vertex i and equals zero outside.

4. The sum of derivatives finishes in each element followed from the property 3.5

$$\sum_{i=1}^{N_m} \nabla \varphi_i(x) = 0, \qquad \forall \mathbf{x} \in \Omega_k$$

It is worth mentioning that this property does not require the shape functions to be continuous across element boundaries for non-conforming finite elements such as the linear Crouzeix-Raviart element [35] or the rotated bilinear Rannacher-Turek element [107]. The elements can be divided into two groups: elements with continuous pressure (Taylor-Hood family) and elements with discontinuous pressure (Crouzeix-Raviart family). Type of elements which have been studied in finite element literature are triangular, quadrilateral, 3D hexahedral elements, with linear, bilinear, bi-quadratic elements.

In this section we shall construct quadrilateral finite element which is been used.

3.4.1 Quadrilateral Elements

In general applications, quadrilateral elements are favorable above triangular elements, but when the region is irregular or complex geometry then it is hard to approximate easily by quadrilaterals [36]. Also, the derivation of basis functions, element matrices and vectors is more complicated for quadrilateral elements than for triangular elements, except in the case that the boundaries of the elements are curved, because always, even for straight sides an isoparametric transformation is needed. However, the advantage of quadrilateral elements over triangular elements is as follows:

1. Compared to triangular elements, only one half of the number of elements is needed. This reduces the computation time for the construction of matrices and vectors.

2. If we divide a quadrilateral into two triangles, diagonals of the quadrilateral has one of two possible directions. Numerical computations for convective dominant flows, have shown, at least for rectangular grids, that the solution is sensitive to the direction of the diagonal. This sensitivity reduces when size of the elements decreases. Quadrilateral elements do not exhibit this behavior their results are more ”symmetric” for symmetrical problems.

The choice of an element depends on the type of problem, the number of elements desired, the accuracy required, and the available computing time. To begin with, the element must be able to represent derivatives up to the order required in the solution procedure. The simplest way of satisfying the convergence requirements is to use elements that are conforming and, across the element, can adequately represent the function and its derivatives. It needs noting, however, that these conforming may give little increase in accuracy and require a considerable increase in computing time compared to elements with fewer terms. We employed the conforming Q_2P_1 element compromising the computing time for accuracy.

3.4.2 Conformity

The requirement that the representations of the variables and their principal derivatives be continuous is known as the *principal continuity condition*. The reduced continuity condition states that when a nodal value of a variable/derivative is used in a finite element formulation, the values of this variable/derivative at the coincident nodes of adjacent elements should equal this value. This condition is in fact the *compatibility condition* for the elements over the domain and must always be satisfied [97, 36, 28].

In general, the reduced continuity condition is not sufficient to ensure that the principle continuity condition results. If, however, the element definition is such that reduced continuity means that the principal continuity condition applies, the element is said to be conforming (conformable, compatible) for that problem [97].

3.5 Conforming Q_2P_1 Element

We approximate the domain Ω by a domain Ω_h with polygonal boundary and by $\mathscr{T}_h$ we denote a set of quadrilaterals covering the domain Ω_h. We assume that $\mathscr{T}_h$ is regular in the sense that any two quadrilateral are disjoint or have a common vertex or a common edge. By $\overline{T} = [-1,1]^2$ we denote the reference quadrilateral.

Our treatment of the problem as a one system suggests to use the same finite elements on both, the solid part and the fluid region. We have to choose a pair of finite element spaces known to be stable for the problems with incompressibility constraint. We utilize the LBB-stable conforming bi-quadratic, discontinuous bilinear Q_2P_1 pair which is known to be one of the "best" (see [5], [74]), that means most accurate and robust finite element pair for highly viscous incompressible flow computations [50].

The basis function for this element are bi-quadratic polynomials on the reference element for the velocity and linear (discontinuous) polynomials for the pressure. See Figure 3.1 for the location of the degrees of freedom.

We define the usual finite dimensional spaces U for displacement, V for velocity, P for pressure approximation as follows

$$
\begin{aligned}
U &= \{\mathbf{u} \in L^\infty(I,[W^{1,2}(\Omega)]^2), \mathbf{u} = \mathbf{0} \text{ on } \partial\Omega\},\\
V &= \{\mathbf{v} \in L^2(I,[W^{1,2}(\Omega_t)]^2) \cap L^\infty(I,[L^2(\Omega_t)]^2), \mathbf{v} = \mathbf{0} \text{ on } \partial\Omega\},\\
P &= \{p \in L^2(I,L^2(\Omega))\},
\end{aligned}
$$

then the variational formulation of the fluid-structure interaction problem is to find $(\mathbf{u},\mathbf{v},p) \in U \times V \times P$ such that the equations are satisfied for all $(\zeta,\xi,\gamma) \in U \times V \times P$ including appropriate initial conditions. The spaces U,V,P on an interval $[t^n,t^{n+1}]$ would be approximated in the case of the Q_2P_1 pair as

$$
\begin{aligned}
U_h &= \{\mathbf{u}_h \in [C(\Omega_h)]^2, \mathbf{u}_h|_T \in [Q_2(T)]^2 \quad \forall T \in \mathscr{T}_h, \mathbf{u}_h = \mathbf{0} \text{ on } \partial\Omega_h\},\\
V_h &= \{\mathbf{v}_h \in [C(\Omega_h)]^2, \mathbf{v}_h|_T \in [Q_2(T)]^2 \quad \forall T \in \mathscr{T}_h, \mathbf{v}_h = \mathbf{0} \text{ on } \partial\Omega_h\},\\
P_h &= \{p_h \in L^2(\Omega_h), p_h|_T \in P_1(T) \quad \forall T \in \mathscr{T}_h\}.
\end{aligned}
$$

Let us denote by $\mathbf{u}_h^n$ the approximation of $\mathbf{u}(t^n)$, $\mathbf{v}_h^n$ the approximation of $\mathbf{v}(t^n)$ and p_h^n the approximation of $p(t^n)$. Consider for each $T \in \mathscr{T}_h$ the bilinear transformation

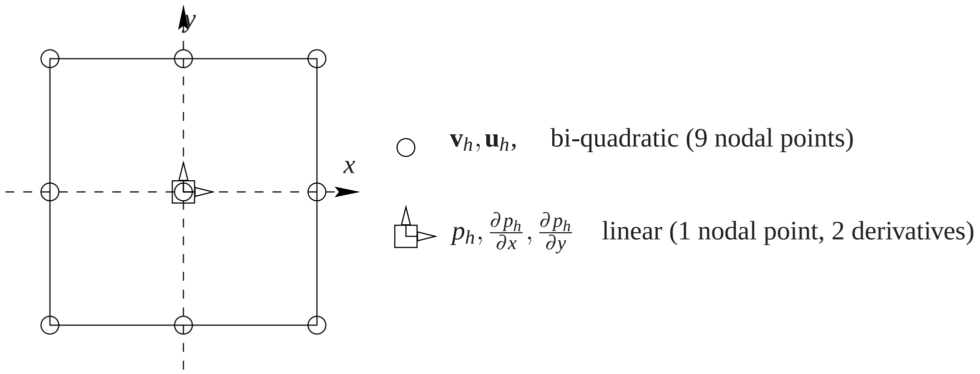

Figure 3.1: Location of the degrees of freedom for the (Crouzeix-Raviart) Q_2P_1 element

$\psi_T : \hat{T} \to T$ to the unit square T. So the local basis on the reference element for $Q_2(T)$ is defined as

$$Q_2(T) = \left\{ q \circ \psi_T^{-1} : q \in \text{span} < 1, x, y, xy, x^2, y^2, x^2y, y^2x, x^2y^2 > \right\}$$

$$\begin{aligned} Q_2(T) = \text{span}\{&(1-x^2)(1-y^2), \frac{1}{2}(1-x^2)(y-y^2), \frac{1}{2}(1-x^2)(y+y^2), \\ &\frac{1}{2}(x-x^2)(1-y^2), \frac{1}{4}(x-x^2)(y-y^2), \frac{1}{4}(x-x^2)(y+y^2), \\ &\frac{1}{2}(x+x^2)(1-y^2), \frac{1}{4}(x+x^2)(y-y^2), \frac{1}{4}(x+x^2)(y+y^2)\}, \end{aligned}$$

with nine local degrees of freedom located at the vertices, midpoints of the edges and in the center of the quadrilateral. The space $P_1(T)$ consists of linear functions defined by

$$\mathrm{P}_1(T) = \left\{ q \circ \psi_T^{-1} : q \in \text{span} < 1, x, y > \right\} \tag{3.6}$$

with the function value and both partial derivatives located in the center of the quadrilateral, as its three local degrees of freedom. The velocity-pressure inf-sup condition is satisfied (see [20]) in the presence of a purely viscous contribution [7]. However, the combination of the bilinear transformation ψ with a linear function on the reference square $P_1(\widehat{T})$ would imply that the basis on the reference square does not contain the full basis. So, the method can at most be first order accurate on general meshes (see [5, 20])

$$||p - p_h||_0 = O(h).$$

The standard remedy is to consider a local coordinate system (ξ, η) obtained by joining the midpoints of the opposing faces of T (see [5, 107, 122]). Then, we set on each element T

$$P_1(T) := \text{span} < 1, \xi, \eta > .$$

For this case, the inf-sup condition is also satisfied and the second order approximation is recovered for the pressure as well as for the velocity gradient (see [20, 62])

$$||p - p_h||_0 = O(h^2) \quad \text{and} \quad ||\nabla(u - u_h)||_0 = O(h^2).$$

For a smooth solution, the approximation error for the velocity in the L_2-norm is of order $O(h^3)$ which can easily be demonstrated for prescribed polynomials or for smooth data on appropriate domains [20].

This choice results to 39 degrees of freedom on an element in the case of our displacement, velocity, pressure formulation in two dimensions and to 112 degrees of freedom on an element in three dimensions. This seem rather prohibitive, especially for a three dimensional computation. The velocity components and pressure gradient in the centroid may be eliminated, reducing the number of velocity degrees of freedom to 16 and number of pressure degrees of freedom to 1.

3.6 Discretization

The initial value problems which consist of a parabolic or hyperbolic differential equation and the initial conditions (besides the boundary conditions) can not be completely solved by the finite element method. The parabolic or hyperbolic differential equations contain the time as one of the independent variables. To convert the time or temporal derivatives into algebraic expressions, another numerical technique like the finite difference method (FDM) is required. Usually, IBVP are discretized first in space, thus getting a system of coupled first order ordinary differential equations in time, strategy is called *semi discrete method*. It remains to integrate the first order ordinary differential equations forward in time which is also known as *method of lines* in numerical analysis literature.

Thus, to solve an initial value problem, one needs both the finite element method as well as the finite difference method where the spatial derivatives are converted into algebraic expressions by FEM and the temporal derivatives are converted into algebraic equations by FDM, Rothe method in this present research [83].

3.6.1 Temporal Discretization

The first step in the numerical discretization process is to choose an appropriate time stepping scheme. It should not only be accurate in time, but also easy to realize and computationally robust and affordable (inexpensive) to use. A simple and flexible choice is the θ-scheme approach, which allows for the use of the single step Backward Euler and Crank-Nicholson schemes, and also multi-step schemes such as the strongly A-stable Fractional-step-θ-scheme. The θ-scheme applied to the monolithic FSI equations for which we need to solve $X = (\mathbf{u}, \mathbf{v}, p)$ at the current time step, $n+1$, with known values only from the previous time step, n.

Basic θ-Scheme: Let us consider an initial value problem of the following form, with $X(t) \in \mathbb{R}^d, d \geq 1$:

$$\begin{cases} \dfrac{dX}{dt} + f(X,t) = 0 \quad \forall t > 0 \\ \qquad X(0) \quad = \quad X_0 \end{cases} \tag{3.7}$$

Given X^n at time $t = t^n$and $k = t_{n+1} - t_n$, then solve for $X = X^{n+1}$

$$X^{n+1} + \theta k f\left(X^{n+1}, t^{n+1}\right) \quad = \quad X^n - (1-\theta) k f(X^n, t^n)$$

The time step k is assumed constant and a parameter θ is to be taken in the interval $[0,1]$.

3.6.2 Explicit Schemes

In the past, explicit time-stepping schemes have been commonly used in non-stationary flow calculations. It possess the severe stability problems and required small time steps prohibit the efficient treatment of long time flow simulations.
Forward Euler-Scheme: (FE, with $\theta = 0$)

$$X^{n+1} + kf(X^n, t^n) \quad = \quad X^n$$

- Implementation and parallelization is easy, low cost per time step
- A good starting point for the development of CFD software
- Small time steps are required for stability reasons, especially if the velocity and/or mesh size are varying strongly
- Extremely inefficient for solution of stationary problems unless local time-stepping i.e. $\Delta t = \Delta t(x)$ is employed
- The required small time steps prohibit the efficient treatment of long time flow simulations

3.6.3 Implicit Schemes

Due to the high stiffness, one should prefer implicit schemes in the choice of time-stepping methods. Since implicit methods have become feasible thanks to more efficient nonlinear and linear solvers, the schemes most frequently used are still either the simple first-order Backward Euler scheme (BE) or more preferably the second-order Crank-Nicholson scheme (CN). These two methods belong to the group of *One-Step-θ-schemes*
Backward Euler-Scheme: (BE, with $\theta = 1$)

$$X^{n+1} + kf\left(X^{n+1}, t^{n+1}\right) \quad = \quad X^n$$

- First order accurate only
- Good choice for steady state calculations
- Strongly A stable, means numerical solution is bounded

Crank-Nicholson-Scheme: (CN, with $\theta = 1/2$)

$$X^{n+1} + \frac{k}{2} f\left(X^{n+1}, t^{n+1}\right) \quad = \quad X^n - \frac{k}{2} f(X^n, t^n)$$

- Second order accurate
- Occasionally suffers from numerical instabilities

- Not strongly A stable, weak damping property

The overall advantages and disadvantages of implicit schemes are as follows

- Stable over a wide range of time steps, sometimes unconditionally
- Constitute excellent iterative solvers for steady-state problems
- Difficult to implement and parallelize, high cost per time step
- Insufficiently accurate for truly transient problems at large Δt
- Convergence of linear solvers deteriorates/fails as Δt increases

Another method which has proven to have the potential to excel in this regard is the Fractional-Step-θ-scheme (FS). It uses three different values for θ and for the time step k at each time level.
Fractional-Step-θ-Scheme: By choosing

$$\theta = 1 - \frac{\sqrt{2}}{2}, \qquad \theta' = 1 - 2\theta, \qquad \alpha = \frac{1-2\theta}{1-\theta}, \qquad \beta = 1 - \alpha$$

it divides the time step in the following consecutive sub steps (with $\tilde{\theta} := \alpha\theta k = \beta\theta' k$):

$$\begin{aligned}
X^{n+\theta} + \tilde{\theta} f\left(X^{n+\theta}, t^{n+\theta}\right) &= X^n - \beta\theta k f\left(X^n, t^n\right) \\
X^{n+1\theta} + \tilde{\theta} f\left(X^{n+1-\theta}, t^{n+1-\theta}\right) &= X^{n+\theta} - \alpha\theta' k f\left(X^{n+\theta}, t^{n+\theta}\right) \\
X^{n+1} + \tilde{\theta} f\left(X^{n+1}, t^{n+1}\right) &= X^{n+1-\theta} - \beta\theta k f\left(X^{n+1-\theta}, t^{n+1-\theta}\right)
\end{aligned}$$

It is a strongly A-stable scheme. Hence, the FS-method possesses the full smoothing property which is important in the case of rough initial or boundary values. Further, it contains only very little numerical dissipation which is crucial in the computation of non-enforced temporal oscillations in the flow. For a rigorous theoretical analysis of the FS-scheme for this special choice of θ see [128]. Therefore, this scheme combines the advantages of both the classical CN-scheme (2nd order accuracy) and the BE-scheme (strongly A-stable), but with the same numerical effort.

A Modified Fractional-Step-θ-Scheme: A modified θ-scheme (see [128, 126]) with macro time step k can be written again as three consecutive sub steps, where $\theta = 1 - 1/\sqrt{2}$, $X^0 = X_0$, $n \geq 0$ and X^n is known:

$$\begin{aligned}
X^{n+\theta} + \theta k f\left(X^{n+\theta}, t^{n+\theta}\right) &= X^n \\
X^{n+1-\theta} &= \frac{1-\theta}{\theta} X^{n+\theta} + \frac{2\theta - 1}{\theta} X^n \\
X^{n+1} + \theta k f\left(X^{n+1}, t^{n+1}\right) &= X^{n+1-\theta}
\end{aligned}$$

As shown in [126], the considerable properties of this θ-scheme are that

- It is fully implicit
- It is strongly A-stable means numerical solution is bounded

- It is second order accurate (in fact, it is ”nearly” third order accurate [126]).

The main difference to the previous ‘classical’ FS scheme is that substeps 1. and 3. look like a Backward Euler step while substep 2. is an extrapolation step only for previously computed data such that no operator evaluations at previous time steps are required.

The pressure term $\nabla p = \nabla p^{n+1}$ may be replaced by $\theta\nabla p^{n+1} + (1-\theta)\nabla p^{n}$, but, with appropriate post processing, both strategies lead to solutions of the same accuracy. In all cases, we end up with the task of solving, at each time step, a nonlinear saddle point problem of given type which has then to be discretized in space.

Summarizing, one obtains that the numerical effort of the modified scheme for each substep is cheaper - at least for ‘small’ time steps (treatment of the nonlinearity) and complex right hand side evaluations while the resulting accuracy is similar. Incidentally, the modified θ-scheme is a *Runge-Kutta* one; it has been derived in [126] as a particular case of the Fractional-Step-θ-scheme.

3.7 Non Dimensionalization

Dimensionless numbers help to identify which physical effects are dominating, and also assist when classifying different model problems. We non-dimensionalize all the quantities by a given characteristic length L and speed V, and the subsequent scaling of the involved variables as follows

$$\begin{aligned} \hat{t} &= t\frac{V}{L}, & \hat{\mathbf{x}} &= \frac{\mathbf{x}}{L}, \\ \hat{\mathbf{u}} &= \frac{\mathbf{u}}{L}, & \hat{\mathbf{v}} &= \frac{\mathbf{v}}{V}, \\ \hat{\sigma}^s &= \sigma^s\frac{L}{\rho^f V^2}, & \hat{\sigma}^f &= \sigma^f\frac{L}{\rho^f V^2}, \\ \hat{\mu} &= \frac{\mu}{\rho^f V L}, & \hat{\Psi} &= \Psi\frac{L}{\rho^f V^2}, \end{aligned}$$

further using the same symbols, without the hat, for the non-dimensional quantities and denoting by $\beta = \frac{\rho^s}{\rho^f}$ the densities ratio. The non-dimensionalized system with the choice of material relations, 2.71 for viscous fluid and 2.81 for the hyper-elastic solid is

$$\frac{\partial \mathbf{u}}{\partial t} = \begin{cases} \mathbf{v} & \text{in } \Omega^s, \\ \Delta\mathbf{u} & \text{in } \Omega^f, \end{cases} \tag{3.8}$$

$$\frac{\partial \mathbf{v}}{\partial t} = \begin{cases} \frac{1}{\beta}\,\mathrm{Div}\left(-Jp^s\mathbf{F}^{-T} + \frac{\partial\Psi}{\partial\mathbf{F}}\right) & \text{in } \Omega^s, \\ -(\mathrm{Grad}\,\mathbf{v})\mathbf{F}^{-1}(\mathbf{v} - \frac{\partial\mathbf{u}}{\partial t}) & \\ \quad + \mathrm{Div}\left(-Jp^f\mathbf{F}^{-T} + J\mu\,\mathrm{Grad}\,\mathbf{v}\mathbf{F}^{-1}\mathbf{F}^{-T}\right) & \text{in } \Omega^f, \end{cases} \tag{3.9}$$

$$0 = \begin{cases} J-1 & \text{in } \Omega^s, \\ \mathrm{Div}(J\mathbf{v}\mathbf{F}^{-T}) & \text{in } \Omega^f, \end{cases} \tag{3.10}$$

and the boundary conditions

$$\sigma^f \mathbf{n} = \sigma^s \mathbf{n} \qquad \text{on } \Gamma_t^0, \tag{3.11}$$

$$\mathbf{v} = \mathbf{v}_B \qquad \text{on } \Gamma_t^1, \tag{3.12}$$

$$\mathbf{u} = \mathbf{0} \qquad \text{on } \Gamma_t^2, \tag{3.13}$$

$$\sigma^f \mathbf{n} = \mathbf{0} \qquad \text{on } \Gamma_t^3. \tag{3.14}$$

We used the weak or weighted residual technique to the governing set of equation which goes as follows

3.8 Weak or Weighted Residual Formulation

Let $I = [0,T]$ denotes the time interval of interest. We multiply the equations 3.8-3.10 by the test functions ζ, ξ, γ such that $\zeta = \mathbf{0}$ on Γ^2, $\xi = \mathbf{0}$ on Γ^1 and integrate over the space domain Ω and the time interval I. Using integration by parts on some of the terms and the boundary conditions we obtain

$$\begin{aligned}\int_0^T \int_\Omega \frac{\partial \mathbf{u}}{\partial t} \cdot \zeta dV dt = & \int_0^T \int_{\Omega^s} \mathbf{v} \cdot \zeta dV dt \\ & - \int_0^T \int_{\Omega^f} \operatorname{Grad} \mathbf{u} \cdot \operatorname{Grad} \zeta dV dt,\end{aligned} \tag{3.15}$$

$$\begin{aligned}\int_0^T \int_{\Omega^f} J \frac{\partial \mathbf{v}}{\partial t} \cdot \xi dV dt + \int_0^T \int_{\Omega^s} \beta J \frac{\partial \mathbf{v}}{\partial t} \cdot \xi dV dt & \\ = - \int_0^T \int_{\Omega^f} & J \operatorname{Grad} \mathbf{v} \mathbf{F}^{-1} (\mathbf{v} - \frac{\partial \mathbf{u}}{\partial t}) \cdot \xi dV dt \\ + \int_0^T \int_\Omega & J p \mathbf{F}^{-T} \cdot \operatorname{Grad} \xi dV dt \\ - \int_0^T \int_{\Omega^s} & \frac{\partial \Psi}{\partial \mathbf{F}} \cdot \operatorname{Grad} \xi dV dt \\ - \int_0^T \int_{\Omega^f} & J \mu \operatorname{Grad} \mathbf{v} \mathbf{F}^{-1} \mathbf{F}^{-T} \cdot \operatorname{Grad} \xi dV dt,\end{aligned} \tag{3.16}$$

$$\begin{aligned}0 = & \int_0^T \int_{\Omega^s} (J-1) \gamma dV dt \\ & + \int_0^T \int_{\Omega^f} \operatorname{Div}(J \mathbf{v} \mathbf{F}^{-T}) \gamma dV dt.\end{aligned} \tag{3.17}$$

Transforming some of the integrals to the current domain the momentum balance equation 3.16 becomes

$$\begin{aligned}\int_0^T \int_{\Omega_t^f} \frac{\partial \mathbf{v}}{\partial t}\cdot \xi\, dvdt + \int_0^T \int_{\Omega_t^s} \beta \frac{\partial \mathbf{v}}{\partial t}\cdot \xi\, dvdt \\ = -\int_0^T \int_{\Omega_t^f} \nabla \mathbf{v}(\mathbf{v} - \frac{\partial \mathbf{u}}{\partial t})\cdot \xi\, dvdt \\ + \int_0^T \int_{\Omega_t} p\, \mathrm{div}\, \xi\, dvdt \\ - \int_0^T \int_{\Omega^s} \frac{\partial \Psi}{\partial \mathbf{F}} \cdot \mathrm{Grad}\, \xi\, dVdt \\ - \int_0^T \int_{\Omega_t^f} \mu \nabla \mathbf{v} \cdot \nabla \xi\, dvdt.\end{aligned} \tag{3.18}$$

This is our method of choice in this study, which also known as the Classical Galerkin residual method.

Now, by following the steps of the classical Galerkin method to the fluid structure interaction main equations. We used the velocity $\mathbf{v}$ as a test function ξ in this equation and obtain the balance of the mechanical energy

$$\begin{aligned}\frac{1}{2}\int_0^T \int_{\Omega_t^f} \frac{\partial}{\partial t} |\mathbf{v}|^2\, dvdt + \frac{\beta}{2}\int_0^T \int_{\Omega_t^s} \frac{\partial}{\partial t} |\mathbf{v}|^2\, dvdt \\ = -\int_0^T \int_{\Omega_t^f} \nabla \mathbf{v}(\mathbf{v} - \frac{\partial \mathbf{u}}{\partial t})\cdot \mathbf{v}\, dvdt \\ - \int_0^T \int_{\Omega^s} \frac{\partial \Psi}{\partial \mathbf{F}} \cdot \mathrm{Grad}\, \mathbf{v}\, dVdt \\ - \int_0^T \int_{\Omega_t^f} \mu\, |\nabla \mathbf{v}|^2\, dvdt.\end{aligned} \tag{3.19}$$

The first term on the left hand side of 3.19 together with the convective term on the right hand side can be rewritten with the help of 2.31 as

$$\begin{aligned}&\frac{1}{2}\int_0^T \int_{\Omega_t^f} \frac{\partial}{\partial t} |\mathbf{v}|^2\, dvdt + \int_0^T \int_{\Omega_t^f} \nabla \mathbf{v}(\mathbf{v} - \frac{\partial \mathbf{u}}{\partial t})\cdot \mathbf{v}\, dvdt \\ &= \frac{1}{2}\int_0^T \int_{\Omega^f} J \frac{\partial}{\partial t} |\mathbf{v}|^2\, dVdt + \int_0^T \int_{\Omega_t^f} \nabla \mathbf{v}(\mathbf{v} - \frac{\partial \mathbf{u}}{\partial t})\cdot \mathbf{v}\, dvdt \\ &= \frac{1}{2}\int_0^T \int_{\Omega^f} \frac{\partial}{\partial t}\left(J |\mathbf{v}|^2\right) dVdt - \frac{1}{2}\int_0^T \int_{\Omega^f} J |\mathbf{v}|^2\, \mathrm{div}\, \frac{\partial \mathbf{u}}{\partial t} dVdt \\ &\quad + \frac{1}{2}\int_0^T \int_{\Omega_t^f} \nabla |\mathbf{v}|^2 (\mathbf{v} - \frac{\partial \mathbf{u}}{\partial t}) dvdt \\ &= \frac{1}{2}\int_0^T \frac{\partial}{\partial t} \int_{\Omega_t^f} |\mathbf{v}|^2\, dvdt + \frac{1}{2}\int_0^T \int_{\Omega_t^f} \mathrm{div}\left(|\mathbf{v}|^2 (\mathbf{v} - \frac{\partial \mathbf{u}}{\partial t})\right) dvdt \\ &= \frac{1}{2}\left[\|\mathbf{v}(t)\|^2_{L^2(\Omega_t^f)}\right]_0^T + \frac{1}{2}\int_0^T \int_{\partial\Omega_t^f} |\mathbf{v}|^2 (\mathbf{v} - \frac{\partial \mathbf{u}}{\partial t}) \cdot \mathbf{n}_{\Omega_t^f}\, dadt, \\ &= \frac{1}{2}\left[\|\mathbf{v}(t)\|^2_{L^2(\Omega_t^f)}\right]_0^T + \frac{1}{2}\int_0^T \int_{\Gamma_t^1} |\mathbf{v}_B|^2\, \mathbf{v}_B \cdot \mathbf{n}_{\Omega_t^f}\, dadt.\end{aligned} \tag{3.20}$$

where we have used the boundary condition 3.12 and the fact that $\frac{\partial \mathbf{u}}{\partial t} = \mathbf{v}$ on Γ^0 and $\frac{\partial \mathbf{u}}{\partial t} = \mathbf{0}$ on Γ^1.

The second term on the right hand side of 3.19 can be rewritten by use of 2.29 as

$$\begin{aligned} \int_0^T \int_{\Omega^s} \frac{\partial \Psi}{\partial \mathbf{F}} \cdot \operatorname{Grad} \mathbf{v} dV dt &= \int_0^T \int_{\Omega^s} \frac{\partial \Psi}{\partial \mathbf{F}} \cdot \frac{d\mathbf{F}}{dt} dV dt \\ &= \int_0^T \int_{\Omega^s} \frac{d\Psi}{dt} dV dt \\ &= \left[\int_{\Omega^s} \Psi(\mathbf{F}(t)) dV \right]_0^T . \end{aligned} \tag{3.21}$$

Using 3.20 and 3.21 in 3.19 with the initial condition 3.11–3.14 and the fact that $\Psi = 0$ in the initial, undeformed state, we obtain

$$\begin{aligned} &\frac{1}{2}\|\mathbf{v}(T)\|^2_{L^2(\Omega^f_T)} + \frac{\beta}{2}\|\mathbf{v}(T)\|^2_{L^2(\Omega^s_T)} + \int_0^T \mu \|\nabla \mathbf{v}\|^2_{L^2(\Omega^f_t)} dt + \int_{\Omega^s} \Psi(\mathbf{F}(T)) dV \\ &= \frac{1}{2}\|\mathbf{v}_0\|^2_{L^2(\Omega^f)} + \frac{\beta}{2}\|\mathbf{v}_0\|^2_{L^2(\Omega^s)} - \frac{1}{2}\int_0^T \int_{\Gamma^1_t} |\mathbf{v}_B|^2 \mathbf{v}_B \cdot \mathbf{n}_{\Omega^f_t} da dt. \end{aligned} \tag{3.22}$$

Using the assumption 2.85, setting $c = \min(1, \beta)$ and considering the homogeneous Dirichlet boundary condition $\mathbf{v}_B = \mathbf{0}$ we finally obtain an energy estimate of the following form

$$\begin{aligned} \frac{c}{2}\|\mathbf{v}(T)\|^2_{L^2(\Omega_T)} &+ \int_0^T \mu \|\nabla \mathbf{v}\|^2_{L^2(\Omega^f_t)} dt + a\| \operatorname{Grad} \mathbf{u}(T)\|^2_{L^2(\Omega^s)} \\ &\leq \|b\|_{L^1(\Omega^s)} + \frac{1}{2}\|\mathbf{v}_0\|^2_{L^2(\Omega^f)} + \frac{\beta}{2}\|\mathbf{v}_0\|^2_{L^2(\Omega^s)}. \end{aligned} \tag{3.23}$$

Here we assume *a priori* that we have the solution and we put it into the weak formulation and choose spaces which have square integrable velocity, displacement and their gradients are also square integrable and can show these norms has to be bounded. It make sense to look in the spaces of square integrable function and their gradients, that spaces are commonly known as Sobolev spaces [1].

Definition 1 *Find* $(\mathbf{u}, \mathbf{v} - \mathbf{v}_B, p) \in U \times V \times P$ *such that equations* 3.15, 3.16 *and* 3.17 *are satisfied for all* $(\zeta, \xi, \gamma) \in U \times V \times P$.

Let us denote by $\mathbf{u}_h^n$ the approximation of $\mathbf{u}(t^n)$, $\mathbf{v}_h^n$ the approximation of $\mathbf{v}(t^n)$ and p_h^n the approximation of $p(t^n)$. Further we will use following shorthand notation

$$\mathbf{F}^n = \mathbf{I} + \operatorname{Grad} \mathbf{u}_h^n, \quad J^n = \det \mathbf{F}^n \quad J^{n+\frac{1}{2}} = \frac{1}{2}(J^n + J^{n+1}),$$

$$(f, g) = \int_\Omega f \cdot g dV, \quad (f, g)_s = \int_{\Omega^s} f \cdot g dV, \quad (f, g)_f = \int_{\Omega^f} f \cdot g dV,$$

f, g being scalars, vectors or tensors.

For simplicity we wrote down the discrete equivalent of the equations for 3.15-3.17 by using Crank Nicholson method, then the variational formulation of the fluid-structure interaction problem is stated as follows

$$
\begin{aligned}
&(\mathbf{u}_h^{n+1},\eta) - \frac{k_n}{2}\Big\{ (\mathbf{v}_h^{n+1},\eta)_s + (\nabla\mathbf{u}_h^{n+1},\nabla\eta)_f \Big\} \\
&\qquad - (\mathbf{u}_h^{n},\eta) - \frac{k_n}{2}\Big\{ (\mathbf{v}_h^{n},\eta)_s + (\nabla\mathbf{u}_h^{n},\nabla\eta)_f \Big\} = 0,
\end{aligned}
\tag{3.24}
$$

$$
\begin{aligned}
&\Big(J^{n+\frac{1}{2}}\mathbf{v}_h^{n+1},\xi\Big)_f + \beta\,(\mathbf{v}_h^{n+1},\xi)_s - k_n\,\big(J^{n+1}p_h^{n+1}(\mathbf{F}^{n+1})^{-T},\operatorname{Grad}\xi\big)_s \\
&+\frac{k_n}{2}\Big\{ \Big(\frac{\partial\Psi}{\partial\mathbf{F}}(\operatorname{Grad}\mathbf{u}_h^{n+1}),\operatorname{Grad}\xi\Big)_s + \mu\,\big(J^{n+1}\operatorname{Grad}\mathbf{v}_h^{n+1}(\mathbf{F}^{n+1})^{-1},\operatorname{Grad}\xi\,(\mathbf{F}^{n+1})^{-1}\big)_f \\
&\qquad + \big(J^{n+1}\operatorname{Grad}\mathbf{v}_h^{n+1}(\mathbf{F}^{n+1})^{-1}\mathbf{v}_h^{n+1},\xi\big)_f \Big\} \\
&\qquad - \frac{1}{2}\,\big(J^{n+1}\operatorname{Grad}\mathbf{v}_h^{n+1}(\mathbf{F}^{n+1})^{-1}(\mathbf{u}_h^{n+1}-\mathbf{u}_h^{n}),\xi\big)_f \\
&\qquad - \Big(J^{n+\frac{1}{2}}\mathbf{v}_h^{n},\xi\Big)_f - \beta\,(\mathbf{v}_h^{n},\xi)_s \\
&+\frac{k_n}{2}\Big\{ \Big(\frac{\partial\Psi}{\partial\mathbf{F}}(\operatorname{Grad}\mathbf{u}_h^{n}),\operatorname{Grad}\xi\Big)_s + \mu\,\big(J^{n}\operatorname{Grad}\mathbf{v}_h^{n}(\mathbf{F}^{n})^{-1},\operatorname{Grad}\xi\,(\mathbf{F}^{n})^{-1}\big)_f \\
&+ \big(J^{n}\operatorname{Grad}\mathbf{v}_h^{n}(\mathbf{F}^{n})^{-1}\mathbf{v}_h^{n},\xi\big)_f \Big\} + \frac{1}{2}\,\big(J^{n}\operatorname{Grad}\mathbf{v}_h^{n}(\mathbf{F}^{n})^{-1}(\mathbf{u}_h^{n+1}-\mathbf{u}_h^{n}),\xi\big)_f = 0,
\end{aligned}
\tag{3.25}
$$

$$
\big(J^{n+1}-1,\gamma\big)_s + \big(J^{n+1}\operatorname{Grad}\mathbf{v}_h^{n+1}(\mathbf{F}^{n+1})^{-1},\gamma\big)_f = 0. \tag{3.26}
$$

Using the basis of the spaces U_h, V_h, P_h as the test functions ζ, ξ, γ we obtain a nonlinear algebraic set of equations. In each time step we have to find $\mathbf{X} = (\mathbf{u}_h^{n+1}, \mathbf{v}_h^{n+1}, p_h^{n+1}) \in U_h \times V_h \times P_h$ such that

$$
\mathscr{F}(\mathbf{X}) = \mathbf{0}, \tag{3.27}
$$

where $\mathscr{F}$ represents the system (3.24–3.26). The solver aspects of this system will be addressed in next Chapter.

3.9 Initial and Boundary Conditions

The modeled FSI applications and physical processes are usually very specific in nature and the studies can thus be confined to a smaller spatial sub region or domain $\Omega \subset \mathbb{R}^d$ and a specific temporal duration $[0,T]$. Both these restrictions will usually greatly simplify the modeling and also reduce the effort required to obtain a solution. It is particularly advantageous to utilize all existing symmetry axes to further shrink the computational domain. Sometimes it is also possible to transform a three dimensional model to two dimensions if the problem can be considered axisymmetric. The drawback of restricting the models spatially is that the equations now have to be supplied with suitable boundary conditions, which are supposed to describe all interactions between and the rest of the non modeled environment. Initial conditions, in the form of specified velocities must be prescribed in addition to the boundary conditions for applications where the temporal evolution is of interest. The equations together with fluid parameters, domain, boundary conditions, and initial conditions all together now uniquely specify the model problem.

A very detailed discussion on boundary and initial conditions for fluid structure interaction problems is found in [6]. We just describe briefly the possible initial and boundary conditions for the problems as follows:

Initial Conditions: For time-dependent or non-stationary problems compulsory initial condition defines the contribution of u at time $t = 0$

$$u(\mathbf{x},0) = u_0(\mathbf{x}), \qquad \forall \mathbf{x} \in \Omega.$$

For stationary simulations it is also advantageous to set a good initial guess so that the nonlinear solver will converge faster.
Boundary Conditions: Usually, boundary conditions are, Dirichlet boundary conditions which sets the value of a quantity, and Neumann, also called natural, boundary conditions which assigns the in- or out-flux. In general, the boundary may consist of different parts

$$\Gamma = \Gamma_{in} \cup \Gamma_{wall} \cup \Gamma_{out},$$

where ($\mathbf{n}$ is the outward pointing unit normal vector at the point $\mathbf{x} \in \Gamma$)

- $\Gamma_{in} = \{\mathbf{x} \in \Gamma : \mathbf{v} \cdot \mathbf{n} < 0\}$ denotes the *inflow* part,
- $\Gamma_{wall} = \{\mathbf{x} \in \Gamma : \mathbf{v} \cdot \mathbf{n} = 0\}$ denotes a *solid wall*,
- $\Gamma_{out} = \{\mathbf{x} \in \Gamma : \mathbf{v} \cdot \mathbf{n} > 0\}$ denotes the *outflow* part.

Typical boundary conditions are as follows:

- *Dirichlet boundary conditions*

  $$u(\mathbf{x},t) = u_D(\mathbf{x},t), \quad \forall \mathbf{x} \in \Gamma_D, \forall t \in (0,T)$$

  That is, Dirichlet conditions set the value of velocity u on the boundary part $\Gamma_D \subset \Gamma$, directly. These conditions are usually prescribed at inlets to set the inflow velocities or to that of the wall which usually has zero velocity.

- *Neumann or natural boundary conditions*

  $$(-p\mathbf{I} + (\nabla u(\mathbf{x},t) + \nabla u(\mathbf{x},t)^T) \cdot \mathbf{n} = \tilde{g}_N(\mathbf{x},t) \quad \forall \mathbf{x} \in \Gamma_N, \forall t \in (0,T)$$

  That is, one can alternatively prescribe the stress at a boundary with the above natural boundary condition. For the special case of a homogeneous Neumann condition ($g_N(\mathbf{x},t) = 0$), or zero stress condition, is commonly used as an outflow boundary condition.

- *No-Slip boundary conditions*

  $$u(\mathbf{x},t) \cdot \mathbf{n} = 0 \quad \text{or} \quad (-p\mathbf{I} + (\nabla u(\mathbf{x},t) + \nabla u(\mathbf{x},t)^T) \cdot \mathbf{n} = 0, \quad \forall \mathbf{x} \in \Gamma_D, \forall t \in (0,T)$$

That is, a combination of Dirichlet and Neumann conditions may be used to specify a so called no-slip or symmetry condition. No-slip boundary condition requires that fluid in contact with the wall stay and move with the wall motion and it should have inclination to stick with the walls.

Expect the best, ready for the worst.

M. A. Jinnah

4

Solvers

If modeling the physical problem is an uphill task then solving it numerically is not that easy in fact even harder. The solution strategies for fluid-structure interaction problems have been the rage for almost two decades, this chapter will sorts it all out with references therein. Furthermore, we will explain the general differences between the direct and iterative solvers. The set of core ideas of iterative solvers like Krylov subspace solver and multigrid solvers strategies will be explained thoroughly with associated references. The methods which have been used will be specifically mentioned.

4.1 Solution Algorithm

After discretization in time by following the foot steps of Rothe method [83] and in space by the standard Galerkin finite element method we arrived at

$$\mathscr{F}(\mathbf{X}) = \mathbf{0} \tag{4.1}$$

which is a set of nonlinear algebraic equations of the form for the unknown vector $\mathbf{X} = (u_h, v_h, p_h)$

$$Mu_h - \frac{k}{2}(M^s v_h + L^f u_h) = \mathrm{rhs}(u_h^n, v_h^n) \tag{4.2}$$

$$\begin{aligned}(M^f + \beta M^s)v_h + \frac{k}{2}N_1(v_h, v_h) + \frac{1}{2}N_2(v_h, u_h)& \\ + \frac{k}{2}(S^s(u_h) + S^f(v_h)) - kB^f(v_h)p_h &= \mathrm{rhs}(u_h^n, v_h^n)\end{aligned} \tag{4.3}$$

$$C^s(u_h) + {B^f}^T(v_h)v_h = \mathrm{rhs}(1, p_h) \tag{4.4}$$

where M is the mass matrix, M^s, M^f are the mass matrices corresponding to the integration over only fluid or solid sub-domains such that $M = M^s + M^f$, N_1 and N_2 represent the convective term in ALE formulation, S^s and S^f are the stress operators (elastic for the solid part and diffusive for the fluid), C is the incompressibility constraint for the solid, B is discrete gradient operator ($B = B^s + B^f$) and L^f is the operator realizing the mesh motion in the fluid domain. All of the operators, apart of the dependences indicated explicitly, also depend on the u_h. The right hand sides depend on the values of the unknowns in the previous time step.

This structure of the system is followed from the weak form of equations (3.24–3.26), derived in the Chapter 3. The involved quantities read as follows:

$$
\begin{aligned}
Mu_h &= \left(\mathbf{u}_h^{n+1}, \eta\right) \\
M^s v_h &= \left(\mathbf{v}_h^{n+1}, \eta\right)_s \\
L^f u_h &= \left(\nabla \mathbf{u}_h^{n+1}, \nabla \eta\right)_f \\
\operatorname{rhs}(u_h^n, v_h^n) &= (\mathbf{u}_h^n, \eta) - \frac{k_n}{2}\left\{ (\mathbf{v}_h^n, \eta)_s + (\nabla \mathbf{u}_h^n, \nabla \eta)_f \right\} \\
M^f v_h &= \left(J^{n+\frac{1}{2}} \mathbf{v}_h^{n+1}, \xi\right)_f \\
M^s v_h &= \left(\mathbf{v}_h^{n+1}, \xi\right)_s \\
N_1(v_h, v_h) &= \left(J^{n+1} \operatorname{Grad} \mathbf{v}_h^{n+1} (\mathbf{F}^{n+1})^{-1} \mathbf{v}_h^{n+1}, \xi\right)_f \\
N_2(v_h, v_h) &= \left(J^n \operatorname{Grad} \mathbf{v}_h^n (\mathbf{F}^n)^{-1} (\mathbf{u}_h^{n+1} - \mathbf{u}_h^n), \xi\right)_f \\
&\quad - \left(J^{n+1} \operatorname{Grad} \mathbf{v}_h^{n+1} (\mathbf{F}^{n+1})^{-1} (\mathbf{u}_h^{n+1} - \mathbf{u}_h^n), \xi\right)_f \\
S^s(u_h) &= \left(\frac{\partial \Psi}{\partial \mathbf{F}} (\operatorname{Grad} \mathbf{u}_h^{n+1}), \operatorname{Grad} \xi\right)_s \\
S^f(v_h) &= \mu \left(J^{n+1} \operatorname{Grad} \mathbf{v}_h^{n+1} (\mathbf{F}^{n+1})^{-1}, \operatorname{Grad} \xi \, (\mathbf{F}^{n+1})^{-1}\right)_f \\
B^f(v_h) &= \left(J^{n+1} p_h^{n+1} (\mathbf{F}^{n+1})^{-T}, \operatorname{Grad} \xi\right)_s \\
\operatorname{rhs}(u_h^n, v_h^n) &= -\left(J^{n+\frac{1}{2}} \mathbf{v}_h^n, \xi\right)_f - \beta \, (\mathbf{v}_h^n, \xi)_s + \frac{k_n}{2}\left\{ \left(\frac{\partial \Psi}{\partial \mathbf{F}} (\operatorname{Grad} \mathbf{u}_h^n), \operatorname{Grad} \xi\right)_s \right. \\
&\quad \left. + \mu \left(J^n \operatorname{Grad} \mathbf{v}_h^n (\mathbf{F}^n)^{-1}, \operatorname{Grad} \xi \, (\mathbf{F}^n)^{-1}\right)_f + \left(J^n \operatorname{Grad} \mathbf{v}_h^n (\mathbf{F}^n)^{-1} \mathbf{v}_h^n, \xi\right)_f \right\} \\
C^s(u_h) &= \left(J^{n+1}, \gamma\right)_s \\
{B^f}^T(v_h) v_h &= \left(J^{n+1} \operatorname{Grad} \mathbf{v}_h^{n+1} (\mathbf{F}^{n+1})^{-1}, \gamma\right)_f \\
\operatorname{rhs}(1, p_h) &= 1.
\end{aligned}
$$

Equivalently, the discrete set of equations (3.24–3.26) can also be written as

$$
\begin{pmatrix} S_{\mathbf{uu}} & S_{\mathbf{uv}} & 0 \\ S_{\mathbf{vu}} & S_{\mathbf{vv}} & kB \\ c_{\mathbf{u}} B_s^T & c_{\mathbf{v}} B_f^T & 0 \end{pmatrix} \begin{pmatrix} \mathbf{u} \\ \mathbf{v} \\ p \end{pmatrix} = \begin{pmatrix} \mathbf{f}_{\mathbf{u}} \\ \mathbf{f}_{\mathbf{v}} \\ f_p \end{pmatrix},
$$

which is a typical nonlinear saddle point problem, where S describes the diffusive and convective terms from the governing equations.

The linearized problem reads

$$
\frac{\partial \mathscr{F}}{\partial \mathbf{X}}(\mathbf{X}) =
\begin{pmatrix}
M - \frac{k}{2} L^f & \frac{k}{2} M^s & 0 \\
\frac{1}{2} \frac{\partial N_2}{\partial u_h} + \frac{k}{2} \frac{\partial (N_1 + S^s + S^f)}{\partial u_h} + k \frac{\partial B}{\partial u_h} p_h & M^s + \beta M^f + \frac{1}{2} \frac{\partial N_2}{\partial v_h} + \frac{k}{2} \frac{\partial (N_1 + S_f^2)}{\partial v_h} & kB \\
B^{sT} + \frac{\partial {B^f}^T}{\partial u_h} v_h & {B^f}^T & 0
\end{pmatrix}
$$

4.2 Nonlinear Solver

The system (4.1) of nonlinear algebraic equations is solved using Newton method as the basic iteration by two ways, either as continuous Newton method on variational level (before discretization), which implies that the continuous Frechet operator can be analytically calculated or by inexact Newton method on matrix level (after discretization) which means that the Jacobian matrix is approximated using finite differences. In the subsequent sections we described the general formulas of Newton method then the more specific definition of the used invariants of Newton methods are given.

4.2.1 Newton's Methods and Its Variants

Consider a vector function $f \in C^1(I)$ and $f^{'}(\mathbf{X}) \neq 0$ for all $\mathbf{X} \in I$, then the standard Newtons iteration formula is

$$\mathbf{X}^{n+1} = \mathbf{X}^n - \frac{f(\mathbf{X}^n)}{f'(\mathbf{X}^n)} \quad \forall n \geq 0. \tag{4.5}$$

The basic idea of the Newton iteration is to find a root of a nonlinear algebraic equation, (4.1) by using the available known function value and its non zero first derivative. Then the standard Newton iteration formula for this nonlinear algebraic system can be formulated as for given $\mathbf{X}^0 \in \mathbb{R}^n$ $n = 1, \dots, n$ until convergence:

$$\text{Solve} \quad J_{\mathscr{F}}(\mathbf{X}^n)\delta\mathbf{X}^n = \mathscr{F}(\mathbf{X}^n) \quad \Rightarrow \quad \delta\mathbf{X}^n = [J_{\mathscr{F}}(\mathbf{X}^n)]^{-1}\mathscr{F}(\mathbf{X}^n) \tag{4.6}$$

$$\text{Set} \quad \mathbf{X}^{n+1} = \mathbf{X}^n + \delta\mathbf{X}^n \tag{4.7}$$

where $\mathbf{X} = (\mathbf{u}_h, \mathbf{v}_h, p_h)$ and $J_{\mathscr{F}}(\mathbf{X}^n) = \frac{\partial\mathscr{F}(\mathbf{X^n})}{\partial\mathbf{X}}$ is the Jacobian matrix. At each step n the solution of linear system with matrix $J_{\mathscr{F}}(\mathbf{X}^n)$ is required. The convergence of this basic iteration can be characterized by the following standard result.

Theorem 6 *Let* $\mathbf{X}$ *be a solution of* $\mathscr{F}(\mathbf{X}) = 0$ *and* $J_{\mathscr{F}}(\mathbf{X}^n) = \frac{\partial\mathscr{F}}{\partial\mathbf{X}}(\mathbf{X}^n)$ *is invertible and locally Lipschitz continuous. Then, if* $\mathbf{X}^0$ *is sufficiently close to* $\mathbf{X}$*, the Newton algorithm has the following property*

$$\|\mathbf{X}^{n+1} - \mathbf{X}\| \leq c\|\mathbf{X}^n - \mathbf{X}\|^2.$$

Proof 3 *For proof see [104] theorem 7.1.*

We can see that this gives us quadratic convergence provided that the initial guess is sufficiently close to the solution. To ensure the convergence globally some improvements of this basic iteration are used which follows in the next section.

4.2.2 Modified Newton's Methods

There are several modification made to the Newton's method in order to reduce the cost when the computed solution is sufficiently close to $\mathbf{X}$.

Inexact Newton It means to solve the system (4.7) by an iterative method in which the admissible iteration is fixed a priori. The schemes are identified as Newton-Jacobi, Newton-SOR or Newton-Krylov methods, according to the iterative process that is used for the linear system in [84]. However, we used the divided differences approximation for Jacobian approximation.

Difference Approximation of the Jacobian On the discrete level the **inexact Newton** method is applied by replacing $J_{\mathscr{F}}(\mathbf{X})$ (whose explicit computation is often expensive), and since we know the sparsity pattern of the matrix in advance, which is given by the used finite element method, it can be computed by finite differences from the residual vector $\mathscr{F}(\mathbf{X})$

$$(J_{\mathscr{F}}(\mathbf{X}^n))_{ij} = \left[\frac{\partial \mathscr{F}}{\partial \mathbf{X}}\right]_{ij}(\mathbf{X}^n) \approx \frac{[\mathscr{F}]_i(\mathbf{X}^n + \alpha_j \mathbf{e}_j) - [\mathscr{F}]_i(\mathbf{X}^n - \alpha_j \mathbf{e}_j)}{2\alpha_j}, \tag{4.8}$$

where $\mathbf{e}_j$ are the unit basis vectors in $\mathbb{R}^n$ and the coefficients $\alpha_j > 0$ are increments to be suitably chosen at each step n of the iteration (4.7) and can be taken adaptively according to the change in the solution in the previous time step. Now the Newton iteration in this case reads

$$\mathbf{X}^{n+1} = \mathbf{X}^n + [J^n_\alpha]^{-1}\mathscr{F}(\mathbf{X}^n), \tag{4.9}$$

the truncation error w.r.t α_j which arise from the divided difference (4.8) can be reduced by reducing the size of α^n_j. However, a too small value of α^n_j can lead of limiting the truncation errors and ensuring a certain accuracy in computations. A possible choice which is been used is

$$\alpha^n_j = -b_* \sqrt{\varepsilon_M}$$

Where b_* parameter to be assigned at start, see [114, 84]. However, the resulting nonlinear and linear solution behavior is quite sensitive w.r.t. the parameters, which will be shown in Chapter 6 in detail in numerical results section. This computation can be done in an efficient way so that the linear solver remains the dominant part in terms of the CPU time (see [122, 128]).

4.2.3 Quasi-Newton's Methods

Quasi-Newton's methods are all those schemes in which globally convergent methods are coupled with Newton-like methods that are only locally convergent, but with an order greater than one. The Quasi-Newton's method for an initial value $\mathbf{X}^0 \in \mathbb{R}^n$ at each step n has the following steps

1. Compute $\mathscr{F}(\mathbf{X}^n)$ by letting $\mathbf{X}^n$ be some starting guess
2. Set the residuum vector $\mathbf{R}^n = \mathscr{F}(\mathbf{X}^n)$ and the tangent matrix $\mathbf{A} = \frac{\partial \mathscr{F}}{\partial \mathbf{X}}(\mathbf{X}^n)$.
3. Solve the linear system for correction $\delta\mathbf{X}$

$$\mathbf{A}\delta\mathbf{X} = \mathbf{R}^n$$

or

$$J_{\mathscr{F}}(\mathbf{X}^n)\delta\mathbf{X}^n = \mathscr{F}(\mathbf{X}^n)$$

4. Find optimal step length ω.
5. Update the solution $\mathbf{X}^{n+1} = \mathbf{X}^n + \omega^n \delta \mathbf{X}^n$,

where ω^n are suitable damping parameters. Here step 4. is the characterizing part of this family of methods. We also used the damped Newton method with line search which is accomplished as follows

The Damped Newton Method with line search improves the chance of convergence by adaptively changing the length of the correction vector (see [122, 75] for more details). The damping parameter $\omega^n \in (-1, 0)$ is chosen such that

$$\mathscr{F}(\mathbf{X}^{n+1}) \cdot \mathbf{X}^{n+1} \leq \mathscr{F}(\mathbf{X}^n) \cdot \mathbf{X}^n.$$

The damping greatly improves the robustness of the Newton iteration in the case when the current approximation $\mathbf{X}^n$ is not close enough to the final solution, see [122, 75] for more details.

By using the solution update step in the Newton method we explain the line search technique here

$$\mathbf{X}^{n+1} = \mathbf{X}^n + \omega^n \delta \mathbf{X}^n, \tag{4.10}$$

where the parameter ω^n is determined such that a certain error measure decreases. One of the possible choices for the quantity to decrease is

$$f(\omega) = \mathscr{F}(\mathbf{X}^n + \omega^n \delta \mathbf{X}^n) \cdot \delta \mathbf{X}^n. \tag{4.11}$$

Since we know from eq 4.11

$$f(0) = \mathscr{F}(\mathbf{X}^n) \cdot \delta \mathbf{X}^n,$$

and taking derivative of 4.11 with respect to ω

$$f'(\omega) = \frac{\partial f(\omega)}{\partial \omega} = \frac{\partial \mathscr{F}}{\partial \mathbf{X}}(\mathbf{X}^n + \omega^n \delta \mathbf{X}^n) \delta \mathbf{X}^n \cdot \delta \mathbf{X}^n$$

$$f'(0) = \left[\frac{\partial \mathscr{F}}{\partial \mathbf{X}}(\mathbf{X}^n) \right] \delta \mathbf{X}^n \cdot \delta \mathbf{X}^n \equiv [J_{\mathscr{F}}(\mathbf{X}^n)] \, \delta \mathbf{X}^n \cdot \delta \mathbf{X}^n, \tag{4.12}$$

making use of 4.7 to 4.12 above equation we reach

$$f'(0) = \mathscr{F}(\mathbf{X}^n) \cdot \delta \mathbf{X}^n,$$

and computing $f(\omega_0)$ for $\omega_0 = -1$ or ω_0 determined adaptively from previous iterations, we can approximate $f(\omega)$ by a quadratic function

$$f(\omega) = \frac{f(\omega_0) - f(0)(\omega_0 + 1)}{\omega_0^2} \omega^2 + f(0)(\omega + 1).$$

Then setting

$$\tilde{\omega} = \frac{f(0)\omega_0^2}{f(\omega_0) - f(0)(\omega_0 + 1)},$$

the new optimal step length $\omega \in [-1,0]$ is

$$\omega = \begin{cases} -\dfrac{\tilde{\omega}}{2} & \text{if } \dfrac{f(0)}{f(\omega_0)} > 0, \\ -\dfrac{\tilde{\omega}}{2} - \sqrt{\dfrac{\tilde{\omega}^2}{4} - \tilde{\omega}} & \text{if } \dfrac{f(0)}{f(\omega_0)} \leq 0. \end{cases}$$

This line search can be repeated with ω_0 taken as the last ω until, for example, $f(\omega) \leq \frac{1}{2} f(0)$. By this safeguarding we can enforce a monotone convergence of the approximation $\mathbf{X}^n$ [84] theorem 3.2.4. If $\omega^n = 1$ then the Quasi Newton method and Newton method are the same and only one iteration is required.

Remark 4.13 *Without line search/damping the Newton's method is only locally convergent. It means it converges only when we are close to the solution. If roots are far away from the solution at start then it is not clear whether it converges or not. These methods (line search or damping) are all methods which make the Newton method globally convergent.*

Remark 4.14 *Trust region methods overcome the problems that line search methods face. The specific trust region methods are presented which effect a smooth transition from the steepest descent direction to the Newton direction in a way that gives the global convergence properties of steepest descent and the fast local convergence of Newton's method in [84] (section 3.3).*

4.3 Linear Solvers

Linear solvers are generally divided into two broad categories, the direct solvers and iterative solvers. The direct methods or solvers are those which in the absence of roundoff error give the exact solution to a linear system after a finite number of steps. Contrarily iterative solvers or methods refer to techniques that computes iterative steps ever better approximation to obtain accurate solutions to a linear system at each step.

In the following subsections, short description of the method of choice for our own problem is given briefly and further references are directed for better understanding.

4.3.1 Direct Solver

In this category, when we have small system for instance (i.e. number of unknowns less than 20.000) then a direct linear solver for sparse systems like UMFPACK (see [40]) is preferably used, which appears to be a good candidate, at least in 2D. Moreover this choice provides very robust linear solvers, however its memory and CPU time requirements are too high for larger systems.

In the next paragraph brief insight of UMFPACK is given

UMFPACK is a set of routines for solving unsymmetric sparse linear systems,

$$\mathbf{AX} = \mathbf{b}, \tag{4.15}$$

by using the Unsymmetric-pattern MultiFrontal method and direct sparse LU factorization. The sparse matrix **A** can be square or rectangular, singular or non-singular, and real or complex (or any sort). Only square matrices **A** can be used to solve (4.15) or related systems. However rectangular matrices can only be factorized.

It is written in ANSI/ISO C, with a MATLAB interface and relies on the Level-3 Basic Linear Algebra Subprograms (dense matrix multiply) for its performance. This code works on Windows and many versions of Unix (Sun Solaris, Red Hat Linux, IBM AIX, SGI IRIX, and Compaq Alpha). A short introduction to Unix users of the C interface of UMFPACK is reported in [41, 39].

4.3.2 Iterative Solvers

Iterative solvers further divided and categorized into two major broad classes, namely Krylov Subspace solvers and Multigrid solver. In the following subsection general description of these methods documented and the solution algorithm to solve very own FSI problem is incorporated. For detail insight on the iterative methods one may go through [114].

Krylov Subspace Solver

Possibly the large linear problems can be solved by Krylov-space methods (BiCGStab, GMRes, see [8]) with suitable preconditioners. One possibility is the ILU preconditioner with special treatment of the saddle point character of our system, where we allow certain fill-in for the zero diagonal blocks, see [22].

Here, we describe the very basic detail of Krylov subspace method and associated preconditioners in similar order in the following two paragraphs.

The Krylov subspace methods are considered currently among the most important iterative techniques available for solving large linear systems. These techniques are based on projection processes, both orthogonal and incline, onto Krylov subspaces, which are subspaces spanned by vectors of the form $p(A)v$ where p is a polynomial. Precisely, theses techniques approximate $\mathbf{A}^{-1}b$ by $p(\mathbf{A})b$, where p is good polynomial. Because the vectors tend very quickly to become almost linearly dependent, methods relying on Krylov subspace frequently involve some orthogonalization scheme, such as Lanczos iteration for Hermitian matrices or Arnoldi iteration for more general matrices [114]. A general projection method for solving the linear system (4.15) is a method which seeks an approximate solution x_m from an affine subspace $x_0 + K_m$ of dimension m under the condition

$$b - \mathbf{A}x_m \perp L_m$$

where L_m is another subspace of dimension m. Here, x_0 represents an arbitrary initial guess to the solution. A **Krylov subspace** method is a method for which the subspace K_m is the Krylov subspace

$$K_m(\mathbf{A}, r_0) = span\left\{r_0, \mathbf{A}r_0, \mathbf{A}^2 r_0, \ldots, \mathbf{A}^{m-1} r_0\right\},$$

where $r_0 = b - \mathbf{A}x_0$. For simplicity $K_m(\mathbf{A}, r_0)$ will be denoted by K_m. The different versions of Krylov subspace methods arise from different choices of the subspaces L_m and importantly from the ways in which the system is preconditioned.

It is clearly seen that the approximations obtained from a Krylov subspaces methods are of the form from the approximation theory point of view,

$$\mathbf{A}^{-1}b \approx x_m = x_0 + q_{m-1}(\mathbf{A})r_0,$$

in which q_{m-1} is a certain polynomial of degree $m-1$. In the simplest case where $x_0 = 0$, then

$$\mathbf{A}^{-1}b \approx q_{m-1}(\mathbf{A})b.$$

In other words, $\mathbf{A}^{-1}b$ is approximated by $q_{m-1}(\mathbf{A})b$.

Although all the techniques provide the same type of polynomial approximations, the choice of L_m, i.e., the constraints used to build these approximations, will have an important effect on the iterative technique. Two broad choices for L_m give rise to the best known techniques [114].

1. The first is simply $L_m = K_m$ and the minimum-residual variation $L_m = \mathbf{A}K_m$. A few of the numerous methods in this category are the Arnoldi, the symmetric Lanczos, Conjugate gradient, GMRES (generalized minimum residual), the Conjugate residual method, GCR, ORTHOMIN, and ORTHODIR methods.
2. The second class of methods is based on defining L_m to be a Krylov subspaces methods associated with $\mathbf{A}^T$, namely, $L_m = K_m(\mathbf{A}^T, r_0)$. Methods of this class are Lanczos Bi orthoganalization, BiCG, QMR (quasi minimal residual), BiCGSTAB (biconjugate gradient stabilized), TFQMR (transpose-free QMR), and MINRES (minimal residual) methods.

There are also block extensions of each of these methods termed block Krylov subspace methods, see [114] for further comprehensive survey of each of the above sub methods.

Preconditioning Preconditioning is a key ingredient for the success of Krylov subspace methods in the applications to follow in next chapter and many other engineering applications.

It is well fact that iterative solver keep inherent robustness/stability issues compare to direct solvers. Although, they are applicable to large linear system but stability related issues restrict the wide use of iterative solvers in many industrial applications.

It is well observed that, lack of robustness is a widely recognized weakness of iterative solvers, relative to direct solvers, which damage the acceptance of iterative methods in industrial application despite their applicability for very large linear systems. To circumvent this, both the efficiency and robustness of iterative techniques can be improved by using preconditioning. Preconditioning is simply means of transforming the original linear system into one which has the same solution, but which is likely to be easier to solve with an iterative solver. In general, the reliability of iterative techniques, when dealing with various applications, depends much more on the quality of the preconditioner than on the the particular Krylov subspace accelerator used. Finding a good preconditioner to solve a given sparse linear system is often viewed as combination of art and science. Theoretical results are rare and some methods work surprisingly well, often above expectations. A preconditioner can be defined as an supplementary approximate solver which is combined with an outer iteration technique, typically one of the Krylov subspace iterations. We employed the most successful techniques used to precondition a sparse linear system arrive in our problem. However, common feature of the preconditioners are built from the original coefficient matrix. Roughly speaking, a preconditioner is any form of implicit or explicit modification of an original linear system which make it easier to solve by a given iterative methods.

For example, scaling all rows of a linear system to make the diagonal system to make the diagonal elements equal to one is an explicit form of preconditioning. The resulting system can be solved by a Krylov subspace method and may require fewer steps to converge than with original system (although this is not guaranteed).

One of the simplest ways of defining a preconditioner is to perform an incomplete factorization of the original matrix **A**. This implies a decomposition of the form $\mathbf{A} = \mathbf{LU} - \mathbf{R}$ where **L** and **U** have the same nonzero structure as the lower and upper parts of **A** respectively and **R** is the residual or error of factorization.

Zero fill-in ILU(0)

The incomplete $\mathbf{L}U$ factorization technique with no fill-in, denoted by $\mathbf{ILU}(0)$, consists of taking the zero pattern p to be precisely the zero pattern of **A**. By definition , together the **L** and **U** matrices in $\mathbf{ILU}(0)$ have the same number of nonzero elements as the original matrix **A**, see [114] 10.3.2.

This incomplete factorization is rather easy and inexpensive to compute. On the other hand, it often leads to a crude approximation which may result in the Krylov subspace accelerator requiring many iteration to converge. To circumvent this, several alternative incomplete factorization have been developed by allowing more fill-in in **L** and **U**. In general, the more accurate **ILU** factorizations require fewer iterations to converge, but the preprocessing cost to compute the factors is high [114].

Level of fill and ILU(P)

The accuracy of the $\mathbf{ILU}(0)$ incomplete factorization may be insufficient to yield an adequate rate of convergence [114] example 10.2. More accurate incomplete $\mathbf{L}U$ factorizations are often more efficient as well as more reliable. These more accurate factorizations will differ from $\mathbf{ILU}(0)$ by allowing some fill-in. Thus, $\mathbf{ILU}(1)$ keeps the first order fill-in, a term which is explained in [114] 10.3.3. There are few drawbacks to the $\mathbf{ILU}(p)$.

- The amount of fill-in and computational work to get the $\mathbf{ILU}(p)$ factorization is not predictable for $p > 0$.
- The cost of updating the levels can be quite high.

Most importantly, the level of fill-in for indefinite matrices may not be a good indicator of the size of the elements that are being dropped. This normally leads to large number of iteration to achieve the convergence. The popular strategies to circumvent this issue are Modified $\mathbf{ILU}(\mathbf{MILU})$ factorization and **ILUT** strategies.

Historically, incomplete factorization preconditioners were developed for the regular structure matrices, rather than for general sparse matrices [114].

Multigrid Solver

Multigrid methods were invented for partial differential equation such as Poisson's equation, however they work on wider class of problems too. In contrast to other iterative methods discussed before, multigrid's convergence rate is independent of the problem size N. For a general introduction to multigrid we refer to the book of Hackbush [66].

As an alternative, we also utilized an efficient standard geometric multigrid approach to solve the discretized fluid structure interaction problem which is based on a hierarchy of grids obtained by successive regular refinement of a given coarse mesh which is today one of the the fastest iterative linear solvers for CFD problems, (see [133]). Inside multigrid, restriction is applied to the residual after smoothing on all mesh levels and a direct sparse linear solver [40] is utilized to obtain the coarsest grid solution, if the number of degrees of freedom is sufficiently small. Prolongation is then applied which is followed by post-smoothing to give a better approximation. These steps continue until a V or F-cycle of multigrid iterations is finished.

To explain how multigrid works, we need some operators that take a problem one one grid level and either improve it or transform it to a related problem on another grid.

In the following we describe a prototypical multigrid procedure to solve the linear system $A_i u_i = b_i$, which contains the following steps:

1. Start with an initial guess on fine grid level i, u_i^0, execute $j = 0, \dots, m-1$ presmoothing steps to get a more accurate iterate

   $$u_i^{j+1} = \mathbf{S}_i(u_i^j).$$

   The smoothing operator $\mathbf{S}_i$ essentially computes a first improved approximation to $\mathbf{A}_i u_i = b_i$.

2. The presmoothing steps should have "smoothed/damped" the high frequency components of the error/residual sufficiently so that the remaining error will be seen as having a high frequency on a coarser grid. So to speak, The variation of Jacobi's method makes the solution smoother, which is equivalent to getting rid of high frequency error. Calculate the residual and restrict it to a coarser grid

   $$r_{i-1} = \mathbf{R}_i^{i-1}(b_i - A_i u_i^m)$$

   where $\mathbf{R}_i^{i-1}$ is the restriction operator from the fine grid level i to the coarser grid level $i-1$, which is an approximation on the coarser grid.

3. Solve recursively on the coarse grid system

   $$A_{i-1} u_{i-1}^* = r_{i-1}$$

   to get the correction u_{i-1}^*.

4. Prolongate the calculated correction to the next finer grid level and apply

   $$u_i^{m+1} = u_i^m + \alpha_i \mathbf{P}_{i-1}^i u_{i-1}^*,$$

   where α_i is a suitably chosen damping parameter and $\mathbf{P}_{i-1}^i$ is the prolongation or interpolation operator from grid level $i-1$ to level i.

5. Execute $l = 0, \dots, n-1$ number of postsmoothing steps (likewise in step 1) to get the final solution u_i^{m+1+n}.

It is common to apply these steps recursively on a succession of grid levels to achieve a faster reduction of error. Appropriate algorithms now have to be chosen for the prolongation, restriction, smoother, and solver components to achieve full efficiency. The basic idea of construction of MGV and MGF which is been part of MG is as follows

Multigrid V-Cycle (MGV) The basic multigrid V-cycle algorithm states

```
                 Multigrid V-Cycle (MGV)

function $MGV(b^i, u^i)$      ...replace an approximate solution $u^i$
                                ...of $A_i u_i = b_i$ with an improved one

if $i = 1$ ...only one unknown
compute the exact solution $u^1$ of $Prob^1$
return $u^1$
else
    1. $u^i = \mathbf{S}(b^i, u^i)$                  ...improve the solution
    2. $r^i = \mathbf{A}^i \cdot u^i - b^i$              ...compute the residual
    3. $d^i = \mathbf{P}(MGV(\mathbf{R}(r^i), 0)$       ...solve recursively on coarser grid level
    4. $u^i = x^i - d^i$                     ...correct fine grid solution
    5. $u^i = \mathbf{S}(b^i, u^i)$                  ...improve the solution again
return $u^i$
endif
```

The algorithm is called a V-cycle, because if we draw it schematically in (grid number *i*, time) space, with a point for each recursive call to MGV. The multigrid cycles looks like in Figure. 4.1. Although, W-cycles are usually more robust and they are easier to analyze in the classical multigrid convergence theory. However, they are more expensive and in local refinement applications they may fail to have optimal work count.

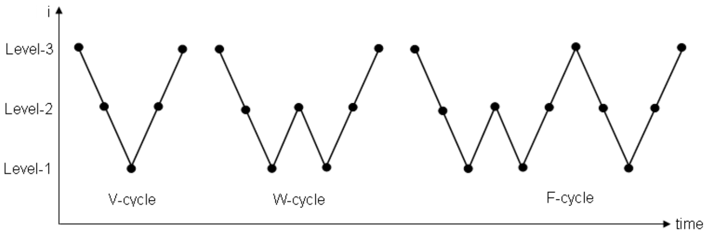

Figure 4.1: Multigrid V, W, F cycles from left to right

W-cycles are especially expensive in parallel algorithms when frequent coarse grid visits leads to poor processor utilization. Either V- or W-cycles can (and should be) used in FMG. However, we used the V-cycle for the calculations.

Full Multigrid (FMG) The ultimate multigrid algorithm which uses the MGV as a building block and known as full multigrid (FMG) is employed and states.

Multigrid F-Cycle (FMG)

```
function $MGF(b^i, u^i)$        ...return an accurate solution $u^i$ of $A_i u_i = b_i$
solve $A_1 u_1 = b_1$ exactly to get $u^1$
for $i = 2$ to $k$
$u^i = MGV(b^i, \mathbf{P}(u^i))$
end for
```

A picture of FMG in (grid number i, time) space is shown in 4.1. There is one ”V” in this picture for each call to MGV in the inner loop of FMG. We used interpolation operators for the prolongation and restriction routines as are normally constructed as pure interpolation operators. There are other alternative approaches like discrete L^2-projection operators and others, which has been developed for highly anisotropic grids, is to embed appropriate weighting in the operators to properly account for the anisotropies [106]. This approach is potentially advantageous for two-phase flow simulations since the discontinuous density and viscosity fields can be interpreted as anisotropies.

Advantages The idea behind multigrid is to assemble and iteratively solve the linear systems on a sequence of grids. This allows for the slowly converging low frequency errors on the finest grid to quickly be filtered out on the coarser grids (the low frequency error is seen as having a higher frequency on the coarser grids). A near linear efficiency can in this way be achieved in the optimal case (with linear meaning that the cost of solving the systems increase linearly with the number of degrees of freedom) [66]. This is in contrast to standard iterative solvers which require an increasing number of iterations to converge as the computational grids are refined.

Coupled Multigrid with Vanka-type Smoothing This type of multigrid smoothers has been originally introduced by Vanka [130] for solving the Navier-Stokes equations discretized by finite differences. The smoother is sometimes denoted as symmetrically coupled Gauss-Seidel (SCGS) [130] or box iteration/relaxation [133]. The Vanka technique has especially been developed to deal with saddle point systems exhibiting a zero block appearing on the diagonal of the system matrix, where standard (point-wise) Jacobi or Gauss-Seidel smoothers fail. Stokes and linearized Navier-Stokes systems belong to this category which is the main reason for the strong influence the method had (and still has) in the field of computational fluid dynamics (CFD) and fluid-structure interaction (FSI) is obviously not the different. Other reasons are that it can be implemented with the help of elementary techniques available in all finite element packages and that it is efficient and robust for a wide class of problem configurations. The main idea of the Vanka approach is to directly couple all field variables, i. e., velocity, displacements and pressure in our case, on a local level, resulting in small coupled systems that have to be solved successively.

We used on finer levels a fixed number of smoothing steps of iterations by local MPSC schemes (Vanka-like smoother) which acts locally in each element Ω_i on all levels [122, 130, 75]. Such iterations can be written as

$$\begin{pmatrix} \mathbf{u}^{l+1} \\ \mathbf{v}^{l+1} \\ p^{l+1} \end{pmatrix} = \begin{pmatrix} \mathbf{u}^{l} \\ \mathbf{v}^{l} \\ p^{l} \end{pmatrix} - \omega^l \sum_{\Omega_i} \begin{pmatrix} S_{\mathbf{uu}|\Omega_i} & S_{\mathbf{uv}|\Omega_i} & 0 \\ S_{\mathbf{vu}|\Omega_i} & S_{\mathbf{vv}|\Omega_i} & kB_{|\Omega_i} \\ c_{\mathbf{u}}B^T_{s|\Omega_i} & c_{\mathbf{v}}B^T_{f|\Omega_i} & 0 \end{pmatrix}^{-1} \begin{pmatrix} \mathbf{def}^l_{\mathbf{u}} \\ \mathbf{def}^l_{\mathbf{v}} \\ def^l_p \end{pmatrix}.$$

The inverse of the local systems (39 × 39) can be done by hardware optimized direct solvers. The full nodal interpolation is used as the prolongation operator $\mathbf{P}$ with its transposed operator used as the restriction $\mathbf{R} = \mathbf{P}^T$ [73, 122].

Idea Behind Vanka-type Smoothers The primitive idea of Vanka-type smoothers is to divide the mesh into small subregions Ω_i and treat them separately. One smoothing step consists of a loop over all these Ω_i's, where steps to be followed in each iteration are

1. Assemble a small local matrix from the global matrix which constitute the number of unknowns to the current subregions.
2. Construct associated local residual which is done via **ILU** method, i. e., information, which has been updated in previously treated subregions, is immediately incorporated into the assembly process of the current local residual.
3. Solve the resulting system with the local residual as right hand side. Note that the resulting local matrices are always invertible. The associated boundary conditions are incorporated accordingly. A direct solver is employed to invert the local systems.
4. Update the corresponding parts of the global solution with this local correction.

This is a general description of the Vanka process. In this thesis we used the Element-based Vanka smoother for the FSI problem. Their numerical studies are reported in [134] in detail with highlighting the general drawbacks and advantages with respect to isotropic meshes, aspect ratios, relaxation parameter and materials under consideration.

Survey on Vanka-type Smoothers Although there is not much literature found on the theoretical aspects of Vanka-type smoothing but enough literature can be found presenting numerical studies in the context of the discretised Navier-Stokes equations in CFD [91, 94, 117]. In all these numerical test cases, the smoother is extensively tested on the benchmark configuration 'flow around a cylinder' [127, 122] for the steady and unsteady state. Ouazzi and Turek [99] transfer the Vanka idea to edge-oriented storage- and stabilization techniques for the Navier-Stokes equations. For further references, see the overview paper of Wesseling and Oosterlee [133] and comparative solver studies including Vanka smoothers in [122]. Hron and Turek [75] employ Vanka smoothers to solve coupled systems arising from the Q_2P_1 discretization of fluid structure interaction problems which is been employed in this thesis.

Part II

Numerical Results And Future Insight

The fool collects facts; wise man selects them.

John Wesley Powell

5

Numerical Applications

It is well known that every mathematical modeling is done for the real life physical phenomena and later numerical simulation are based on it. Our is not different, we applied the proposed mathematical model to wide range of real life application from engineering to biomechanics. In this chapter validation of the proposed method for well known numerical benchmark will be made. This chapter will be divided into three sections based on three different applications, namely, the benchmarking and validation of the code, experimental benchmark calculations and the hemodynamics aneurysm application.

5.1 FSI Benchmarking

This benchmark settings are described in a way for the rigorous evaluation of different methods to test and compare numerical methods and codes for fluid-structure interaction problems. It is based on the older successful DFG *flow around cylinder* benchmark developed in [127] for incompressible laminar fluid flow. The configurations consist of laminar incompressible channel flow around an elastic object which results in self-induced oscillations of the structure while the deformation of the structure should be significant. The fluid is assumed to be incompressible while the structure is allowed to be compressible or incompressible. The mathematical modeling is done in Chapter 2. Moreover, characteristic flow quantities and corresponding plots are provided for a quantitative comparison.

The overall setup of the interaction problem is such that the solid object with elastic part is submerged in a channel flow. Then, self induced oscillations in the fluid and the deformable part of the structure are obtained so that characteristic physical quantities and plots for the time-dependent results are provided (see [124, 125, 111], for more detail).

The results and experience gained from this benchmark setting will provide invaluable experience and data that will go into the development of a large scale, sophisticated, accurate and reliable simulation model.

5.1.1 Definitions

Although, rigorous mathematical formulation of this benchmark scenario is described in Chapter 2, however, in the subsequent sections we will define briefly the configuration in which the flow of an **incompressible Newtonian fluid** interacting with an **elastic solid** is considered.

Fluid Properties

The fluid is considered to be **Newtonian**, **incompressible** and its state is described by the velocity and pressure fields $\mathbf{v}^f, p^f$. The balance equations are

$$\left.\begin{aligned} \rho^f \frac{\partial \mathbf{v}^f}{\partial t} + \rho^f (\nabla \mathbf{v}^f)\mathbf{v}^f &= \operatorname{div} \sigma^f \\ \operatorname{div} \mathbf{v}^f &= 0 \end{aligned}\right\} \qquad \text{in } \Omega_t^f.$$

The material constitutive equation is

$$\sigma^{\mathbf{f}} = -p^f \mathbf{I} + \rho^f \nu (\nabla \mathbf{v}^f + \nabla \mathbf{v}^{f^T}).$$

The constant density of the fluid is $\rho^f = 1$ and the viscosity is denoted by ν. The Reynolds number is defined by $\mathrm{Re} = \frac{2r\bar{V}}{\nu}$, with the mean velocity $\bar{V} = \frac{2}{3} v(0, \frac{H}{2}, t)$, r radius of the cylinder and H height of the channel (see Fig. 5.1).

Structure Properties

The structure is assumed to be **elastic**, and either **incompressible** or **compressible**. Its configuration is described by the displacement $\mathbf{u}^s$, with velocity field $\mathbf{v}^s = \frac{\partial \mathbf{u}^s}{\partial t}$, and in the incompressible case additionally by the Lagrange multiplier p^s introduced due to the incompressibility of the material. The balance equations are

$$\rho^s \frac{\partial \mathbf{v}^s}{\partial t} + \rho^s (\nabla \mathbf{v}^s)\mathbf{v}^s = \operatorname{div}(\sigma^s) \qquad \text{in } \Omega_t^s.$$

The Cauchy stress tensor σ^s is specified by the constitutive laws which are derived and explained in Chapter 2 in section 2.5.2.

Interaction Condition

The boundary conditions on the fluid solid interface are assumed to be

$$\left.\begin{aligned} \sigma^f \mathbf{n} &= \sigma^s \mathbf{n} \\ \mathbf{v}^f &= \mathbf{v}^s \end{aligned}\right\} \qquad \text{on } \Gamma_t^0,$$

where $\mathbf{n}$ is a unit normal vector to the interface Γ_t^0.

Independent Material Parameters

To introduce the minimal set of independent parameters describing the materials we divide the momentum equations by the constant ρ^f and introduce the following parameters

$$\beta = \frac{\rho^s}{\rho^f}$$
$$\alpha = \frac{\mu}{\rho^f}$$

which together with the Poisson ratio ν_P and the kinematic viscosity ν of the fluid characterize the materials.

Domain Definition

The domain is based on the 2D version of the well-known *flow around cylinder* DFG benchmark [127] and showed here in Figure 5.1. By omitting the elastic bar behind the cylinder one can exactly recover the setup of the *flow around cylinder* configuration which allows for validation of the flow part by comparing the results with the older flow benchmark. The geometry parameters are given as follows (all values in meters):

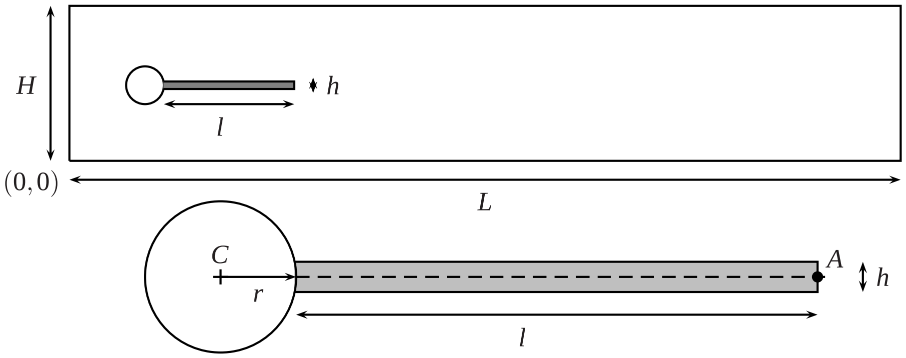

Figure 5.1: Computational domain and detail of the structure part

- The domain dimensions are: length $L = 2.5$, height $H = 0.41$.
- The circle center is positioned at $C = (0.2, 0.2)$ (measured from the left bottom corner of the channel) and the radius is $r = 0.05$.
- The elastic structure bar has length $l = 0.35$ and height $h = 0.02$, the right bottom corner is positioned at $(0.6, 0.19)$, and the left end is fully attached to the fixed cylinder.
- The control point is $A(t)$, attached to the structure and moving in time with $A(0) = (0.6, 0.2)$.

The setting is intentionally non-symmetric (see [127]) to prevent the dependence of the onset of any possible oscillation on the precision of the computation.

Boundary Conditions

The following boundary conditions are prescribed:

- Parabolic velocity profile is prescribed in the left channel inflow

$$v^f(0,y) = 1.5\bar{U}\frac{y(H-y)}{\left(\frac{H}{2}\right)^2} = 1.5\bar{U}\frac{4.0}{0.1681}y(0.41-y), \tag{5.1}$$

geometry parameters		value
channel length	L	2.5
channel width	H	0.41
cylinder center position	C	$(0.2, 0.2)$
cylinder radius	r	0.05
elastic structure length	l	0.35
elastic structure thickness	h	0.02
reference point	A	$(0.6, 0.2)$

Table 5.1: Overview of the geometry parameters.

such that the mean inflow velocity is $\bar{U}$ and the maximum of the inflow velocity profile is $1.5\bar{U}$.

- The outflow condition can be chosen by the user. For example *stress free* or *do nothing* conditions. The outflow condition effectively prescribes some reference value for the pressure variable p. While this value could be arbitrarily set in the incompressible case, in the case of compressible structure this will have influence on the stress and consequently the deformation of the solid. In this description, the reference pressure at the outflow is set to have *zero mean value*.
- The *no-slip* condition is prescribed for the fluid on the other boundary parts. i.e. top and bottom wall, circle and fluid-structure interface Γ_t^0.

Initial Conditions

- Zero velocity in the fluid and no deformation of the structure.
- Other suggested starting procedure is to compute the steady solution for the same problem with $\nu = 10^{-2}$ and structure being solid (i.e. $\mathbf{u}^s = 0$) and use such a solution as the initial solution. So the starting procedure for the non-steady tests is to use a smooth increase of the velocity profile in time as

$$v^f(t,0,y) = \begin{cases} v^f(0,y)\frac{1-\cos(\frac{\pi}{2}t)}{2} & \text{if } t < 2.0 \\ v^f(0,y) & \text{otherwise} \end{cases} \tag{5.2}$$

where $v^f(0,y)$ is the velocity profile given in (5.1).

5.1.2 Material parameters

An overview of certain material properties for some relevant fluids and elastic materials is shown in the Table 5.2. The choice of the parameters for the benchmark is guided by several requirements. First, we would like the flow to be in the laminar regime, which implies ”small” Reynolds numbers. On the other hand, the flow should be capable of deforming the elastic structure. A typical fluid candidate for such experiments is glycerine.

In order not to introduce additional numerical complications connected with high aspect ratios in the geometry, the deformable structure has a certain thickness which requires that the stiffness of the material should be low enough to allow significant

solid material	ρ^s $[\frac{\mathrm{kg}}{\mathrm{m}^3}]$	ν^s	E $[10^6 \frac{\mathrm{kg}}{\mathrm{ms}^2}]$	μ^s $[10^6 \frac{\mathrm{kg}}{\mathrm{ms}^2}]$
polybutadiene	910	0.50	1.6	0.53
polyurethane	1200	0.50	25	8.3
polypropylene	1100	0.42	900	317
PVC	1400	0.42	1500	528
steel	7800	0.29	210000	81400
cork	180	0.25	32	12.8

fluid material	ρ^f $[\frac{\mathrm{kg}}{\mathrm{m}^3}]$	ν^f $[10^{-6} \frac{\mathrm{m}^2}{\mathrm{s}}]$	μ^f $[10^{-3} \frac{\mathrm{kg}}{\mathrm{ms}}]$
air	1.23	0.015	0.018
aceton	790	0.405	0.32
ethyl alcohol	790	1.4	1.1
oil, vegetable	920	76.1	70
water	1000	1.14	1.14
blood	1035	3 – 4	3 – 4
glycerine	1260	1127	1420
honey	1420	7042	10000
mercury	13594	0.0114	1.55

Table 5.2: Overview of some solid and fluid material parameters (densities ρ^f, ρ^s, Poisson ratio ν^s, Young modulus E, shear modulus μ^s, dynamic viscosity μ^f and kinematic viscosity ν^f)

deformations. Certain rubber-like materials fit into such a setting, namely polybutadiene (for a future incompressible configuration) and polypropylene. In Table 5.3 the material parameters are presented for two combinations of glycerine and selected rubber-like material.

parameter	polybutadiene & glycerine	polypropylene & glycerine
ρ^s $[10^3 \frac{\mathrm{kg}}{\mathrm{m}^3}]$	0.91	1.1
ν^s	0.5	0.42
μ^s $[10^6 \frac{\mathrm{kg}}{\mathrm{ms}^2}]$	0.53	317
ρ^f $[10^3 \frac{\mathrm{kg}}{\mathrm{m}^3}]$	1.26	1.26
ν^f $[10^{-3} \frac{\mathrm{m}^2}{\mathrm{s}}]$	1.13	1.13

Table 5.3: Proposed material combination

Quantities for Comparison

Comparisons will be done for *fully developed flow*, and particularly for *one full period of the oscillation* with respect to the position of the point $A(t)$. The position of point $A(t)$ is time dependent. The quantities of interest are:

1. The displacements $u_1(t)$ and $u_2(t)$ in x- and y-direction of the point $A(t)$ at the end of the beam structure (see Figure 5.1) for one full period.

2. Forces exerted by the fluid on the *whole* submerged body, i.e. lift and drag forces

acting on the cylinder and the beam structure together

$$(F_D, F_L) = \int_S \sigma \mathbf{n} dS,$$

$$(F_D, F_L)^T = \int_S \sigma^{\mathbf{f}} \mathbf{n} dS = \int_{S_1} \sigma^{\mathbf{f}} \mathbf{n} dS + \int_{S_2} \sigma^{\mathbf{f}} \mathbf{n} dS,$$

where $S = S_1 \cup S_2$ (see Fig. 5.2) denotes the part of the circle being in contact with the fluid (i.e. S_1) plus part of the boundary of the beam structure being in contact with the fluid (i.e. S_2) and $\mathbf{n}$ is the outer unit normal vector to the integration path with respect to the fluid domain.

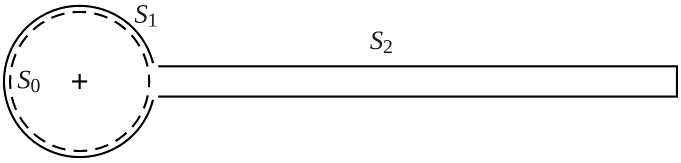

Figure 5.2: Integration path $S = S_1 \cup S_2$ for the force calculation.

Remark: The force can be calculated in several different ways, i.e.

$$\begin{aligned}(F_D, F_L) = \int_S \sigma \mathbf{n} dS &= \int_{S_1} \sigma^f \mathbf{n} dS + \int_{S_2} \sigma^f \mathbf{n} dS \\ &= \int_{S_1} \sigma^f \mathbf{n} dS + \int_{S_2} \sigma^s \mathbf{n} dS \\ &= \int_{S_1} \sigma^f \mathbf{n} dS + \int_{S_2} \frac{1}{2}(\sigma^s + \sigma^f) \mathbf{n} dS \\ &= \int_{S_0} \sigma \mathbf{n} dS\end{aligned}$$

The time dependent values are represented by the mean value, amplitude and frequency. The mean value and amplitude are computed from the last period of the oscillations by taking the maximum and minimum values, then the mean value is taken as average of the min/max values, and the amplitude is the difference of the max/min from the mean:

$$\begin{aligned}\text{mean} &= \frac{1}{2}(\max + \min) \\ \text{amplitude} &= \frac{1}{2}(\max - \min)\end{aligned}$$

The frequency of the oscillations can be computed either from the period time T as

$$\text{frequency} = \frac{1}{T}$$

or by using fourier analysis on the periodic data and taking the lowest significant frequency present in the spectrum. Additionally, a plot of the quantities over the period are presented.

All quantities are time dependent and are compared for *one* full period. For the validation of the employed fluid and solid solvers, we performed computations for 3 different

parameter	FSI1	FSI2	FSI3
ρ^s $[10^3 \frac{\mathrm{kg}}{\mathrm{m}^3}]$	1	10	1
ν^s	0.4	0.4	0.4
μ^s $[10^6 \frac{\mathrm{kg}}{\mathrm{ms}^2}]$	0.5	0.5	2.0
ρ^f $[10^3 \frac{\mathrm{kg}}{\mathrm{m}^3}]$	1	1	1
ν^f $[10^{-3} \frac{\mathrm{m}^2}{\mathrm{s}}]$	1	1	1
$\bar{U}$ $[\frac{\mathrm{m}}{\mathrm{s}}]$	0.2	1	2

parameter	FSI1	FSI2	FSI3
$\beta = \frac{\rho^s}{\rho^f}$	1	10	1
ν^s	0.4	0.4	0.4
$\mathrm{Ae} = \frac{E^s}{\rho^f \bar{U}^2}$	3.5×10^4	1.4×10^3	1.4×10^3
$\mathrm{Re} = \frac{\bar{U}d}{\nu^f}$	20	100	200
$\bar{U}$	0.2	1	2

Table 5.4: Parameter settings for the FSI benchmarks.

levels of spatial discretization Δx (see Fig. and Table 5.3) and 3 time step sizes Δt. The example calculations presented in figures 5.4 – 5.5 are computed with the second order time discretization by the Crank-Nicholson scheme and with space discretization by the finite element method with $Q_2/Q_2/P_1^{dis}$ approximation (see [123]). The computational mesh is obtained by 2 regular refinements of the example mesh in Figure 5.3 which is used for the computations. All simulations have been performed with a fully implicit monolithic ALE-FEM method with a fully coupled multigrid solver as described in [75].

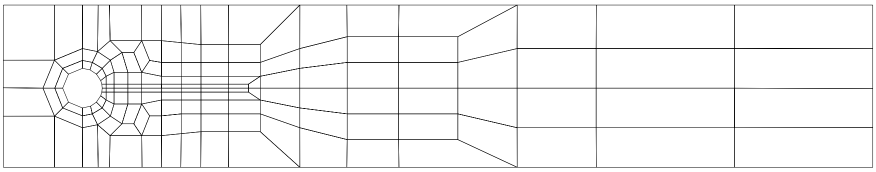

level	#el	#dof
0	62	1338
1	248	5032
2	992	19488
3	3968	76672
4	15872	304128
5	63488	1211392
6	253952	4835328
7	1015808	19320832

Figure 5.3: Coarse mesh with number of degrees of freedom for refined levels.

5.1.3 Numerical Results

The results of the benchmark computations are summarized in Tables 5.5 and figures and tables 5.4–5.5 (ignoring units). Here, $u_1(A)$ and $u_2(A)$ denote the displacements in x- and y-direction of the point A and the drag and lift forces by F_D and F_L respectively. For the unsteady case also the frequencies f_1 and f_2 obtained for the displacements $u_1(A)$ and $u_2(A)$, respectively, are given. The column ”Unknowns” refers to the total number (in space), i.e., the sum of unknowns for all velocity components, pressure, and displacement components.

The following FSI tests are performed for three different inflow speeds. FSI1 is resulting in a steady state solution, while FSI2 and FSI3 result in periodic solutions. The parameter values for the FSI1, FSI2 and FSI3 are given in the Table 5.4. Here, the computed values are summarized in Table 5.5 for the steady state test FSI1.

level	nel	ndof	$u_1(A)[\times 10^{-3}]$	$u_2(A)[\times 10^{-3}]$	drag	lift
2	992	19488	0.02287080	0.8193038	14.27359	0.7617550
3	3968	76672	0.02277423	0.8204231	14.29177	0.7630484
4	15872	304128	0.02273175	0.8207084	14.29484	0.7635608
5	63488	1211392	0.02271553	0.8208126	14.29486	0.7636992
6	253952	4835328	0.02270838	0.8208548	14.29451	0.7637359
7	1015808	19320832	0.02270493	0.8208773	14.29426	0.7637460
ref.			0.0227	0.8209	14.294	0.7637

Table 5.5: Results for **FSI1**

In Figure 5.4 and 5.5, resulting plots of x-y displacement of the trailing edge point A of the elastic bar and plots of the forces (lift, drag) acting on the cylinder attached with an elastic bar are drawn and computed values for three different mesh refinement levels and two different time steps for the non-steady tests FSI2 and FSI3 are presented respectively, which show the (almost) grid independent solution behavior (for more details see [123]).

Comparative benchmark results for different solution methods for fluid-structure interaction problems are reported in [125] which have been developed as collaborative project under the DFG Research Unit 493.

As said before, the benchmark configurations have been carefully chosen and validated via extensive numerical tests in which various CFD codes for main result, characteristic flow quantities provided which allow a quantitative validation and comparison of different numerical methods and software tools (see [125] for details).

As a first result for the FSI1 benchmark, which leads to stationary displacement of the attached elastic beam, it is seen that all applied methods and codes can approximate the same results, at least with decreasing mesh width [125].

Evidently for FSI3, the evaluation of the results is a little bit more difficult: First of all, all schemes show the tendency to converge towards the (more or less) same solution values, at least for increasing mesh level. Although the applied FSI techniques are very different w.r.t. discretization, solver and coupling mechanisms, it is found that the FSI3 benchmark setting proves to be a very valuable tool for numerical FSI benchmarking, leading to grid independent results for the prescribed geometrical and parameter settings [125].

Moreover, also clear differences between the different approaches with regard to accuracy are visible. Particularly for the drag and lift values and also for the displacement values [125]. A more detailed evaluation and also more rigorous comparisons w.r.t. the ratio ‘accuracy vs. efficiency’ are therefore planned for the future. The contribution based on this benchmark setting are made [123, 125, 111].

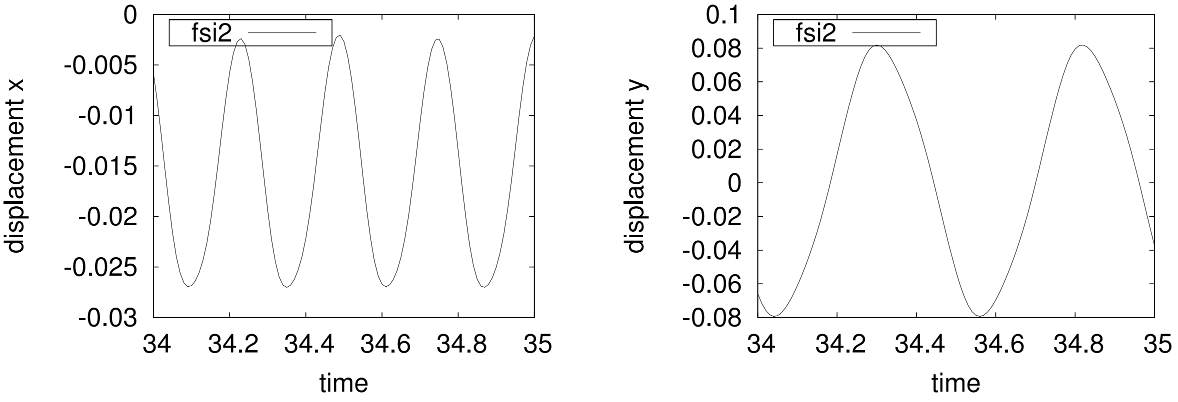

FSI2: x & y displacement of the point *A*

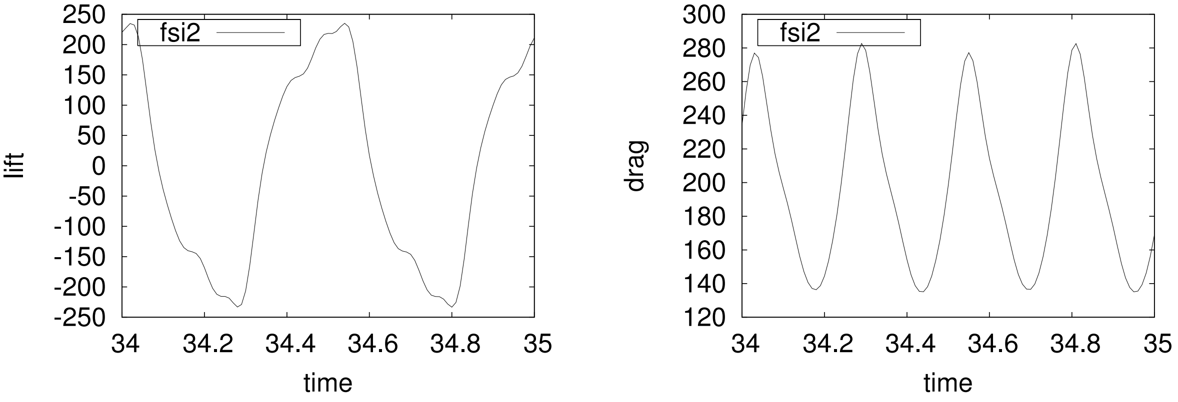

FSI2: lift and drag force on the cylinder+elastic bar

lev.	Unknowns	$u_1(A)[\times 10^{-3}]$	$u_2(A)[\times 10^{-3}]$	F_D	F_L	f_1	f_2
2	19488	-14.02 ± 12.03	1.25 ± 79.3	210.10 ± 72.62	0.25 ± 227.9	3.85	1.93
3	76672	-14.54 ± 12.50	1.25 ± 80.7	212.83 ± 75.89	0.92 ± 234.3	3.86	1.93
4	304128	-14.88 ± 12.75	1.24 ± 81.7	215.06 ± 77.76	0.82 ± 237.1	3.86	1.93
2	19488	-14.01 ± 12.04	1.25 ± 79.3	210.09 ± 72.82	0.52 ± 228.6	3.86	1.93
3	76672	-14.54 ± 12.48	1.25 ± 80.7	213.06 ± 75.76	0.85 ± 234.4	3.86	1.93
4	304128	-14.87 ± 12.73	1.24 ± 81.7	215.18 ± 77.78	0.87 ± 238.0	3.86	1.93
2	19488	-14.01 ± 12.04	1.28 ± 79.2	210.14 ± 72.86	0.49 ± 228.7	3.86	1.93
3	76672	-14.48 ± 12.45	1.24 ± 80.7	213.05 ± 75.74	0.84 ± 234.8	3.86	1.93
4	304128	-14.85 ± 12.70	1.30 ± 81.6	215.06 ± 77.65	0.61 ± 237.8	3.86	1.93
ref.		-14.85 ± 12.70	1.30 ± 81.7	215.06 ± 77.65	0.61 ± 237.8	3.86	1.93

Figure 5.4: Results for **FSI2** with time step $\Delta t = 0.002, \Delta t = 0.001, \Delta t = 0.0005$.

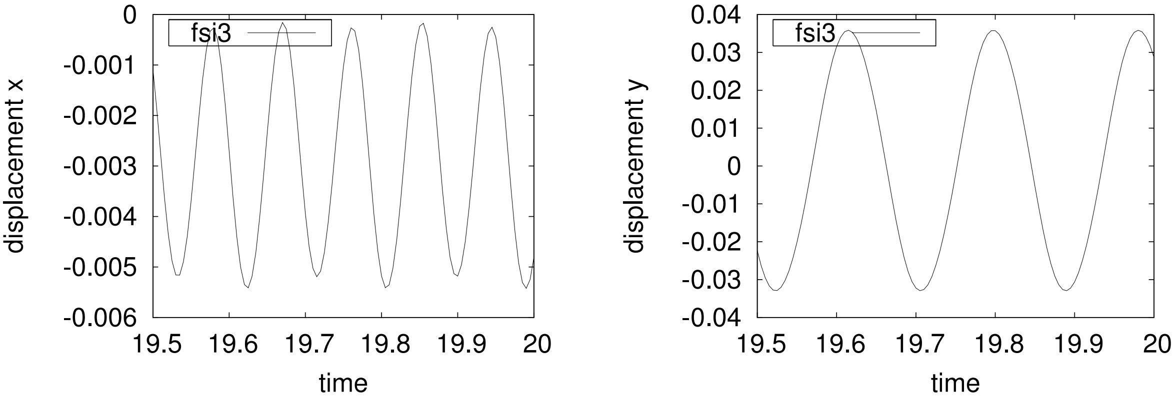

FSI3: x & y displacement of the point A

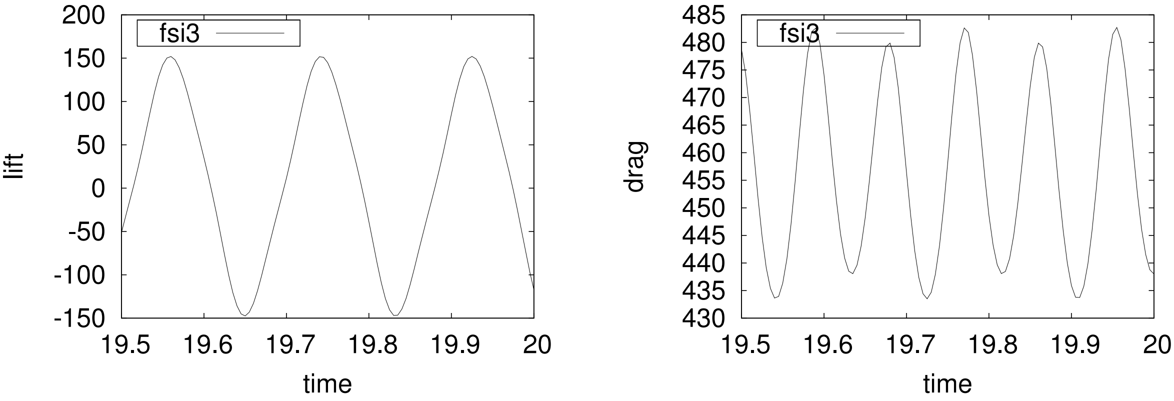

FSI3: lift and drag force on the cylinder+elastic bar

lev.	Unknowns	$u_1(A)[\times 10^{-3}]$	$u_2(A)[\times 10^{-3}]$	F_D	F_L	f_1	f_2
2	19488	-3.02 ± 2.83	1.41 ± 35.47	458.2 ± 28.32	2.41 ± 145.58	10.75	5.37
3	76672	-2.78 ± 2.62	1.44 ± 34.36	459.1 ± 26.63	2.41 ± 151.26	10.93	5.46
4	304128	-2.86 ± 2.70	1.45 ± 34.93	460.2 ± 27.65	2.47 ± 154.87	10.95	5.47
2	19488	-3.02 ± 2.85	1.42 ± 35.63	458.7 ± 28.78	2.23 ± 146.02	10.75	5.37
3	76672	-2.78 ± 2.62	1.44 ± 34.35	459.1 ± 26.62	2.39 ± 150.68	10.92	5.46
4	304128	-2.86 ± 2.70	1.45 ± 34.90	460.2 ± 27.47	2.37 ± 153.75	10.92	5.46
2	19488	-3.02 ± 2.85	1.32 ± 35.73	458.7 ± 28.80	2.23 ± 146.00	10.74	5.36
3	76672	-2.77 ± 2.61	1.43 ± 34.43	459.1 ± 26.50	2.36 ± 149.91	10.93	5.46
4	304128	-2.88 ± 2.72	1.47 ± 34.99	460.5 ± 27.74	2.50 ± 153.91	10.93	5.46
ref.		-2.88 ± 2.72	1.47 ± 34.99	460.5 ± 27.74	2.50 ± 153.91	10.93	5.46

Figure 5.5: Results for **FSI3** with time step $\Delta t = 0.001, \Delta t = 0.0005, \Delta t = 0.00025$.

5.2 Experimental Benchmark

Experimental reference test case [57] were proposed and conducted at the Institute of Fluid Mechanics at University of Erlangen-Nürnberg [56]. The definition of the experimental benchmark is introduced in the subsequent sections followed by the numerical results.

5.2.1 Introduction

The definition of the proposed test case in [56, 57, 58] took into account four principal aspects: (i) reproducibility of the resulting motion, (ii) two-dimensionality of the structure deflection, (iii) moderate structure motion frequency and (iv) significant excursion of the structure.

The main objective of the following numerical investigation is to analyze and to validate our monolithic approach for a configuration with a point constraint (”rigid solid with rotational degree of freedom”) for a special experimental set up. In the future, these numerical and experimental studies shall lead to a reliable data basis for the validation and comparison purposes of different numerical methods and code implementations for fluid-structure interaction simulations. These numerical studies are focused on the two-dimensional periodical swiveling motion of a simple flexible structure driven by a prescribed inflow velocity (see [56]). The structure has a linear mechanical behavior and the fluid is considered incompressible and in the laminar regime. The cylinder is fixed only at the center and can rotate freely. To allow for this kind of additional rotational movement in our method, the cylinder has to be included in the mesh in our recent approach. By prescribing zero displacement for the node located in the center of the cylinder we eliminate the translational degree of freedom of the whole structure but preserve the rotational freedom of the cylinder. Hence, the position of all other nodes located inside the cylinder are taken into account as part of the solution. We divided the numerical tests into two parts corresponding to the thickness of the elastic beam i.e for $1mm$ thick beam and for $0.04mm$ thick beam attached to an aluminum cylinder. At the trailing edge of the elastic beam a rectangular stainless steel mass is located. Both the rear mass and the cylinder are considered rigid. All the structure is free to rotate around an axis located in the center point of the cylinder.

Structure Properties

The structure consists of a thin elastic beam attached to the cylinder, which is identified by the center of the cylinder with one grid point. This point constraint effectively fixes the position of the cylinder axis, but still allows the free rotation around this point. At the trailing end of the beam a rear mass is attached. Such a problem is encountered in many real life applications of great importance. Typical examples of this type of problem are the areas of biomedical fluids which include joint lubrication and deformable cartilage and blood flow interaction with implants. The detailed dimensions of the structure are presented in Fig. 5.6. The densities of the different materials used in the construction of the model are given in Table 5.2.1. The shear modulus of stainless steel is $7.58 \times 10^7 kg/mms^2$ and Poisson ratio of the beam ν^p is taken as 0.3. The Young modulus is measured to be $2 \times 10^8 kg/mm^2$.

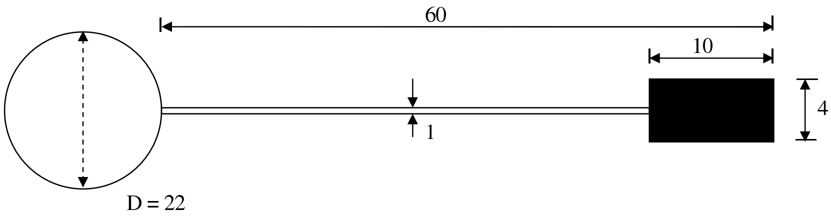

Figure 5.6: Structure (dimensions in millimeters)

variable	material	value
$\rho_{cylinder}$	(aluminum)	$2.828 \times 10^{-6} kg/mm^3$
ρ_{beam}	(stainless steel)	$7.855 \times 10^{-6} kg/mm^3$
$\rho_{rearmass}$	(stainless steel)	$7.800 \times 10^{-6} kg/mm^3$

Table 5.6: Density values of the structure components

Fluid Properties

As fluid for the tests, an incompressible fluid Polyethylene glycol syrup is chosen because of its high viscosity and a density close to water. It has a kinematic viscosity $164 mm^2/s$ and the density of the fluid is $1.05 \times 10^{-6} kg/mm^3$.

Geometry of the Problem

The geometry of the physical domain coincides with the shape of the facility test function. The co-ordinate system used is centered in the rotating axis of the flexible structure front body. The x-axis is aligned with the incoming flow. Then, the geometric details are as follows:

- The overall dimensions of the physical domain are length $L = 338mm$ and width $W = 240mm$.

- The center of the cylindrical front body is C which is located 55mm downstream of the beginning of the physical domain, and the radius r of the cylinder is 11mm.

- The dimensions of the flow field measuring domain (hatched line) are given by length $L' = 272mm$ and width $W' = 170mm$. The measuring domain begins $19mm$ after the beginning of the physical domain as shown in Figure 5.7. The Reynolds number is defined by $Re = \frac{2r\bar{V}}{\nu^f}$ with mean velocity $\bar{\mathbf{V}} = \frac{2}{3}v(0, W/2, t)$ and W height of the channel (see Fig. 5.7).

- The gravity force $9810 mm/s^2$ is aligned with the x-axis.

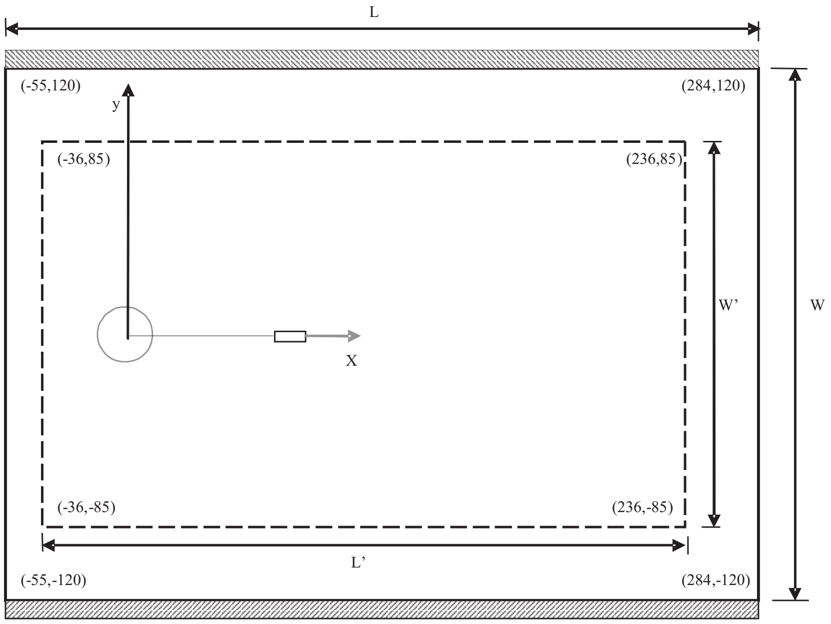

Figure 5.7: Physical domain (continuous line) and flow field measuring domain (hatched line)

Boundary and Initial Conditions

The velocity profile prescribed at the left channel inflow is defined as approximation of the experimental inflow data

$$\mathbf{v}^f(0,y) = \bar{U}(1-(y/120)^8)(1+(y/120)^8), \tag{5.3}$$

such that the maximum of the inflow velocity profile is $\bar{U}$. Figure 5.8 shows the

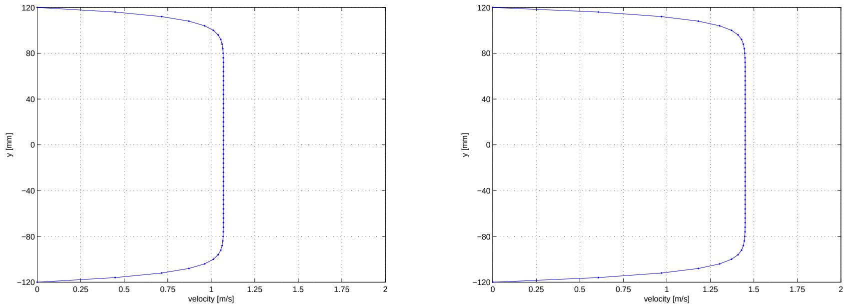

Figure 5.8: Inlet velocity profiles for the first (left) and second (right) laminar reference test case.

inlet velocity profiles for laminar case 1 and case 2. The outflow condition effectively prescribes some reference value for the pressure variable p. While this value could be arbitrarily set in the incompressible case, in the case of a compressible structure this will have influence onto the stress and consequently the deformation of the solid. The *no-slip* condition is prescribed for the fluid on the other boundary parts, i.e. top and bottom wall, circle and fluid-structure interface Γ_t^0. Suggested starting procedure for the non-steady tests is to use a smooth increase of the velocity profile in time as

$$\mathbf{v}^f(t,0,y) = \begin{cases} \mathbf{v}^f(0,y)\dfrac{1-cos(\pi t/2)}{2} & \text{if} \quad t<1 \\ \mathbf{v}^f(0,y) & \text{otherwise} \end{cases} \tag{5.4}$$

where $\mathbf{v}^f(0,y)$ is the velocity profile given in (5.3). Since the cylinder is allowed to freely rotate around its axis, we need to incorporate this into our setup. As described before, by identifying the center of the cylinder with one grid point of our mesh we can prescribe a Dirichlet type boundary condition for the velocity and the displacement of the structure at this point. This point constraint effectively fixes the position of the cylinder axis, but still allows the free rotation around this point.

We perform numerical comparisons for different time stepping schemes, including variants of the Fractional-Step-scheme (FS), Backward Euler (BE) and Crank- Nicholson scheme (CN) for both solid and fluid parts which have been derived in Chapter 3.

5.2.2 Numerical Investigations

In this section we will present numerical results for the $1mm$ thick beam and for the actual thickness $0.04mm$ (see [56])of the beam in similar order.

Results for $1mm$ Thick Beam In the first numerical test we set the thickness of the beam $1mm$ (see Fig. 5.6) and also we reduce the rigidity of the beam (i.e., shear modulus) from $7.69\times10^7 kg/mms^2$ to $7.69\times10^4 kg/mms^2$, all other parameters are from table 5.2.1. We applied the presented time stepping schemes, namely (BE, CN, FS, GL) prescribed in Chapter 3 to analyze the behavior for different Δt. For $\Delta t = 0.0005$ almost the identical amplitude of oscillations (≈ 13.84) of rear mass is observed (see figure 5.11) for the higher order schemes (CN, FS, GL) and for the 1st order Backward Euler (BE) the amplitude of oscillations (≈ 12.42) of rear mass shows 10 percent less accuracy compared to CN, FS and GL. For $\Delta t = 0.00005$ Backward Euler (BE) shows better agreement of the amplitude of oscillations (≈ 13.71) of the rear mass to CN, FS, GL. For larger time step, GL is more damped than CN and FS. We use two different meshes (see Fig. 5.9 and 5.10) and also we increase the mesh refinement level from level 1 to level 2. Corresponding plots for two different meshes and different mesh refinement levels are given in figure 5.12 and figure 5.13 which shows that our solution is almost independent of mesh type and mesh refinement levels. From experimental results, for velocity $1130mm/s$ the structure shows hysteric behavior, but in our simulations no hysteric behavior could be observed so for and resulting frequency of oscillations is $\approx 10Hz$ for applying all the four time stepping schemes mentioned above. The displacement path of the rear mass is shown in figures 5.14 and 5.15.

The following observations are made and corresponding numerical results were obtained:

1. The experimental thickness of the beam is taken as $0.04mm$ and we have taken the thickness of the beam as 1mm for simplicity.
2. When we increase the velocity, the frequency of oscillations increases linearly with the velocity.
3. The frequency of oscillations for the beam with thickness 0.04 mm with velocity $1070mm/s$ is $6.38Hz$, while with the thickness 1mm and velocity 1130 mm/s, the frequency of oscillations of the rear mass is approx. $10Hz$.

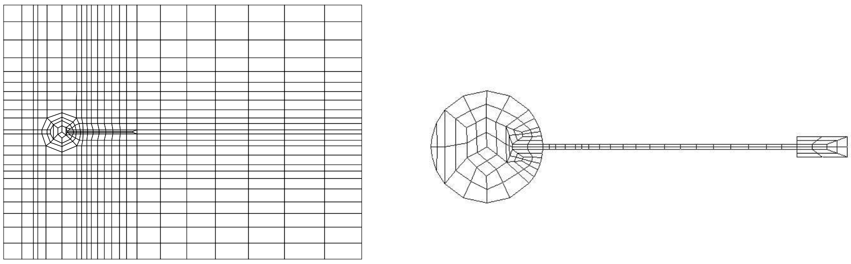

Figure 5.9: Coarse mesh 1 with 576 elements, 622 nodes and 11308 dof.

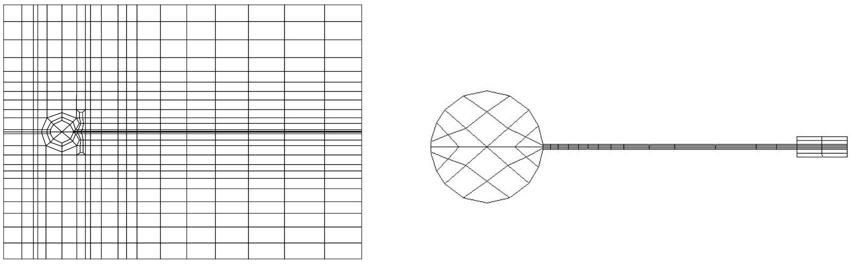

Figure 5.10: Coarse mesh 2 with 529 elements, 574 nodes and 10407 dof.

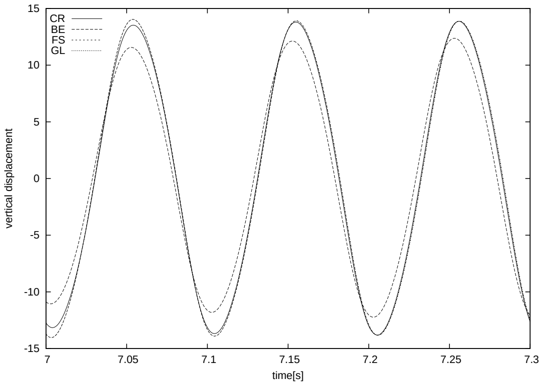

Figure 5.11: For $\Delta t = 0.0005$, the amplitude of oscillations of rear mass is almost identical for the different time stepping schemes CN, FS, GL.

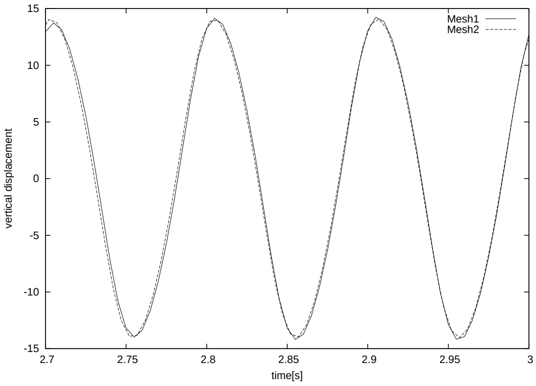

Figure 5.12: For the two different meshes, the amplitude of oscillations is almost the same for the Fractional-Step-θ-scheme.

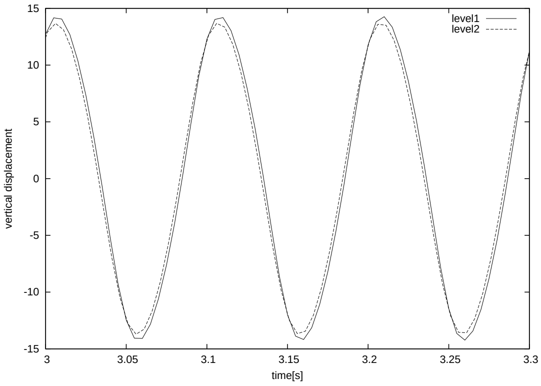

Figure 5.13: For refinement level 1 and 2 the amplitude of oscillation is almost identical.

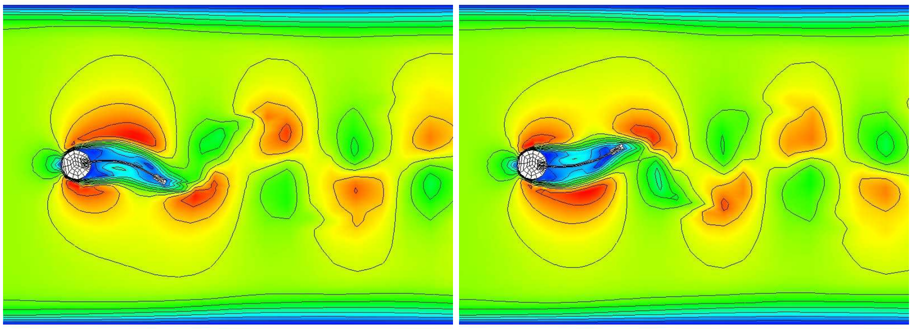

Figure 5.14: Snapshots of the vertical displacement of the rear mass with frequency of oscillations $\approx 10Hz$ for $1mm$ thick beam.

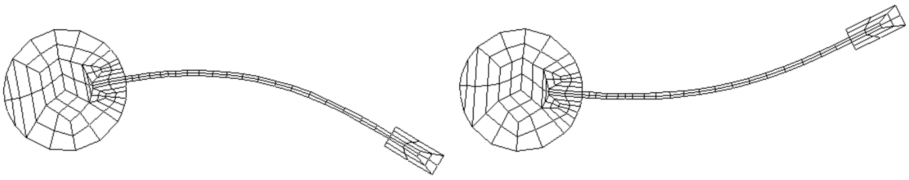

Figure 5.15: Zoomed snapshots of the deformed $1mm$ thick beam.

For velocity $600mm/s$ and $800mm/s$ with $0.04mm$ Thick Beam In this test we keep the thickness of the beam $0.04mm$ as described in the experimental set up [58]. The minimum velocity needed to excite the movement of the structure slightly varied from test to test. In our case for velocity $600mm/s$ ($Re \approx 80$) we are able to excite the structure. For $\Delta t = 0.0025$, path of the rear mass is shown in figure 5.16 for the Backward Euler (BE) and Fractional-step-θ schemes and the difference in the amplitude of oscillations of rear mass is plotted in figure 5.16. Frequency of the structure movement increases linearly with the increase of the velocity of the fluid. We used the velocity $600mm/s$ ($Re \approx 80$) at beginning, then switching to $800mm/s$ ($Re \approx 107$) for simplicity, see figure 5.17 and 5.18.

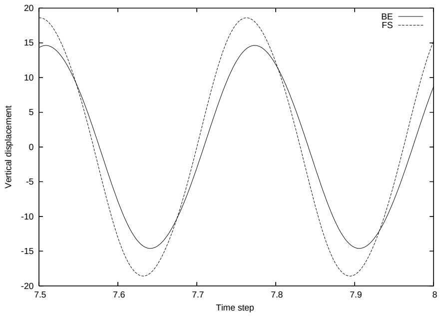

Figure 5.16: For $\Delta t = 0.0025$, the amplitude of oscillations of rear mass for the different time stepping schemes BE, FS for velocity $600mm/s$.

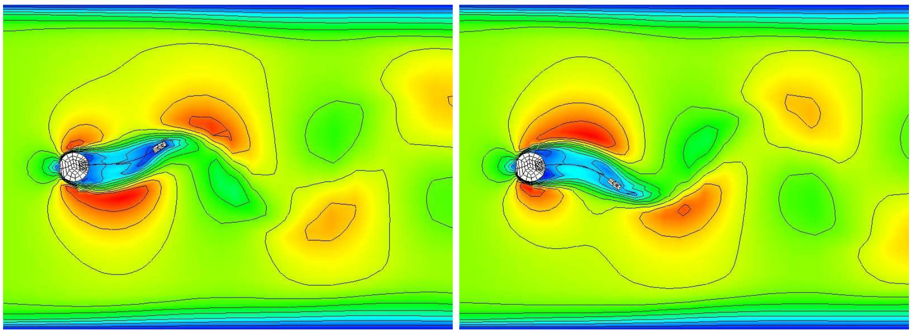

Figure 5.17: Snapshots of the vertical displacement of the rear mass with maximum amplitude ≈ 17.0 and frequency $\approx 4.5Hz$ and velocity $800mm/s$.

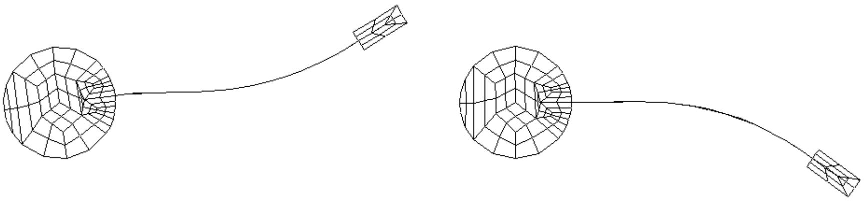

Figure 5.18: Zoomed snapshots of the deformed beam for velocity $800mm/s$.

5.2.3 Comparison of Experimental and Numerical Results

Experimental Results Experimental studies on reference test cases were conducted in laminar flows ($Re \leq 200$) at the Institute of Fluid Mechanics at University of Erlangen-Nürnberg [56]. The structure was defined to be constituted by a $0.04mm$ thick stainless steel sheet attached to an $22mm$ diameter aluminum cylindrical front body. At the trailing edge of the beam a $10mm \times 4mm$ rectangular stainless steel mass was located. All the structure was free to rotate around an axis located in the center point of the front cylinder. Both the front cylinder and the rear mass were considered rigid. The structure model was tested in a viscous liquid flow at different velocities up to $2000mm/s$. The minimum velocity needed for the movement of the structure slightly varied from test to test. In most of the cases it was already possible to achieve a consistent swiveling motion for velocities slightly smaller than $1000mm/s$. The frequency of the structure movement increased linearly with the velocity of the approaching fluid. For velocity ranging from $1140mm/s$ to $1300mm/s$, the frequency of oscillations showed a pronounced hysteresis depending on increasing versus decreasing flow velocity. There were two test cases performed using different flow velocity and the corresponding results were as follows: Using velocity $1070mm/s$ ($Re \approx 140$) one measures a frequency of oscillations of the structure $\approx 6.38Hz$, and with velocity $1450mm/s$ ($Re \approx 190$) a frequency of oscillations of the structure $\approx 13.58Hz$ is observed [58]. At higher velocities the motion of the structure became faster and more complex. At around $1300mm/s$ the structure shifted abruptly to a new swiveling mode in which the second deflection mode played an important role [56, 57, 58]. Figure 5.19 shows the comparison between experimental versus numerical results of the problem.

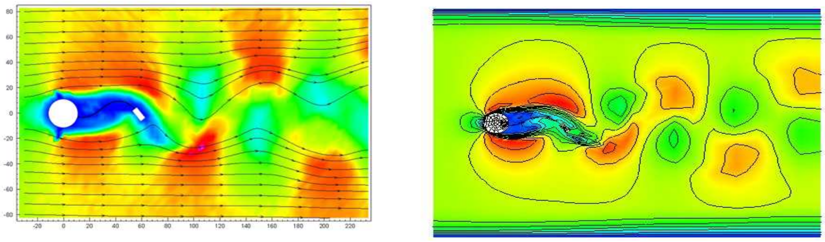

laminar cases	experiment 1: $Re = 140$	experiment 2: $Re = 190$
measured frequency[Hz]	6.38	13.58
computed frequency[Hz]	6.42	10.90
computed frequency[Hz] [1]	7.47	16.78
computed frequency[Hz] [8]	6.72	14.42

Figure 5.19: Experiment from Erlangen (left) and numerical result for velocity $1450mm/s$ (right). Table shows the computed frequencies of oscillation versus experiment.

Laminar case 1: velocity $1070mm/s$ Figure 5.20 shows the amplitude of oscillations of rear mass attached to the elastic beam for velocity $1070mm/s$ and the frequency of oscillation observed is $\approx 6.42Hz$. Figure 5.21 shows the deformed shape of the beam for velocity $1070mm/s$ and figure 5.22 shows the complete mesh behavior during simulation. The experimentally determined swiveling frequency in [58] is

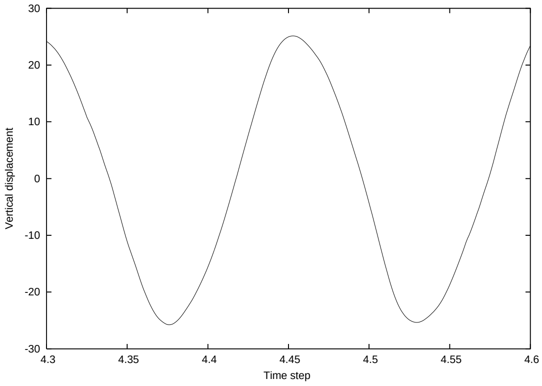

Figure 5.20: Frequency of oscillations of the rear mass for velocity $1070mm/s$ for the described numerical set up is $\approx 6.42Hz$.

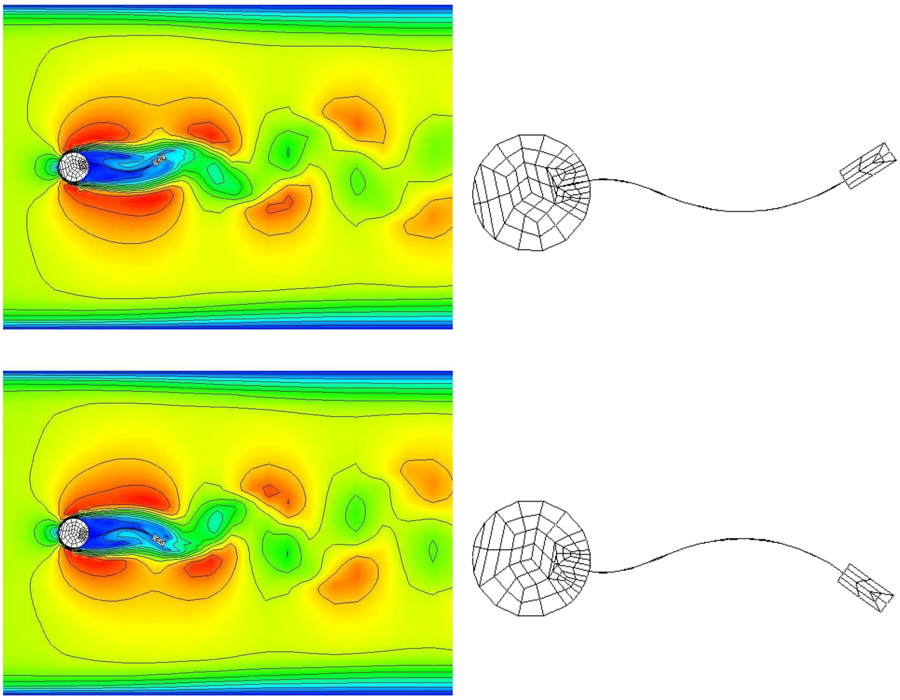

Figure 5.21: Left: Snapshots of the vertical displacement of the rear mass for velocity $1070mm/s$. Right: Zoomed snapshots of the structure.

$6.38Hz$ while in case of numerical simulation it is yielded $6.72Hz$ [116], $7.47Hz$ [52] and our finding is $6.42Hz$. Here, numerical value is bit high but still in fairly good

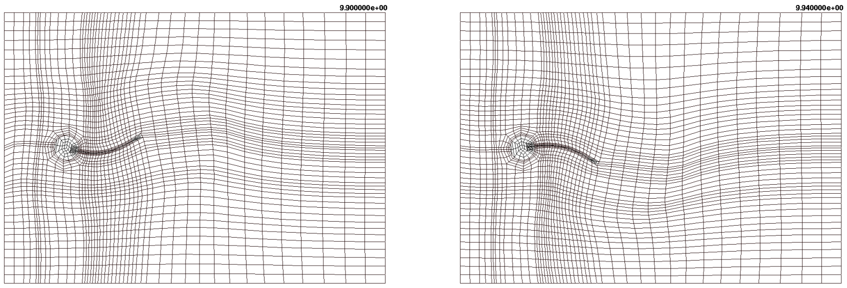

Figure 5.22: Snapshot of the complete mesh.

agreement to [58]. A front cylinder angle for one swiveling period is given in Figure 5.23. A front cylinder body angle from the calculations of [116] and [52] are shown in comparison of experiment [58] left of the figure 5.23 and our numerical result is plotted to the right of the figure. Here, the absolute values compared to the experiment differed noticeably. Here again, the computed results are smaller than the measured ones. The figure 5.24 shows the trailing edge xy-coordinates for one swiveling period.

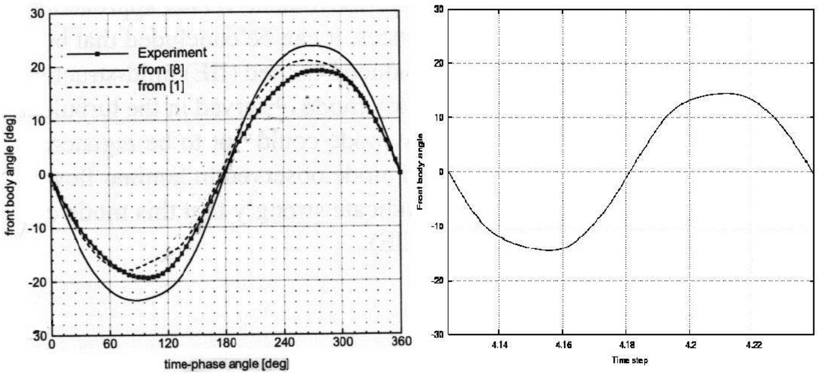

Figure 5.23: Comparison of front body angle for one period at $1070 mm/s$.

Here, numerical results are lesser than the measure one. For comparing the flow field two monitor points are chosen. The first point (point 1) is located at the coordinate $(82mm, 0mm)$ and the second point (point 2) at the coordinate $(82mm, 40mm)$. Numerical velocity out put data is available only in [116] and the u-, and v-components are plotted together with the experiment data [58] in figure 5.25 and in figure 5.26 for these two monitor points respectively. The numerical and experiment result comparable for the second monitor point and for the point 1 prediction is quite hard [58]. For these monitor points numerical results are also reported in [116]. Numerical results and experiment results matched very well at the second monitor point.

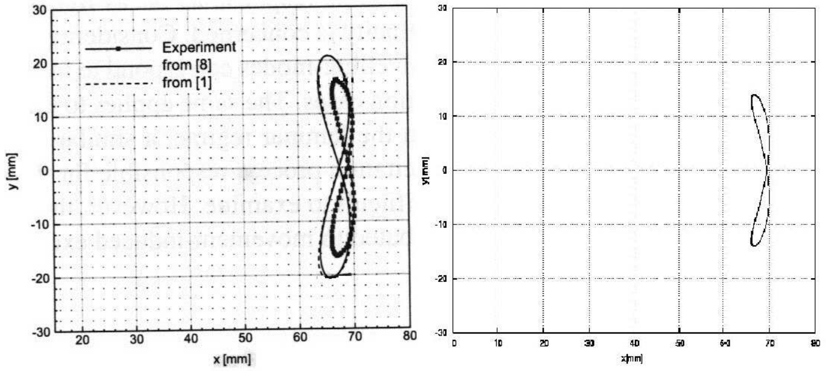

Figure 5.24: Comparison of the x-y trailing edge coordinates for one period at 1070mm/s.

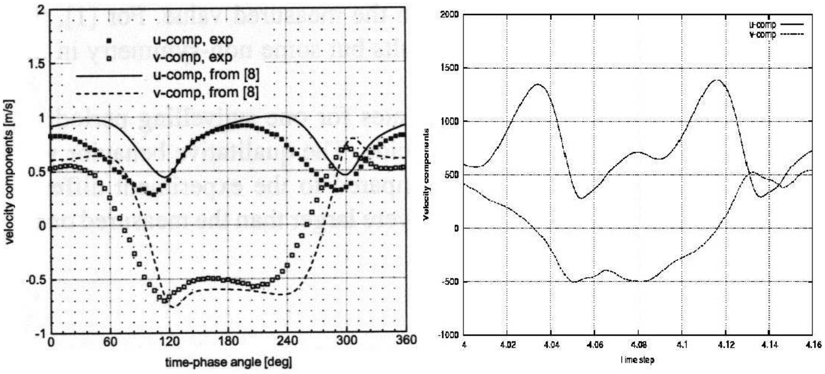

Figure 5.25: Comparison of the flow velocity at point 1 for one period at 1070mm/s.

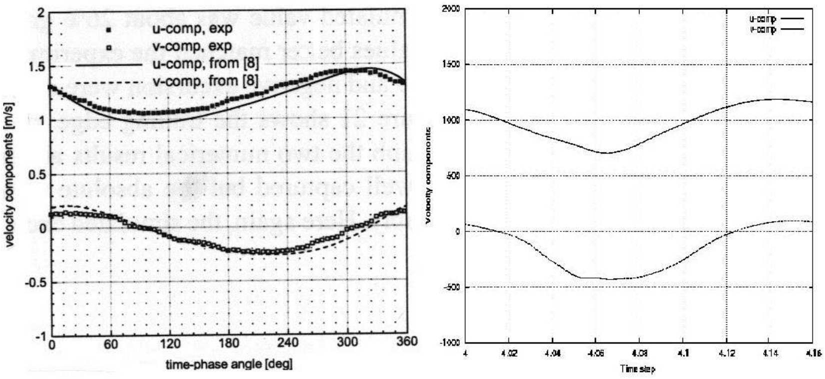

Figure 5.26: Comparison of the flow velocity at point 2 for one period at 1070mm/s.

Laminar case 2: Velocity $1450mm/s$ The experimentally determined swiveling frequency is $13.58Hz$ while in case of numerical simulation it is $\approx 10.9Hz$ and also the simulations resulted in values of 14.42 [116] and 16.78 [52], see figure 5.27. For the velocity $1450mm/s$ the deformation of the elastic beam and rear mass is even more significant, see figure 5.28.

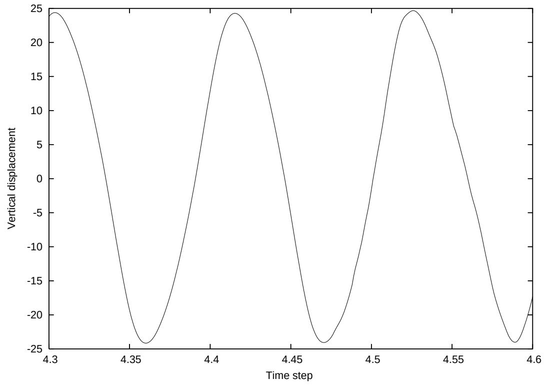

Figure 5.27: Frequency of oscillations of the rear mass for velocity $1450mm/s$ for the described numerical set up is $\approx 10.9Hz$.

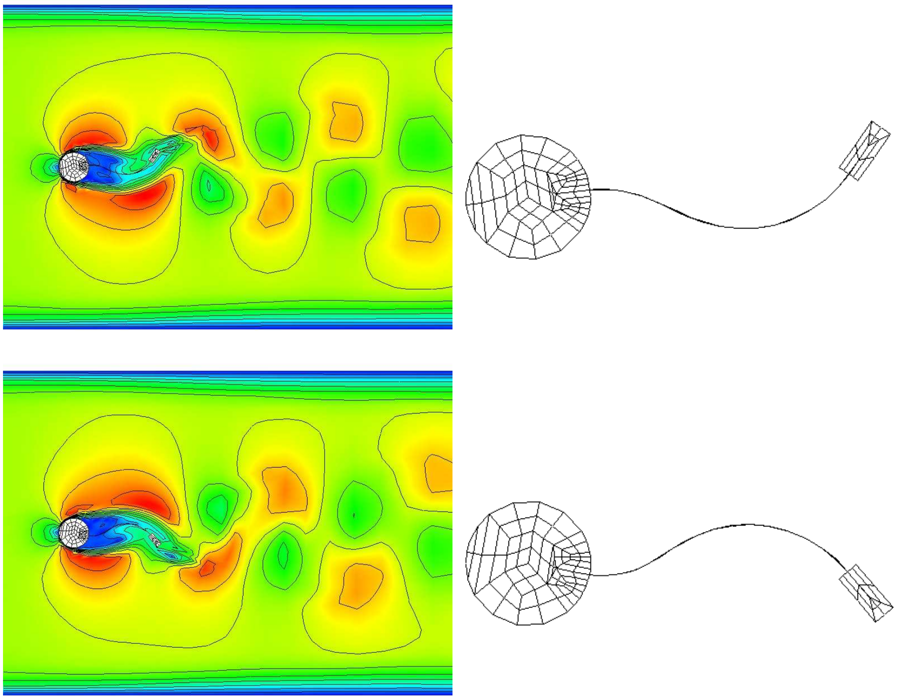

Figure 5.28: Left: Snapshots of the vertical displacement of the rear mass for velocity $1450mm/s$. Right: Zoomed snapshots of the structure.

In figure 5.29 front body angle is plotted and difference in dynamic response of the structure is shown for two swiveling modes with comparison to experiment [58]. A comparison between figure 5.23 (left) and figure 5.29 (left) shows the response of structure for the two swiveling modes and experiment finding in [58].

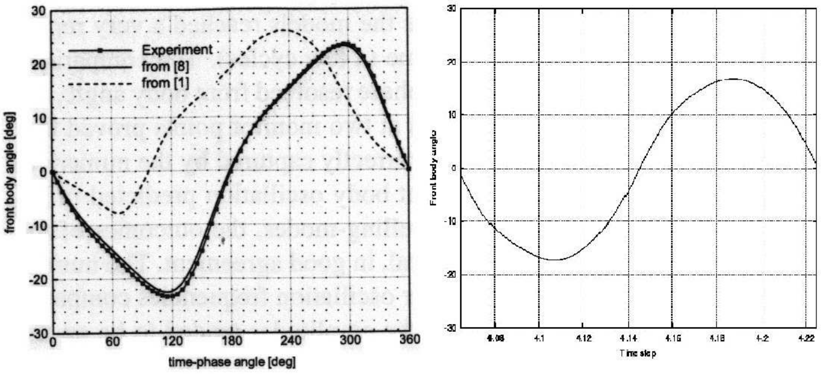

Figure 5.29: Comparison of front body angle for one period at 1450mm/s.

The figure 5.30 displays the path of trailing edge for one swiveling period at 1450mm/s. Here, numerically calculated results (right) are greater than the measure one (left) [58, 52, 116]. Numerically calculated velocity out put for the u-, and v-components for the first monitor point 1 are plotted in Figure 5.31 in comparison of experiment as well as other computed findings [58, 116] (left). For the first monitor point agreement is good enough although slightly less value for the v-component as compare to experiment finding in [58]. In figure 5.32 the u-, and v-components are plotted for the the second monitor point. The second monitor point is comparable to [58]. Numerical velocity out put data for monitor points is available only in [116] and our numerical calculations.

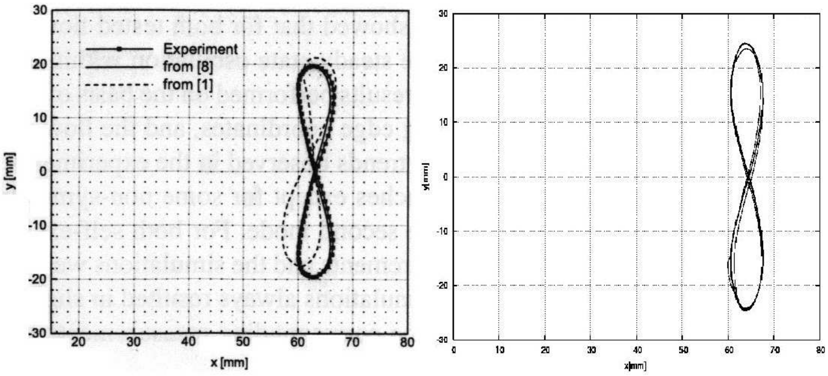

Figure 5.30: Comparison of x-y trailing edge coordinates for one period at 1450mm/s.

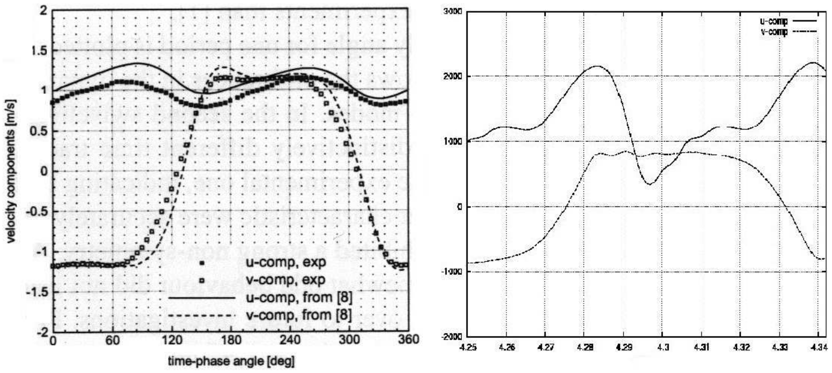

Figure 5.31: Comparison of the flow velocity at point 1 for one period at 1450mm/s.

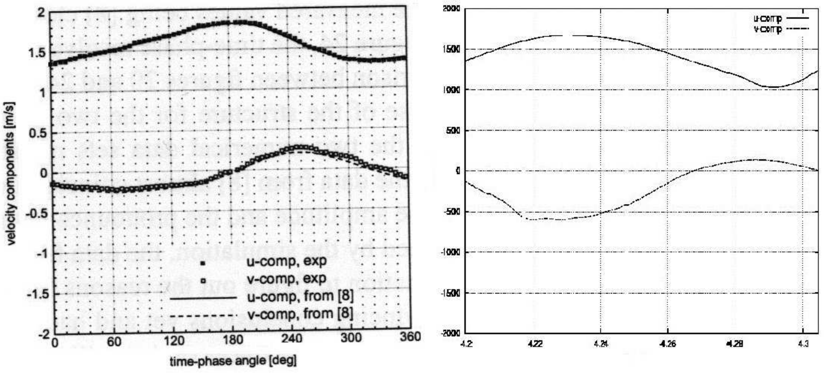

Figure 5.32: Comparison of the flow velocity at point 2 for one period at 1450mm/s.

5.3 Biomedical Applications: Aneurysm

In the following, we consider the numerical simulation of special problems encountered in the area of cardiovascular hemodynamics, namely flow interaction with thick-walled deformable material i.e Aneurysm hemodynamics. Aneurysms are of two kind, abdominal aneurysm (AA) and brain aneurysm (BA). The word ‘aneurysm’ comes from the Latin word *aneurysma* which means dilatation. Aneurysm is a local dilatation in the wall of a blood vessel, usually an artery, due to a defect, disease or injury. Typically, as the aneurysm enlarges, the arterial wall becomes thinner and eventually leaks or ruptures, causing sub-arachnoid hemorrhage (SAH) (bleeding into brain fluid) or formation of a blood clot within the brain. In the case of a vessel rupture, there is a hemorrhage, and when an artery ruptures, then the hemorrhage is more rapid and more intense. In arteries the wall thickness can be up to 30% of the diameter and its local thickening can lead to the creation of an aneurysm.

From a medical point of view, the use of stents provides an efficient treatment for managing the difficult entity of intra-cranial aneurysms. Here, the thickness of the aneurysm wall is attenuated and the aneurysm hemodynamics changes significantly.

Since the purpose of this device is to control the flux within the aneurysm in order to occlude it by a clot or rupture, the resulting flow behavior into and within the aneurysm is the main objective, particularly in view of the different stent geometries. Therefore, we decided for the 2D studies to locate the (2D parts of the) stents only in direct connection to the aneurysm.

5.3.1 Aneurysm Configuration

We employ the proposed numerical methods for aneurysm hemodynamics, which include the interaction of the flow with the deformable material. This numerical simulation aims to relate the aneurysm state (unrupture or rupture) with wall pressure, wall deformation and effective wall stress, which would provide information for the diagnosis and treatment of unrupture and rupture of an aneurysm by elucidating the risk of bleeding or re-bleeding, respectively. Several research groups focus on CFD simulations with realistic 3D geometries, assuming rigid walls (see [46, 2, 129]). On the contrary, comparing our studies with the CFD literature, we concentrate on the complex interaction between elastic deformations and flow perturbations induced by the stent, to analyze qualitatively the influence of geometrical details onto the elastic material behavior, particularly in view of more complex blood models and constitutive equations for the structure.

Therefore, the aims of our studies can be described as follows:

1. What is the influence of the elasticity of the walls onto the flow behavior inside of the aneurysm, particularly w.r.t. the resulting shape of the aneurysm?
2. What is the influence of the geometrical details of the (2D) stents, that means shape, size, position, onto the flow behavior into and inside of the aneurysm?
3. Do both aspects, small-scale geometrical details as well as elastic fluid-structure interaction, have to be considered simultaneously or is one of them negligible in first order approximation?
4. Are modern numerical methods and corresponding CFD simulations tools able to simulate qualitatively the multi-physics behavior of such biomedical configurations?

The geometry of the fluid domain under consideration is currently based on 2D models (see Fig. 5.33) which allows us to concentrate on the detailed qualitative evaluation of our approach based on the described monolithic ALE formulation. The underlying construction of the (2D) shape of the aneurysm can be explained in the Table 5.7 and for further explanation about the construction of meshes see [124, 111, 110]. The examined stents are of circular shape, placed on the neck of the aneurysm, and we use

Table 5.7: Overview of the geometry parameters.

without aneurysma		values [mm]	with aneurysma		value [mm]
innermost circle radius	r_1	6	anuerysma middle	m	$(-6.75, 6)$
next circle radius	r_2	8	inner fundus radius	r_4	1.125
last circle radius	r_3	8.25	outer fundus radius	r_5	1.25

three, resp., five stents (simplified ‘circles’ in 2D as cut-planes from 3D configurations) of different size and position. The stents also consist of a grid, immersed in the blood flow, which is located at the inlet of the aneurysm so that in future elastic deformations of the stents can be included, too, since in real life, the stent is a medical device which consists of a metal wire tube. Stents are typically used to keep arteries open and are located on the vessel wall while this stent is immersed in the blood flow (Fig. 5.33). The purpose of this device is to reduce the flux into and within the aneurysm in order to occlude it by a clot or rupture. Flow through a deformable vein with elastic walls of a brain aneurysm is simulated to analyze qualitatively the described methods; here, the flow is driven by prescribing the flow velocity at the inflow section while the elastic part of the boundary is either fixed or stress-free. Both ends of the walls are fixed, and the flow is driven by a periodical change of the inflow at the left end. The*no-slip* condition is prescribed for the fluid on the other boundary parts, i.e. top and bottom wall, stents and fluid-structure interface. The natural outflow condition at the lower left part effectively prescribes some reference value for the pressure variable p, here $p = 0$. While this value could be arbitrarily set in the incompressible case, in the case of a compressible structure this might have influence onto the stress and consequently the deformation of the solid.

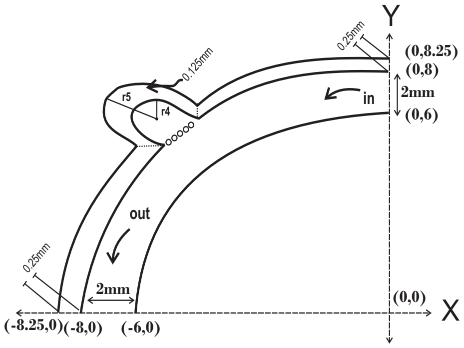

Figure 5.33: Schematic drawing of the measurement section.

Table 5.8: Parameter values.

structure	parameter	values	fluid	parameter	values
density	$\rho^s\ [10^{-6}\frac{\mathrm{kg}}{\mathrm{mm}^3}]$	1.12	density	$\rho^f\ [10^{-6}\frac{\mathrm{kg}}{\mathrm{mm}^3}]$	1.035
poisson ratio	ν^s	0.4	viscosity	$\nu^f\ [\frac{\mathrm{mm}^2}{\mathrm{s}}]$	3.38
shear modulus	$\mu^s\ [\frac{\mathrm{kg}}{\mathrm{mms}^2}]$	42.85	velocity	$\bar{U}\ [\frac{\mathrm{mm}}{\mathrm{s}}]$	20
Young modulus	$E\ [\frac{\mathrm{kN}}{\mathrm{mm}^2}]$	120	Reynolds number	Re	120

In the following, we show some corresponding results for the described prototypical aneurysm geometry, by using parameter values from Table 5.8, first for the steady state inflow profile, followed by non-steady tests for the pulsatile inflow, both with rigid and elastic walls, respectively. Also, results for non-Newtonian Carreau model are given at the end.

5.3.2 Steady Configurations

The (steady) velocity profile, to flow from the right to the left part of the channel, is defined as parabolic inflow, namely

$$\mathbf{v}^f(0,y) = \bar{U}(y-6)(y-8), \tag{5.5}$$

which is not time-dependent. Due to the low Re number, the flow behavior leads to a steady state which only depends on the elasticity and the shape of the stents. Moreover, for the following simulations, we only treat the aneurysm wall as elastic structure. Then, the aneurysm undergoes some slight deformations which can be seen in the Fig. 5.34. Moreover they result in a different volume of the flow domain (see Fig. 5.35).

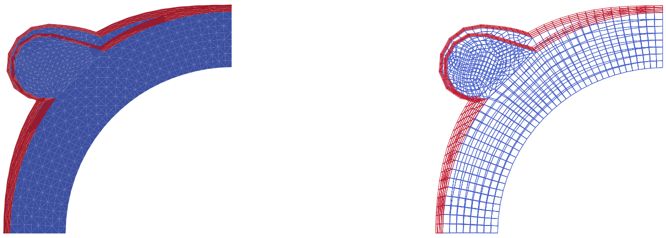

Figure 5.34: Deformed mesh for steady configuration without stents, with elastic wall (left). Mesh for rigid wall (776 elements) (right).

Particularly the influence of the number of stents onto the complete fluid flow through

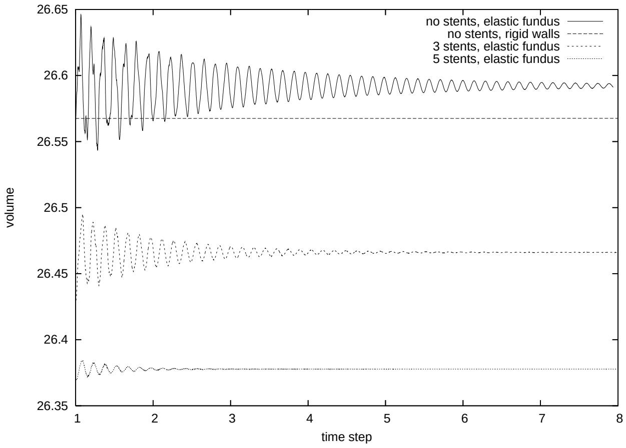

Figure 5.35: Resulting volume of the fluid domain for different configurations.

the channel including the aneurysm can be clearly seen. Summarizing these results for steady inflow, the simulations show that the stent implantation across the neck of the aneurysm prevents blood penetration into the aneurysma. Moreover, the elastic geometrical deformation of the wall is slightly reduced by implanting the stents while the local flow behavior inside of the aneurysm is more significantly influenced by the elastic properties of the outer wall, particularly due to the different width between stents and walls of the aneurysm as can be seen in the Figures. 5.36, 5.37, 5.38, 5.39.

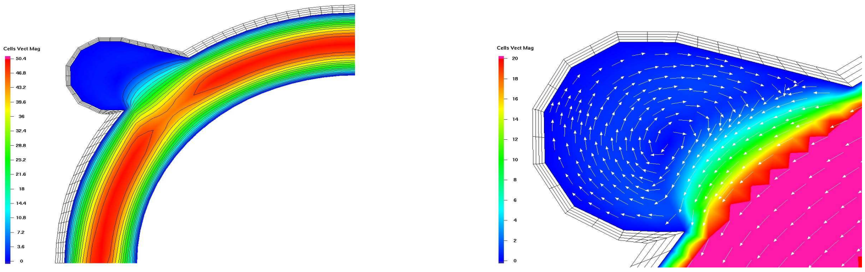

Figure 5.36: Left: Rigid walls with no stents, blood flow vector magnitude., Right: Scaled to view fluid flow concentration inside aneurysm.

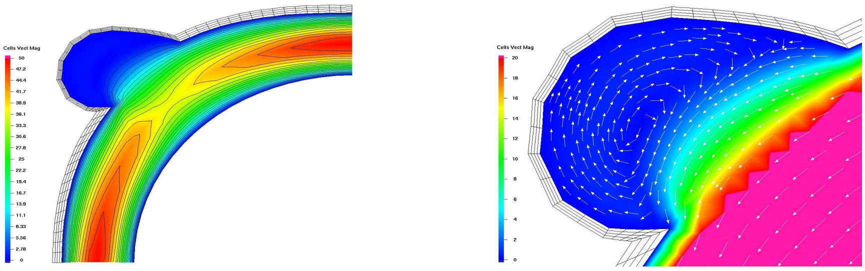

Figure 5.37: Left: Elastic walls with no stents, blood flow vector magnitude., Right: Scaled to view fluid flow concentration inside aneurysm.

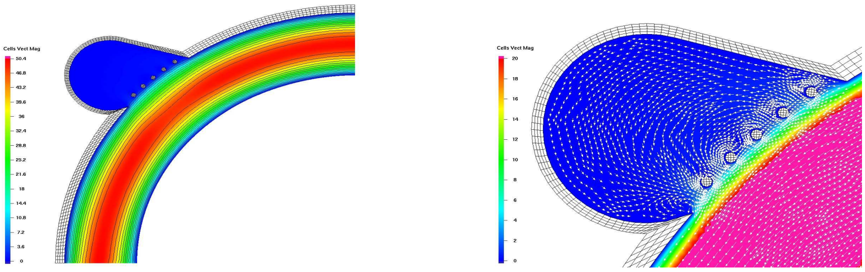

Figure 5.38: Left: Rigid walls with stents, blood flow vector magnitude., Right: Scaled to view fluid flow concentration inside aneurysm.

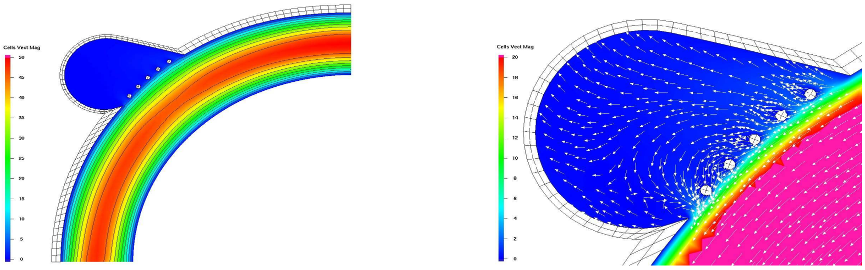

Figure 5.39: Left: Elastic walls with stents, blood flow vector magnitude., Right: Scaled to view fluid flow concentration inside aneurysm.

5.3.3 Pulsatile Configurations

Correspondingly, the pulsatile inflow profile for the non-steady tests for which peak systole and diastole occur for $\Delta t = 0.25s$ and $\Delta t = 0.75s$ respectively, is prescribed as

$$\mathbf{v}^f(t,0,y) = \mathbf{v}^f(0,y)(1+0.75sin(2\pi t)). \tag{5.6}$$

We show again (see Fig. 5.40) the resulting volume of the flow domain for 5, 3 and no stents. In all cases, the oscillating behavior due to the pulsative inflow is visible which also leads to different volume sizes. For the resulting flow behavior, we see global differences w.r.t. the channel flow near the aneurysm, due to the different flow rate into the aneurysm in case of 5, 3, and no stents. Moreover, significant local differences inside of the aneurysm can be observed, which means, attenuation of blood flow inside aneurysm as the stent implanted across the neck of aneurysm (see Fig. 5.41).

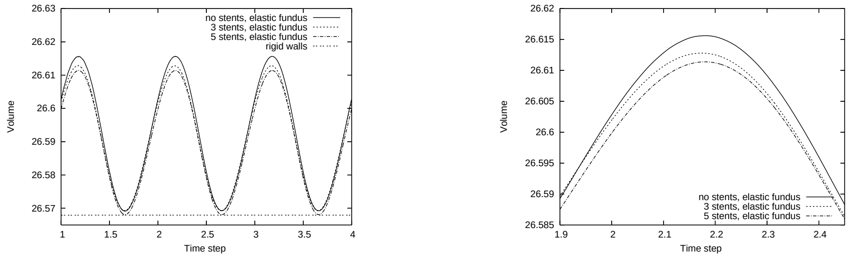

Figure 5.40: Domain volume with rigid and elastic behavior of the aneurysm wall.

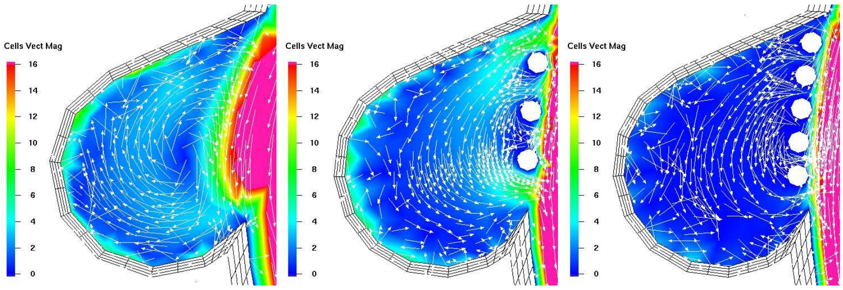

Figure 5.41: Blood flow flux inside aneurysm is less for 5 stents compare to 3 or no stents.

5.3.4 Non-Newtonian Model

We considered the effects of a non-Newtonian fluid model on hemodynamics. The Carreau fluid model was selected because it is an accurate model to describe the rheological behavior of blood [82]. Experimental tests show that blood exhibits shear thinning apart of other non-Newtonian phenomena[129]. Thus, in order to include this feature the viscosity in the following form is used.

$$\mu(|\mathbf{D}(\mathbf{v})|) = \mu_\infty + (\mu_0 - \mu_\infty)(1+K|\mathbf{D}(\mathbf{v})|^2)^n. \tag{5.7}$$

The Carreau blood model predicts decreasing viscosity at high strain, where μ_0 and μ_∞ are low and high shear rate asymptotic values, and parameters K and n control the transition region. We have taken the parameter values as $\mu_\infty = 0.00345Ns/m^2$, $\mu_0 = 0.056Ns/m^2$, $K = 10.976$ $n = -0.3216$ and other parameters, configurations are same as was for pulsatile configuration.

The corresponding parametrization was based on abstractions of biomedical data (i.e., cut planes of 3D specimens from New Zealand white rabbits as well as computer tomographic (see figure 5.42 right) and magnetic resonance imaging data of human neurocrania). A very complex mesh (5.42 left) is constructed based on this image (i.e figure 5.42 right). The green and red color part in figure 5.42 (left) are for elastic walls and they can have separate stiffness. Blue color is the flow region.

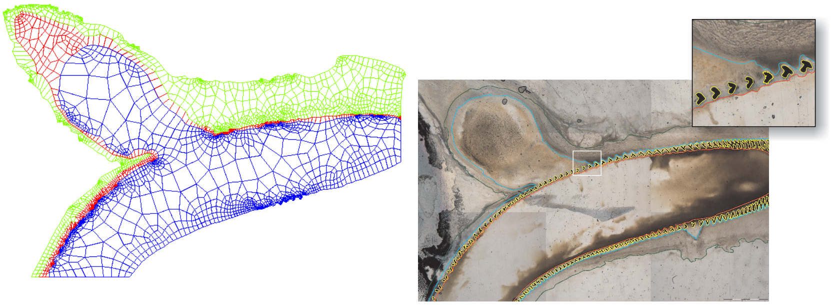

Figure 5.42: Left: Mesh constructed. Right: Histologic sample of aneurysm.

Figure 5.43 show the effective stress distribution at peak systole. The pressure on the wall is nearly constant after the flow is fully developed, see figure 5.44. The intensity of flow behavior to the aneurysm is shown in figure 5.45 by mean of the vector magnitude of the blood flow. It is shown by two ways, at top of the figure complete domain is shown and at bottom flow inside the aneurysm is shown.

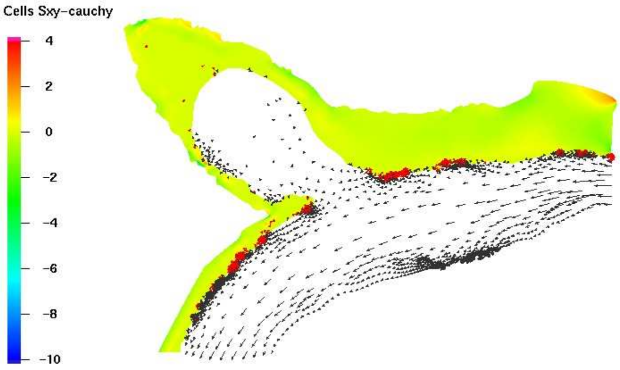

Figure 5.43: Effective stress distributions.

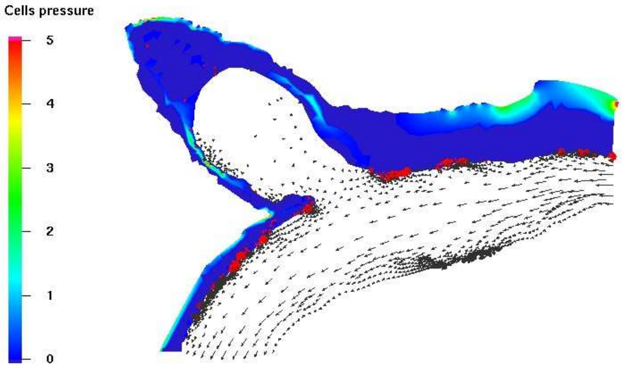

Figure 5.44: Pressure distributions.

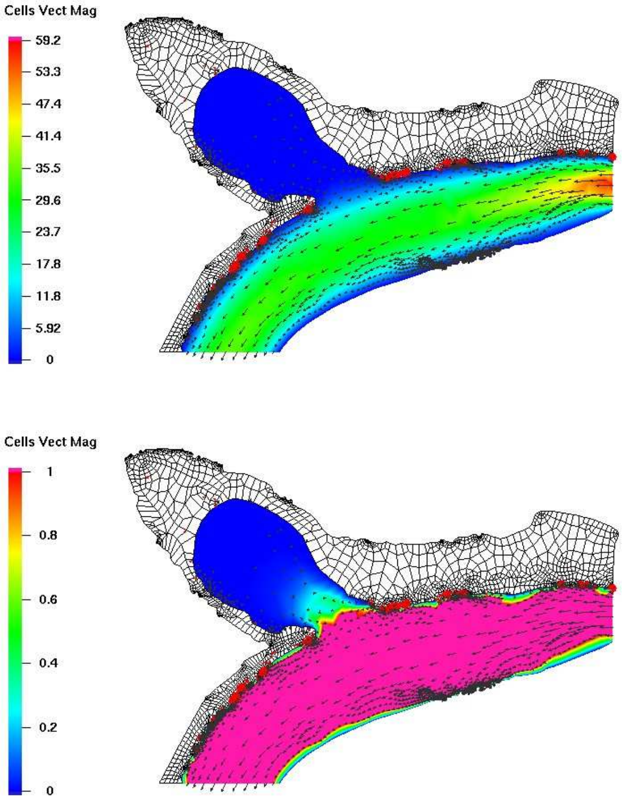

Figure 5.45: Top: FLow vector magnitude complete domain. Bottom: Flow vector magnitude inside aneurysm.

Have patience. All things are difficult before they become easy.
Saadi

6

Fluid-Structure Interaction Optimization

In recent years encouraging progress has been made in the numerical simulation of fluid-structure interaction (FSI) problems. However, the development of efficient simulation-based optimization techniques for the optimal design of FSI systems is still in its infancy. This Chapter will concerns to develop an efficient methods for fluid structure interaction optimization, which will combine modern techniques from PDE-constrained optimization, design optimization of stationary as well as non-stationary strongly coupled FSI problems and multigrid FSI simulation methods in near future based on monolithic ALE approach.

Before stating FSI-Opt benchmark an overview of optimization, historical development of optimization methods and its applicability to vast real application is glanced through.At the end of the Chapter the results for FSI1-Opt benchmark are presented and the future possible extensions hinted.

6.1 Overview

Optimization is the discipline of mathematics in which to get the best result under certain conditions is aimed. Almost every engineering system requires design construction and later its maintenance. The ultimate goal is either to minimize the effort needed or to maximize the desired benefit. Hence optimization can be defined as the process of finding the conditions that give the minimum or maximum value of a function, where the function represents the effort needed or the desired benefit.

Historical Developments The major recently developed novel approaches are goal programming for multi-objective optimization, genetic algorithms, simulated annealing and neural network methods. Engineering applications of optimization with different modeling approaches and optimization techniques are growing with time.

The existence of optimization methods go to the days of Newton, Lagrange, and Cauchy. The work of Newton and Leibnitz to differential calculus made feasible the differential calculus methods for optimization. The calculus of variations dealing with the minimization of functions founded by Bernoulli, Euler, Lagrange, and Weistrass. The constrained optimization problems, which involve the addition of unknown multipliers, is known by the name of its inventor, Lagrange. The pioneer implementation of the steepest descent method made by Cauchy to solve unconstrained optimization problems [55]. By the invent of the high-speed digital computers it became feasible to implement the complex optimization operations and further research on newer methods advanced. This opened the new areas in optimization methods.

They are outlined here with a few milestones.

1. The simplex method for linear programming problems developed by Dantzig in 1947 [37, 38].
2. The principle of optimality for dynamic programming problems is stated by Bellman in 1957 [11].
3. Work by Kuhn and Tucker in 1951 on the necessary and sufficient conditions for the optimal solution of programming problems laid the foundation for later research in non-linear programming [85].
4. The contributions of Zoutendijk and Rosen to nonlinear programming during the early 1960s have been very significant [112, 113, 136].
5. Work of Carroll [23] and Fiacco and McCormick facilitated many difficult problems to be solved by using the well-known techniques of unconstrained optimization [49, 47, 48].
6. Geometric programming was developed in the 1960s by Duffin, Zener, and Peterson [101, 45].
7. Gomory did pioneering work in integer programming, one of the most exciting and rapidly developing areas of optimization. The reason for this is that most real world applications fall under this category of problems [59, 60].
8. Dantzig and Charnes and Cooper developed stochastic programming techniques [25, 26, 27] and solved problems by assuming design parameters to be independent and normally distributed.

Engineering Applications of Optimization To indicate the widespread scope of the subject, some typical applications in different engineering disciplines are:

- Design of civil engineering structures such as frames, foundations, bridges, towers, chimneys and dams for minimum cost.
- Design of minimum weight structures for earth quake, wind and other types of random loading.
- Optimal plastic design of frame structures (e.g., to determine the ultimate moment capacity for minimum weight of the frame).
- Design of water resources systems for obtaining maximum benefit.
- Design of optimum pipeline networks for process industry.
- Design of aircraft and aerospace structure for minimum weight.
- Design of pumps, turbines and heat transfer equipment for maximum efficiency.

- Optimum design of electrical machinery such as motors, generators and transformers.
- Optimum design of electrical networks, control systems, chemical processing equipments and plants .

In the below section, the configuration of the problem is documented then the employed Nelder-Mead method to very own benchmark setting is explained followed by the computation results.

6.2 FSI Optimization Benchmarking

The main purpose of this benchmark scenario is to describe specific configurations which shall help in future to test and to compare different numerical methods and code implementations for the fluid-structure interaction (FSI) problem which can be additionally coupled with an additional optimization procedure. This FSI optimization benchmark is based on 2D steady FSI problem based on the benchmark configuration of Turek and Hron [123] with additional altered boundary control flows as shown in figure 6.5. The idea is to integrate the FSI solver into an optimization procedure for FSI problems. Furthermore, these FSI configurations can be extended towards optimal control of body forces acting on and deformations of the elastic object in which case additional outer in flow/out flow regions control the optimal result.

6.2.1 Optimizer

As optimizer a derivative-free optimization method for this unconstrained minimization problem is chosen, which is the SIMPLEX algorithm developed by Nelder and Mead [86, 95]. The method is wide spread due to the fact that is makes no assumptions about the objective functional except that it is continuous. Furthermore, it is quite numerically robust [10, 92]. The basic operations (reflection, expansion, and contraction) of this method are explained in the following .

Nelder-Mead Method

A simplex method for finding a local minimum of a function of several variables has been devised by Nelder and Mead [95, 86]. For two variables, a simplex is a triangle, and the method is a pattern search that compares function values at the three vertices of a triangle. The worst vertex, where $f(x,y)$ is largest, is rejected and replaced with a new vertex. A new triangle is formed and the search is continued. The process generates a sequence of triangles (which might have different shapes), for which the function values at the vertices get smaller and smaller. The size of the triangles is reduced and the coordinates of the minimum point are found.

The basic strategy is explained in the subsequent subsections.

Initial Triangle BGW Let $f(x,y)$ be the function that is to be minimized. To start, three vertices of a triangle are given: $V_k = (x_k, y_k)$, $k = 1,2,3$. The function $f(x,y)$ is then evaluated at each of the three points: $z_k = f(x_k, y_k)$ for $k = 1,2,3$. The subscripts are then reordered so that $z_1 \le z_2 \le z_3$. The notation

$$B = (x_1, y_1), \qquad G = (x_2, y_2), \qquad \text{and} \qquad W = (x_3, y_3), \tag{6.1}$$

are used to remember that B is the best vertex, G is good (next to best), and W is the worst vertex to be discarded.

Midpoint of the Good Side The building process uses the midpoint of the line segment joining B and G, by averaging the coordinates:

$$M = \frac{B+G}{2} = (\frac{x_1+x_2}{2}, \frac{y_1+y_2}{2}), \tag{6.2}$$

Reflection Using the Point R The function values decreases moving along the side of the triangle from W to B, and it decreases moving along the side from W to G. Hence it is feasible that $f(x,y)$ takes on smaller values at points that lie away from W on the opposite side of the line between B and G. A test point R that is obtained by ”reflecting” the triangle through the side BG is chosen. To determine R, we first find the midpoint M of the side BG. Then draw the line segment from W to M and call its length d. This last segment is extended a distance d through M to locate the point R (see Figure6.1). The vector formula for R is

$$R = M + (M - W) = 2M - W. \tag{6.3}$$

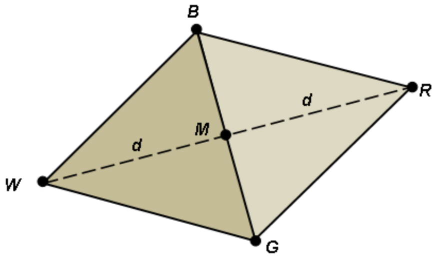

Figure 6.1: The triangle $\triangle BGW$ and midpoint M and reflected point R

Expansion Using the Point E If the function value at R is smaller than the function value at W, then we have moved in the correct direction toward the minimum. Perhaps the minimum is just a bit farther than the point R. So we extend the line segment through M and R to the point E. This forms an expanded triangle BGE. The point E is found by moving an additional distance d along the line joining M and R (see Figure 6.2). If the function value at E is less than the function value at R, then have to found a better vertex than R. The vector formula for E is

$$E = R + (R - M) = 2R - M. \tag{6.4}$$

.

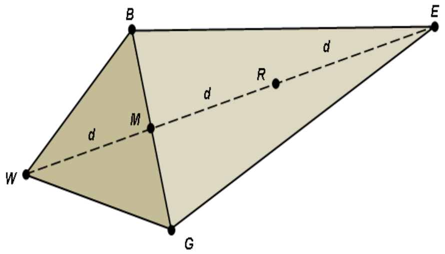

Figure 6.2: The triangle $\triangle BGW$ and point R and extended E

Contraction Using the Point C If the function values at R and W are the same, another point must be tested. Perhaps the function is smaller at M, but cannot replace W with M because there must have a triangle. Consider the two midpoints $C1$ and $C2$ of the line segments WM and MR, respectively (see Figure 6.3). The point with the smaller function value is called C, and the new triangle is BGC. Note. The choice between $C1$ and $C2$ might seem inappropriate for the two-dimensional case, but it is important in higher dimensions.

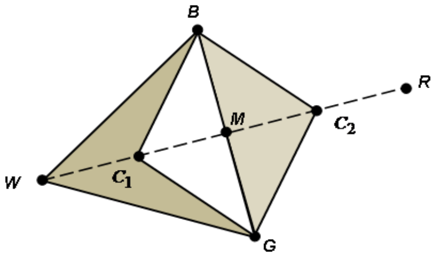

Figure 6.3: The contraction point C_1 or C_2.

Shrink toward B If the function value at C is not less than the value at W, the points G and W must be shrunk toward B (see Figure 6.4). The point G is replaced with M, and W is replaced with S, which is the midpoint of the line segment joining B with W.

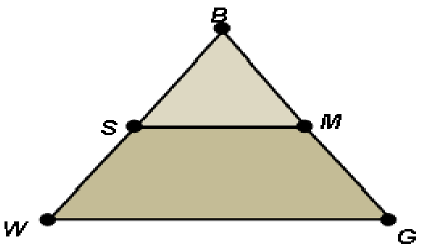

Figure 6.4: Shrinking the triangle toward B

6.2.2 Objectives

The objective of the following benchmarking scenario is to extend the validated FSI benchmark configurations to optimization problems such that minimal drag/lift values of the elastic object, minimal pressure loss or minimal non-stationary oscillations through boundary control of the inflow, change of geometry or optimal control of volume forces can be reached. The main design aim for the presented fluid structure interaction optimization problem is to minimize the lift on the beam with the help of boundary control of inflow data.

Further extension or design aim of this optimization problem is to measure minimal pressure loss, minimal non-stationary oscillations of the elastic beam through boundary control of inflow section, change of geometry (elastic channel walls or length/thickness of elastic beam), optimal control of volume forces. To implement optimization within monolithic FSI solver, the optimization components are defined below.

Definition The domain is based on the 2D version of the described FSI benchmark, see figure 6.5. The thickness of the beam is increased from 0.02 to 0.04 and other geometry parameters kept as defined in [123, 124]. As described before the beam is not symmetric so that the lift is not zero at the beginning.

An objective functional is the minimization of lift/drag forces on the deformable structures through boundary flow control. Mathematically this optimization problem can be written as

$$\text{minimize}\left(lift^2+\alpha V_C^2\right) \tag{6.5}$$

$$\text{subject to}\quad V_1, V_2, \tag{6.6}$$

The control velocity profile from top and bottom is prescribed in the following

$$v_C^f(x,0)=V_C=\begin{cases} V_1(x-0.45)(x-0.60), & \text{top}\\ V_2(x-0.45)(x-0.60), & \text{bottom}\end{cases} \tag{6.7}$$

where V_1 the magnitude of the parabolic velocity from/to top and V_2 velocity from/to below, these can be set directly when SIMPLEX method is not employed. The location of the inlet, outlet is shown in the schematic diagram of the geometry sketched in figure 6.5. The region through are coordinated at $(0.45,0)$ $(0.60,0)$ and $(0.45,0.41)$ $(0.60,0.41)$. However, V_1 and V_2 will be resulting velocities which results in minimum lift on beam when SIMPLEX Nelder Mead algorithm is in place.

A parabolic velocity profile is prescribed at the left channel inflow

$$v^f(0,y)=1.5\bar{U}\frac{y(H-y)}{\left(\frac{H}{2}\right)^2}=1.5\bar{U}\frac{4.0}{0.1681}y(0.41-y), \tag{6.8}$$

where $\bar{U}=0.2$ denotes the mean inflow velocity in x-direction and H denotes the channel height. Fluid and structural parameter values are based on the FSI1 benchmark as given in Chapter 5. The density and dynamic viscosity of fluid is $\rho^f=1000kg/m^3$, $\nu^f=1kg/ms$ respectively. Thus the Reynolds number is $Re=20$ based on the cylinder diameter. The structure density $\rho^s=1000kg/m^3$, the Young modulus $E=178000kg/ms^2$ and the Poisson ratio $\mu^s=0.4$ as set in the paper of Turek and Hron [123].

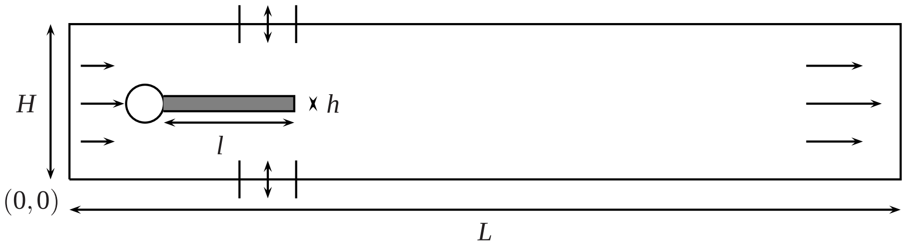

Figure 6.5: Geometry and computational domain of the configuration.

Finally, numerical results for this problem involving optimization for a steady fluid-structure interaction are given here to illustrate the capability of the approach considered.

6.3 Results

We simulated this FSI1-Opt configuration on same mesh refine level as used for FSI benchmark in Chapter 5. The reference value of lift force in case of stationary FSI calculation is $7.6e-1$ (see [124, 125] for more details). When we introduced or injected the flow with velocity $V_2 = 10$ from below the lift on the beam obviously increase see figure 6.6 which shows that it is wrong direction to inject flow. For the case when we suck the flow with same velocity $V_2 = 10$ from below we get the negative values of lift in increasing order see figure 6.7. If we inject flow from top and suck from below with same velocities $V_1 = V_2 = 10$ and not consider the simplex method then the resulting lift force on beam seems to be quite smeared, irregular and hard to predict or conclude what could be best coordinate which can give minimum lift. The flow vector magnitude behavior is shown in figure 6.8.

From this it is clear that $V_1 = V_2 > 10$ is not good idea to set. Hence it became clear that for the implementation of simplex method the coordinates of triangle should be between $[0,10]$. For numerical simulation we set the coordinates $(0,-3)$, $(3,3)$ and $(-3,3$ for two variable Nelder-Mead algorithm. For this case if the simplex method is in place lift goes to almost zero as shown in figure 6.9 and beam is almost static. Optimal points are then the (V_1,V_2) values which result in minimum lift on the beam depending on the parameter α. As α decreases we get the reduction of the lift on the beam and the optimal point $(1.06e+0, 1.08+1)$ for level 1, $(1.04e+0, 1.05e+01)$ for level 2 and for level 3 $(1.04e+0, 1.05e+01)$ using the simplex algorithm proposed by Nelder and Mead [95]. Results are shown in figures 6.10, 6.11 and 6.12, for level 1, level 2 and level 3 in respective order, which show the optimal velocity values V_1 and V_2 providing the minimum lift on the beam as compared with the FSI1 benchmark reference lift values which is $7.6e-1$. In Figure 6.10, it is quite visible that beam is not displaced i.e. no lift on the beam is observed due to the boundary control, and results are shown for three different mesh refinement levels. Lift force on the beam with changing α parameter is given in the corresponding tables 6.10, 6.11 and 6.12.

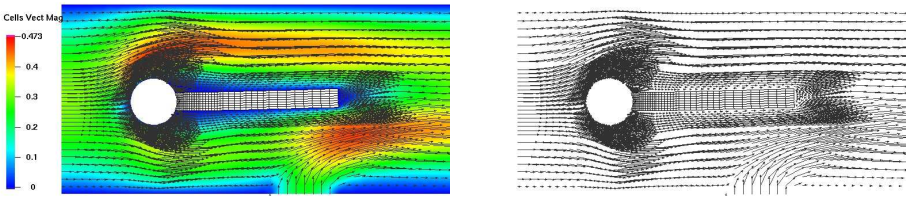

Figure 6.6: No SIMPLEX: Flow vector magnitude (Injection) level 3.

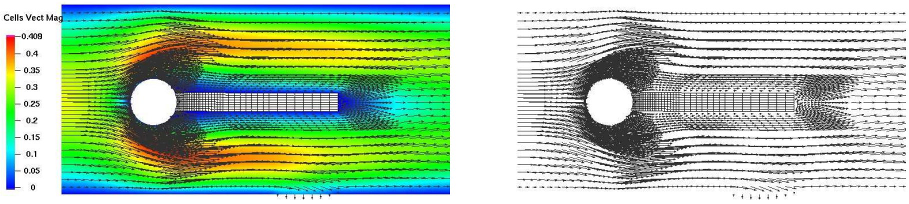

Figure 6.7: No SIMPLEX: Flow vector magnitude (suction) level 3.

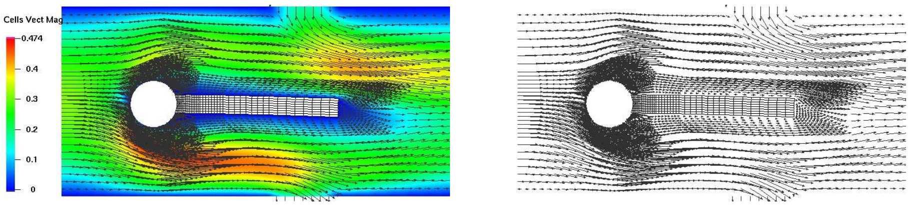

Figure 6.8: No SIMPLEX: Flow vector magnitude (Injection and suction) level 1.

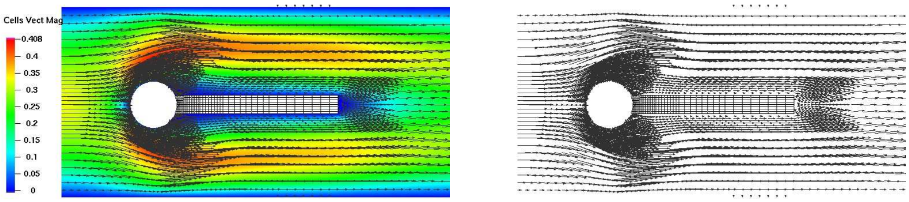

Figure 6.9: SIMPLEX: Flow vector magnitude (Injection and suction) level 1.

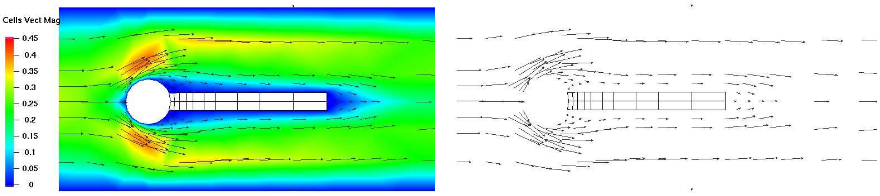

α		level 1	
	iter	optimal values(V_1,V_2)	lift
$1e+0$	57	$(3.74e-1, 3.88e-1)$	$8.1904e-1$
$1e-2$	60	$(1.04e+0, 1.06e+0)$	$2.2684e-2$
$1e-4$	73	$(1.06e+0, 1.08e+1)$	$2.3092e-4$
$1e-6$	81	$(1.06e+0, 1.08e+1)$	$2.3096e-6$

Figure 6.10: No displacement is visible of the beam due to optimal boundary flow control: Level 1

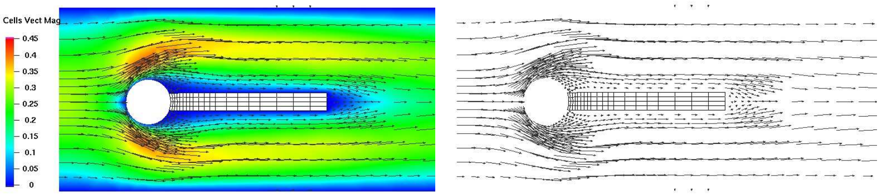

α		level2	
	iter	optimal values(V_1,V_2)	lift
$1e+0$	59	$(3.66e-1, 3.79e-1)$	$7.8497e-1$
$1e-2$	59	$(1.02e+0, 1.04e+0)$	$2.1755e-2$
$1e-4$	71	$(1.04e+0, 1.05e+01)$	$2.2147e-4$
$1e-6$	86	$(1.04e+0, 1.05e+01)$	$2.2151e-6$

Figure 6.11: No displacement is visible of the beam due to optimal boundary flow control: Level 2

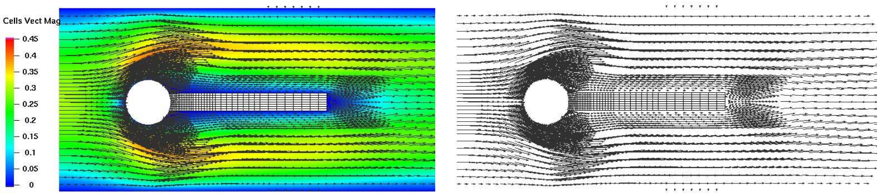

α		level3	
	iter	optimal values(V_1,V_2)	lift
$1e+0$	67	$(3.66e-1, 3.79e-1)$	$7.87e-1$
$1e-2$	77	$(1.02e+0, 1.06e+0)$	$1.97e-2$
$1e-4$	100	$(1.04e+0, 1.06e+0)$	$2.03e-4$
$1e-6$	100	$(1.04e+0, 1.06e+0)$	$1.3372e-6$

Figure 6.12: No displacement is visible of the beam due to optimal boundary flow control: Level 3

6.4 Summary

In this Chapter we have presented 2D benchmark results for monolithic ALE numerical approach for fluid-structure interaction optimization problem. we employed a derivative free mathematical optimization technique (see for more details [31, 92]). To the authors knowledge, this approach is not investigated yet in literature in the context of FSI optimization.

The simplex method presented is a robust algorithm for unconstrained optimization problems. Although, not all direct search methods reliably find solutions. Some algorithms, such as the simplex algorithm of Nelder and Mead, sometimes find minimizers very efficiently, but they can also fail unpredictably for many reasons. Thus it is necessary to circumvent this problem for constrained optimization so that simplex does not deteriorate. Interested readers are referred to [86] for a comprehensive survey of the original Nelder-Mead simplex algorithm and for its advantages and disadvantages.

In case one need to optimize more complex shape then more parameter will require then it is very hard to get solution through simplex method and it is required to use more sophisticated with this approach. As a outlook one could think for more complex optimization for instance some gradient based methods [53].

As an extension, corresponding 3D simulations are planned as well as the embedding into outer optimization tools (see `http://jucri.jyu.fi/?q=node/14` for a first attempt towards optimal control on the basis of the presented FSI1 configuration).

The scientific observer of Nature is a kind of mystic seeker in the act of prayer.

M. Iqbal

7

Conclusions and Outlook

The work presented in this thesis is based on the intensive research carried out to investigate the mathematical modeling for the fluid structure interaction problems and the validation to benchmark scenarios as well as its applicability for real life problems.

The performance of the proposed methodology has been analyzed by conducting extensive and accurate simulation based on experiments settings and compared with the existing standard benchmark settings. This concluding chapter will give a summary of the work undertaken and the results achieved towards the numerical solution and optimization of various aspects of FSI problems. It will also point out areas where further research is required in order to ensure a continual progress.

A summarized account of the various topics and respective contributions discussed and proposed in this thesis is provided in the subsequent sections below.

7.1 Summary and Conclusion

In this respect the contents of this thesis cover various aspects pertaining to the appropriate findings to enhance the performance of a monolithic ALE-FEM fluid-structure interaction solver.

Numerical techniques for solving the problem of fluid-structure interaction with an elastic material in a laminar incompressible viscous flow are described. An Arbitrary Lagrangian-Eulerian (ALE) formulation is used in a fully coupled monolithic way, considering the problem as one continuum. The mathematical description and the numerical schemes are designed in such a way that more complicated constitutive relations (and more realistic for biomechanics applications) for the fluid as well as the structural part can be easily incorporated. We utilize the well-known Q_2P_1 finite element pair for discretization in space to gain high accuracy and perform as time-stepping the 2nd order Crank-Nicholson, resp., Fractional-Step-θ-scheme for both solid and fluid parts. The resulting nonlinear discretized algebraic system is solved by a Newton method which approximates the Jacobian matrices by a divided differences approach, and the resulting linear systems are solved by iterative solvers, preferably of Krylov-multigrid type.

For validation and evaluation of the accuracy of the proposed methodology, we present corresponding results for a new set of FSI benchmarking configurations (‘channel flow around cylinder with attached elastic beam’, see [123]) which describe the self-induced elastic deformation of a beam attached to a cylinder in laminar channel flow, allowing stationary as well as periodically oscillating deformations.

Results have been given for the structure consisting of a thin elastic beam attached to the cylinder and at the trailing end of the beam a rear mass is attached in laminar flow.

We simulated two cases corresponding to the thickness of the beam to be $1mm$ and $0.04mm$, respectively. Additionally, we present numerical studies on different mesh types. Numerical results are provided for all time stepping schemes which show very reproducible symmetrical two–dimensional swiveling motions. These numerical tests show that the solution is independent of the mesh type and mesh refinement level. Preliminary results for the experimental benchmark configuration are shown to see the qualitative behavior of the elastic beam for a high velocity profile fluid.

Then, as an example for fluid-structure interaction (FSI) in biomedical problems, the influence of endovascular stent implantation onto cerebral aneurysm hemodynamics is numerically investigated. The aim is to study the interaction of the elastic walls of the aneurysm with the geometrical shape of the implanted stent structure for prototypical 2D configurations. This study can be seen as a basic step towards the understanding of the resulting complex flow phenomena so that in future aneurysm rupture shall be suppressed by an optimal setting for the implanted stent geometry.

The used numerical methodology allows the system to be coupled with additional models of chemical and electric activation of the active response of the biological material as well as non-Newtonian models to describe the shear thinning property of the blood. Further extension to viscoelastic models and coupling with mixture based models for soft tissues together with chemical and electric processes would allow to perform more realistic simulations for real life applications. Future studies need to evaluate the applicability of this 2D approach to calculations in 3D.

7.2 Outlook

During the course of evaluating and comparing the performance of this proposed solver with the standard benchmark settings, various considerations came up. In order to enhance the overall capabilities and applicability of this approach, it is important to address few considerations as part of the future development road map. The contributions presented in this thesis are based on the proposition and analysis of novel benchmark settings for FSI.

It is evident that the computational complexity increases tremendously for full 3D problems and with more complicated models like visco-elastic materials for the fluid or solid components. The presented numerical method is accurate and robust with respect to the constitutive models. The possible next steps regarding better efficiency of the solvers include the development of improved multigrid solvers, for instance of global pressure Schur complement type [122], and the essential combination with parallel high performance computing techniques in future, particularly towards actual 3D configurations.

As mentioned before, the formulation kept general enough to allow immediate extension to more realistic material models. For example in the case of material anisotropy one can consider

$$\tilde{\Psi} = c_1(I_C - 3) + c_2(I\!I_C - 3) + c_3(|\mathbf{Fa}| - 1)^2,$$

with **a** being the preferred material direction. The term $|\mathbf{Fa}|$ represents the extension in the direction **a**. In the same manner the constitutive relation for the fluid can be directly extended to the power law models used to describe the shear thinning property of blood. Further extension to viscoelastic models and coupling with the mixture based model for soft tissues together with models for chemical and electric processes involved in biomechanical problems would allow to perform realistic simulations for real applications.

This thesis presented the proof-of-concept of the proposed solver towards enhancing 3D real life application of the code and collecting the feasible data respectively. For this purpose the performance was analyzed based on certain assumptions.

However, as part of the future research the recommendation to be incorporated for further tests are analyzed in the following section.

7.3 Vision for the Future

Throughout the discussion presented in this thesis, focus has been to provide and test the solver for benchmark settings and extend it to real life applications. The topic of biomechanics holds great relevance as transition towards the realization of future need of numerical simulation in this era.

The future scenario and aim for the cerebral aneurysm settings is to extend it to an 3D cerebral aneurysm hemodynamics application comprising of real life data received by the medical partners. However, to handle such situations it is imperative to have effective numerical tool, mechanisms in place.

Furthermore, the benchmarking scenario has to extend the validated FSI benchmark configurations to optimization problems such that minimal drag/lift values of the elastic object, minimal pressure loss or minimal non-stationary oscillations of the elastic beam through boundary control of the inflow, change of geometry (elastic channel walls or length/thickness of elastic beam) or optimal control of volume forces can be reached. The simulation is based on the described FSI1 configuration. At present the Simplex method according to Nelder and Mead [86] is chosen, which is a derivative free optimization method for unconstrained minimization problems and quite numerically robust but it requires big CPU time for computation even for less degrees of freedoms. Aim is to apply the gradient base method in the adjoint operator presence and for non-stationary problem settings to minimize the lift on the beam via boundary control.

We believe that such basic studies may help towards the development of future ‘Virtual Flow Laboratories’ which individually assist to develop personal medical tools in an individual style.

Bibliography

[1] R. A. Adam. *Sobolev spaces*. Academic Press, 1st Edition, 1975.

[2] S. Appanaboyina, F. Mut, R. Löhner, E. Scrivano, C. Miranda, P. Lylyk, C. Putman, and J. Cebral. Computational modelling of blood flow in side arterial branches after stenting of cerebral aneurysm. *International Journal of Computational Fluid Dynamics*, 22:669–676, 2008.

[3] R. Armentano, J. L. Megnien, A. Simon, F. Bellenfant, J. Barra, and J. Levenson. Effects of hypertension on viscoelasticity of carotid and femoral arteries in humans. *Hypertension*, 26(1):48–54, 1995.

[4] R. L. Armentano, J. G. Barra, J. Levenson, A. Simon, and R. H. Pichel. Arterial wall mechanics in conscious dogs: assessment of viscous, inertial, and elastic moduli to characterize aortic wall behavior. *Circ. Res.*, 76:468–478, 1995.

[5] D. N. Arnold, D. Boffi, and R. S. Falk. Approximation by quadrilateral finite element. *Math. Comput.*, 71:909–922, 2002.

[6] I. Babuska. Courant element before and after. In M. Krizek, P. Neittaanmäki, and R. Stenberg, editors, *Finite Element Methods: Fifty years of the courant element*, volume 164 of *Lecture notes in pure and applied mathematics*. Springer, 2006.

[7] J. Baranger and D. Sandri. Formulation of stokes problem and the linear elasticity equations suggested by oldroyd model for viscoelastic flow. *Math. Modell. Numer. Anal.*, 2(26):231–345, 1992.

[8] R. Barrett, M. Berry, T. F. Chan, J. Demmel, J. Donato, J. Dongarra, V. Eijkhout, R. Pozo, C. Romine, and H. Van der Vorst. *Templates for the solution of linear systems: Building blocks for iterative methods*. SIAM, Philadelphia, PA 1994.

[9] R. D. Bauer, R. Busse, A. Shabert, Y. Summa, and E. Wetterer. Separate determination of the pulsatile elastic and viscous forces developed in the arterial wall in vivo. *Pflugers Arch*, 380:221–226, 1979.

[10] G. Becker, J. Siegmann, J. Michaelis, and M. Schäfer. Comparison of a derivative-free and derivative-based shape optimization method. In J. M. Rodrigues, H. C. Guedes, P. R. Fernandes, and M. M. Neves, editors, *Proceeding of the 8th World Congress on Structural and Multidisciplinary Optimization*. Springer, lisbon, Portugal, 2009.

[11] R. Bellman. *Dynamic Programming*. Princeton University Press, USA, 1957.

[12] T. B. Belytschko. Methods and programs for analysis of fluid-structure systems. *Nuclear Engineering Design*, 42:41–52, 1977.

[13] T. B. Belytschko, D. P. Flanagan, and J. M. Kennedy. Finite element method s with user-controlled meshes for fluid- structure interaction. *Computer Methods in Applied Mechanics and Engineering*, 33:669–688, 1982.

[14] T. B. Belytschko and J. M. Kennedy. A fluid-structure finite element method for the analysis of reactor safety problems. *Nuclear Engineering Design*, 38:71–81, 1976.

[15] T. B. Belytschko and J. M. Kennedy. Computer models for subassembly simulation. *Nuclear Engineering Design*, 49:17–38, 1978.

[16] T. B. Belytschko and R. Mullen. Two-dimensional fluid-structure impact computations with regularization. *Computer Methods in Applied Mechanics and Engineering*, 27:139–154, 1981.

[17] T. B. Belytschko and U. Schumann. Fluid structure interactions in light water reactor systems. *Nuclear Engineering Design*, 60:173–195, 1980.

[18] D. J. Benson. An efficient, accurate, simple ale method for nonlinear finite element programs. *Computer Methods in Applied Mechanics and Engineering*, 89:305–350, 1984.

[19] R. B. Bird, R. C. Armstrong, and O. Hassager. *Dynamics of Polymeric Liquids,*, volume 1. John Wiley & Sons, Cambridge, 1987.

[20] D. Boffi and L. Gastaldi. On the quadrilateral Q_2P_1 element for the stokes problem. *Int. J. Numer. Meth. Fluids.*, 39:1001–1011, 2002.

[21] J. Bonet and R. D. Wood. *Nonlinear continuum mechanics for finite element analysis*. Cambridge University Press, Cambridge, 1997.

[22] R. Bramley and X. Wang. *SPLIB: A library of iterative methods for sparse linear systems*. http://www.cs.indiana.edu/ftp/bramley/splib.tar.gz, Department of Computer Science, Indiana University, Bloomington, IN,, 1997.

[23] C. W. Carroll. The created response surface technique for optimizing nonlinear restrained systems. *Operations Research*, 9:169–184, 1961.

[24] A. Chambolle, B. Desjardins, M. J. Esteban, and C. Grandmont. Existence of weak solutions for the unsteady interaction of a viscous fluid within an elastic plate. *J.Math. Fluid Mech.*, 7(3):368–404, 2005.

[25] A. Charnes and W. W. Cooper. Chance-constrained programming. *Management Science*, 6:73–79, 1959.

[26] A. Charnes and W. W. Cooper. Chance constrainted programs with normal deviates and linear decision rules. *Naval Research Logistics Quarterly*, 7:533–544, 1960.

[27] A. Charnes, W. W. Cooper, and G. L. Thompson. Critical path analysis via chance constrained and stochastic programming. *Operations Research*, 12:460–470, 1964.

[28] P. G. Ciarlet. *Numerical Analysis of the Finite Element Method*. University of Montreal, Canada, 1976.

[29] P. G. Ciarlet. *Mathematical Elasticity. Volume I, Three-Dimensional Elasticity*, volume 20 of *Studies in Mathematics and its Applications*. North-Holland, Amsterdam, 1988.

[30] P. G. Ciarlet and V. Lods. Asymptotic analysis of linearly elastic shells. iii: Justification of koiter's shell equations. *Arch. Ration. Mech. Anal.*, 136(2):191–200, 1996.

[31] A. R. Conn, K. Scheinberg, and L. N. Vicente. *Introduction to derivative-free optimization*. SIAM, Philadelphia, PA 2009.

[32] K. D. Costa, P. J. Hunter, Rogers J. M., J. M. Guccione, L. K. Waldman, and A. D. McCulloch. A three-dimensional finite element method for large elastic deformations of ventricular myocardum: I – Cylindrical and spherical polar coordinates. *Trans. ASME J. Biomech. Eng.*, 118(4):452–463, 1996.

[33] K. D. Costa, P. J. Hunter, J. S. Wayne, L. K. Waldman, J. M. Guccione, and A. D. McCulloch. A three-dimensional finite element method for large elastic deformations of ventricular myocardum: II – Prolate spheroidal coordinates. *Trans. ASME J. Biomech. Eng.*, 118(4):464–472, 1996.

[34] D. Coutand and S. Shkoller. Motion of an elastic solid inside an incompressible viscous fluid. *Arch. Ration. Mech. Anal.*, 176(1):25–102, 2005.

[35] M. Crouzeix and P. A. Raviart. Conforming and non-conforming finite elements for solving the stationary stokes equations. *R.A.I.R.O. Anal. Numï¿*$\frac{1}{2}$*r*, 7:33–76, 1973.

[36] C. Cuvelier, A. Segal, and A. A. van Steenhoven. *Introduction to the Finite Element Method*. D. Reidel Publishing Company, 1986.

[37] G. B. Dantzig. Linear programming under uncertainty. *Management Science*, 1:197–206, 1955.

[38] G. B. Dantzig and M. N. Thapa. *Linear Programming: Theory and extensions*. Springer Series on Operations Research, Stanford, USA, 2003.

[39] T. A. Davis. Algorithm 832: Umfpack, an unsymmetric-pattern multifrontal method. *SACM Trans. Math. Software*, 30(4):196–199, 2004.

[40] T. A. Davis and I. S. Duff. A combined unifrontal/multifrontal method for unsymmetric sparse matrices. *SACM Trans. Math. Software*, 25:1–19, 1999.

[41] T. A. Davis and I. S. Duff. A column pre-ordering strategy for the unsymmetric-pattern multifrontal method. *SACM Trans. Math. Software*, 30(4):165–195, 2004.

[42] J. Donea. Arbitrary lagrangian-eulerian finite element methods. In T. B. Belytschko and T. J. R. Hughes, editors, *Numerical Methods for Transient Analysis*, pages 473–516. Amsterdam, North Holland, 1983.

[43] J. Donea, S. Giuliani, and J. P. Halleux. An arbitrary lagrangian-eulerian finite element method for transient dynamic fluid structure interactions. *Computer Methods in Applied Mechanics and Engineering*, 33:689–723, 1982.

[44] J. Donea and A. Huerta. *Finite element methods for flow problems*. John Willey and Sons, England, 2003.

[45] R. J. Duffin, E. L. Peterson, and C. Zener. *Geometric Programming: Theory and Application*. Wiley New York, USA, 1967.

[46] M. A. Fernandez, J-F. Gerbeau, and V. Martin. Numerical simulation of blood flows through a porous interface. *ESAIM: Mathematical Modelling and Numerical Analysis*, 42:961–990, 2008.

[47] A. V. Fiacco and G. P. McCormick. Programming under nonlinear constraints by unconstrained minimization: a primal-dual method. *Research Analysis Corp.*, pages RAC–TP–96, 1963.

[48] A. V. Fiacco and G. P. McCormick. The sequential unconstrained minimization technique for programming with equality constraint. *Research Analysis Corp.*, pages RAC–TP–155, 1965.

[49] A. V. Fiacco and G. P. McCormick. *Nonlinear programming: sequential unconstrained minimization techniques*. SIAM, 1990.

[50] A. Fortin. Old and new finite finite elements for incompressible flows. *Int. J. for Numer. Meth. in Fluids.*, 1:347–364, 1981.

[51] Y. C. Fung. *Biomechanics: Mechanical Properties of Living Tissues.* Springer-Verlag, New York, 1993.

[52] S. Geller, M. Bettah, M. Krafczyk, S. Kollmannsberger, D. Scholz, A. Düster, and E. Rank. An explicit model for three-dimensional fluid-structure interaction using lbm and p-fem. In H.-J. Bungartz, M. Mehl, and M. Schäfer, editors, *Fluid-Structure Interaction II: Modelling, Simulation, Optimisation*, volume 73 of *Lecture Notes in Computational Science and Engineering*, pages 285–326. Springer, 2010.

[53] P. Ghisbain. *Application of a gradient-based algorithm to structural optimization*. Massachusetts Institute of Technology, Dept. of Civil and Environmental Engineering, 2009.

[54] S. Ghosh and N. Kikuchi. An arbitrary lagrangian-eulerian finite element method for large deformation analysis of elastic-viscoplastic solids. *Computer Methods in Applied Mechanics and Engineering*, 86:127–188, 1991.

[55] A. A. Goldstein. Cauchy's method of minimization. *Numer. Math.*, 4:146–150, 1962.

[56] J. P. Gomes and H. Lienhart. Experimental study on a fluid-structure interaction reference test case. In H.-J. Bungartz and M. Schäfer, editors, *Fluid-Structure Interaction: Modelling, Simulation, Optimisation*, volume 53 of *Lecture Notes in Computational Science and Engineering*, pages 356–370. Springer, 2006.

[57] J. P. Gomes and H. Lienhart. Reference test cases for fluid-structure interaction studies. In S. Hartmann, A. Meister, M. Schäfer, and S. Turek, editors, *Fluid-Structure Interaction. Theory, Numerics and Applications*, pages 131–146, Kassel, 2009.

[58] J. P. Gomes and H. Lienhart. Experimental benchmark: Self-excited fluid-structure interaction test cases. In H.-J. Bungartz, M. Mehl, and M. Schäfer, editors, *Fluid-Structure Interaction: Modelling, Simulation, Optimisation*, volume 73 of *Lecture Notes in Computational Science and Engineering*, pages 383–411. Springer, 2010.

[59] R. E. Gomory. Faces of an integer polyhedron. *Proceedings of the National Academy of Sciences of the United States of America*, 57:16–18, 1967.

[60] R. E. Gomory. Some polyhedra related to combinatorial problems. *Linear Algebra and its Applications*, 2:451–558, 1969.

[61] C. Grandmont. Existence for an unsteady fluid-structure interaction problem. *ESAIM: M2AN*, 34(3):609–636, 2000.

[62] P. M. Gresho. On the theory of semi-implicit projection methods for viscous incompressible flow and its implementation via a finite element method that also introduces a nearly consistent mass matrix, part 1: Theory. *Int. J. Numer. Meth. Fluids.*, 11:587–620, 1990.

[63] M. Guidorzi, M. Padula, and P. Plotnikov. Galerkin method for fluids in domains with elastic walls. *University of Ferrara*, 2004.

[64] M. E. Gurtin. *Topics in Finite Elasticity*. SIAM, Philadelphia, PA, 1981.

[65] R. B. Haber. A mixed eulerian-lagrangian displacement model for large deformation analysis in solid mechanics. *Computer Methods in Applied Mechanics and Engineering*, 43:277–292, 1984.

[66] W. Hackbusch. *Multi-Grid Methods and Applications*. Springer-Verlag, Berlin, 1985. ISBN: 0-387-12761-5.

[67] P. Haupt. *Continuum Mechanics and Theory of Materials*. Springer, Berlin, 2000.

[68] M. Heil. Stokes flow in collapsible tubes: Computation and experiment. *J. Fluid Mech.*, 353:285–312, 1997.

[69] M. Heil. Stokes flow in an elastic tube: a large-displacement fluid-structure interaction problem. *Int. J. Num. Meth. Fluids*, 28(2):243–265, 1998.

[70] C. W. Hirt, A. A. Amsden, and J. L. Cook. An arbitrary lagrangian-eulerian computing method for all flow speeds. *Journal of Computational Physics*, 14:227–253, 1974.

[71] G. A. Holzapfel. *Nonlinear solid mechanics: A continuum approach for engineering.* John Wiley and Sons, Chichester, UK, 2000.

[72] G. A. Holzapfel. Determination of meterial models for arterial walls from uniaxial extension tests and histological structure. *International Journal for Numerical Methods in Fluids*, 238(2):290–302, 2006.

[73] J. Hron, A. Ouazzi, and S. Turek. A computational comparison of two fem solvers for nonlinear incompressible flow. In E. Bänsch, editor, *Challenges in Scientific Computing*, LNCSE, pages 87–109. Springer, 2002.

[74] J. Hron and S. Turek. *Lecture Notes in Computational Science and Engineering, Fluid-Structure Interaction –Modelling, Simulation, Optimization*. Springer, ISBN 3–540–34595–7, 2006.

[75] J. Hron and S. Turek. A monolithic FEM/multigrid solver for ALE formulation of fluid structure interaction with application in biomechanics. In H.-J. Bungartz and M. Schäfer, editors, *Fluid-Structure Interaction: Modelling, Simulation, Optimisation*, volume 53 of *Lecture Notes in Computational Science and Engineering*, pages 146–170. Springer, 2006.

[76] T. J. R. Hughes, W. K. Liu, and T. K. Zimmermann. Lagrangian eulerian finite element formulation for incompressible viscous flows. *Computer Methods in Applied Mechanics and Engineering*, 29:329–349, 1981.

[77] T. J. R. Hughes and T. E. Tezduyar. Finite element methods for first order hyperbolic systems with particular emphasis on the compressible euler equations. *Computer Methods in Applied Mechanics and Engineering*, 45:217–284, 1984.

[78] J. D. Humphrey. Mechanics of the arterial wall: review and directions. *Crit. Rev. Biomed. Eng.*, 23(1-2):1–62, 1995.

[79] J. D. Humphrey, R. K. Strumpf, and F. C. P. Yin. Determination of a constitutive relation for passive myocardium: I. A new functional form. *J. Biomech. Engng.*, 112(3):333–339, 1990.

[80] J. D. Humphrey, R. K. Strumpf, and F. C. P. Yin. Determination of a constitutive relation for passive myocardium: II. Parameter estimation. *J. of Biomech. Engng.*, 112(3):340–346, 1990.

[81] C. Johnson. *Numerical solution of partial differential equations by the finite element method*. Cambridge Uni. Press, 1994.

[82] B. M. Johnston, P. R. Johnston, S. Corney, and D. Kilpatrik. Non-newtonian blood flow in human right coronary arteries: steady state simulations. *Journal of Biomechanics*, 37:709–720, 2004.

[83] J. Kacur. *Method of Rothe in evolution equations*. BSB Teubner Verlag, 1985.

[84] C. Kelley. *Iterative Methods for Optimization*. SIAM, Philadelphia, 1999.

[85] H. W. Kuhn and A. W. Tucker. Nonlinear programming. In Jerzy Neyman., editor, *Second Berkeley Symp. on Math. Statist. and Prob.*, pages 481–492, Univ. of Calif., 1951.

[86] J. C. Lagarias, J. A. Reeds, M. H. Wright, and P. E. Wright. Convergence properties of the nelder-mead simplex method in low dimensions. *SIAM J. Optim.*, 9:112–147, 1998.

[87] Patrick Le Tallec and Moulay D. Tidriri. Application of maximum principles to the analysis of a coupling time marching algorithm. *J. Math. Anal. Appl.*, 229(1):158–169, 1999.

[88] W. K. Liu, T. B. Belytschko, and H. Chang. An arbitrary lagrangian-eulerian finite element method for path-dependent materials. *Computer Methods in Applied Mechanics and Engineering*, 58:227–245, 1986.

[89] W. K. Liu and J. Gvildys. Fluid- structure interaction of tanks with an eccentric cor barrel. *Computer Methods in Applied Mechanics and Engineering*, 58:51–57, 1986.

[90] W. K. Liu and D. Ma. Computer implementation aspects for fluid structure interaction problems. *Computer Methods in Applied Mechanics and Engineering*, 31:129–148, 1982.

[91] S. Manservisi. Numerical analysis of vanka-type solvers for steady stokes and navier-stokes flows. *SIAM Journal on Numerical Analysis*, 44(5):2025–2056, 2006.

[92] J. H. Mathews and K. K. Fink. *Numerical Methods Using Matlab*. Prentice-Hall Inc., New Jersey, USA, 2004.

[93] W. Maurel, Y. Wu, N. Magnenat Thalmann, and D. Thalmann. *Biomechanical models for soft tissue simulation*. ESPRIT basic research series. Springer-Verlag, Berlin, 1998.

[94] J. Molenaar. A two-grid analysis of the combination of mixed finite elements and vanka-type relaxation. In W. Hackbusch and U. Trottenberg, editors, *Multigrid Methods: Advances in Applied Mathematics and Mechanics*, volume 1, pages 313–323. Birkhï¿½user Verlag, 1991.

[95] J. A. Nelder and R. Mead. A simplex method for function minimization. *Computer Journal*, 7(4):308–313, 1965.

[96] W. F. Noh. A time-dependent, two-space dimensional coupled eulerian-lagrangian code. In B. Aldert, editor, *Methods in Computational Physics*, page 117. New York, 1964. Academic Press, 1964.

[97] D. H. Norrie. *The Finite Element method: Fundamentals and Applications*. Academic Press, 1973.

[98] R. W. Ogden. *Non-linear Elastic Deformations.* Springer-Verlag, Wiley, Chichester, U.K., 1987 (Dover reprint, 1997).

[99] A. Ouazzi and S. Turek. Efficient multigrid and data structures for edge oriented fem stabilization. In Enumath 2005, editor, *Numerical Mathematics and Advanced Applications*, pages 520–527. Springer, Berlin, ISBN-10 3-540-34287-7b, 2006.

[100] K. C. Park and C. A. Felippa. Partitioned analysis of coupled systems. In T. Belytschko and T. J. R. Hughes, editors, *Computational Methods for Transient Analysis*, page chapter 3. North-Holland, Amsterdam, New York, ISBN-10 3-540-34287-7., 1983.

[101] E. L. Peterson. The origins of geometric programming. *Annals of Operations Research*, 105:15–19, 2001.

[102] W. E. Pracht. Calculating three-dimensional fluid flows at all flow speeds with an eulerian-lagrangian computing mesh. *Journal of Computational Physics*, 17:132–159, 1975.

[103] A. Quarteroni. Modeling the cardiovascular system: a mathematical challenge. In B. Engquist and W. Schmid, editors, *Mathematics Unlimited - 2001 and Beyond*, pages 961–972. Springer-Verlag, 2001.

[104] A. Quarteroni, R. Sacco, and F. Saleri. *Numerical Mathematics*. Springer, 2000.

[105] A. Quarteroni, M. Tuveri, and A. Veneziani. Computational vascular fluid dynamics: Problems, models and methods. *Computing and Visualization in Science*, 2(4):163–197, 2000.

[106] Schmachtel. R. *Robuste Lineare und Nichtlineare Lösungsverfahren für die Inkompressiblen Navier–Stokes–Gleichungen*. PhD thesis, University of Dortmund, 2003.

[107] R. Rannacher and S. Turek. A simple nonconforming quadrilateral stokes element. *Numer. Methods Partial Differential Equations.*, 8:97–111, 1992.

[108] M. Razzaq, H. Damanik, J. Hron, A. Ouazzi, and S. Turek. Fem multigrid techniques for fluid-structure interaction with application to hemodynamics. *Applied Numerical Mathematics*, page accepted for publication, 2010.

[109] M. Razzaq, J. Hron, and S. Turek. Numerical simulation of laminar incompressible fluid-structure interaction for elastic material with point constraintst. In R. Rannacher and A. Sequeira, editors, *Advances in Mathematical Fluid Mechanics-Dedicated to Giovanni Paolo Galdi on the Occasion of his 60th Birthday*, pages 451–472. Springer, 2010.

[110] M. Razzaq, S. Turek, J. Hron, J. F. Acker, F. Weichert, I. Q. Grunwald, C. Roth, and B. F. Wagner, M . Romeike. Numerical simulation of fluid-structure interaction with application to aneurysm hemodynamics. In S. Hartmann, A. Meister, M. Schäfer, and S. Turek, editors, *Fluid-Structure Interaction. Theory, Numerics and Applications*, pages 215–230, Kassel, 2009.

[111] M. Razzaq, S. Turek, J. Hron, J. F. Acker, F. Weichert, I. Q. Grunwald, C. Roth, and B. F. Wagner, M . Romeike. Numerical simulation and benchmarking of fluid-structure interaction with application to hemodynamics. In G. P. Galdi and R. Rannacher, editors, *Fundamental Trends in Fluid-Structure Interaction*, volume 1 of *Contemporary Challenges in Mathematical Fluid Dynamics and its applications*, pages 171–199. World Scientific, 2010.

[112] J. B. Rosen. The gradient projection method for nonlinear programming. part i. linear constraints. *J. Soc. Indust. App. Math.*, 8(1):181–217, 1960.

[113] J. B. Rosen. The gradient projection method for nonlinear programming. part ii. linear constraints. *SIAM*, 9:414–432, 1961.

[114] Y. Saad. *Iterative Methods for Sparse Linear Systems*. SIAM, 2nd edition, 2000.

[115] P. A. Sackinger, P. R. Schunk, and R. R. Rao. A Newton-Raphson pseudo-solid domain mapping technique for free and moving boundary problems: a finite element implementation. *J. Comput. Phys.*, 125(1):83–103, 1996.

[116] M. Schäfer, D. C. Sternel, G. Becker, and P. Pironkov. Efficient numerical simulation and optimization of fluid-structure interaction. In H.-J. Bungartz, M. Mehl, and M. Schäfer, editors, *Fluid-Structure Interaction II: Modelling, Simulation, Optimisation*, volume 73 of *Lecture Notes in Computational Science and Engineering*, pages 131–158. Springer, 2010.

[117] J. Scheberl and W. Zulehner. On schwarz-type smoothers for saddle point problems. *Numerische Mathematik*, 95(2):377–399, 2003.

[118] A. Srikanth and N. Zabaras. An updated lagrangian +nite element sensitivity analysis of large deformations using quadrilateral elements. *Int. J. Numer. Meth. Engng.*, 52(1-2):1131–1163, 2001.

[119] T. E. Tezduyar, S. Sathe, T. Cragin, B. Nanna, B.S. Conklin, J. Pausewang, and M. Schwaab. Modeling of fluid structure interactions with the space time finite elements: Arterial fluid mechanics. *International Journal for Numerical Methods in Fluids*, 54:901–922, 2007.

[120] T. E. Tezduyar, S. Sathe, M. Schwaab, and B.S. Conklin. Arterial fluid mechanics modeling with the stabilized space time fluid structure interaction technique. *International Journal for Numerical Methods in Fluids*, 57:601–629, 2008.

[121] C. Treusdell. *A first course in rational continuum mechanics*, volume 1. Academic Press Inc., Boston, MA, second edition, 1991.

[122] S. Turek. *Efficient Solvers for Incompressible Flow Problems: An Algorithmic and Computational Approach*. Springer-Verlag, 1999.

[123] S. Turek and J. Hron. Proposal for numerical benchmarking of fluid-structure interaction between an elastic object and laminar incompressible flow. In H.-J. Bungartz and M. Schäfer, editors, *Fluid-Structure Interaction: Modelling, Simulation, Optimisation*, volume 53 of *Lecture Notes in Computational Science and Engineering*, pages 371–385. Springer, 2006.

[124] S. Turek, J. Hron, M. Mádlík, M. Razzaq, H. Wobker, and J. F. Acker. Numerical simulation and benchmarking of a monolithic multigrid solver for fluid-structure interaction problems with application to hemodynamics. In H.-J. Bungartz, M. Mehl, and M. Schäfer, editors, *Fluid-Structure Interaction II: Modelling, Simulation, Optimisation*, volume 73 of *Lecture Notes in Computational Science and Engineering*, pages 193–220. Springer, 2010.

[125] S. Turek, J. Hron, M. Razzaq, H. Wobker, and M. Schäfer. Numerical benchmarking of fluid-structure interaction: A comparison of different discretization and solution approaches. In H.-J. Bungartz, M. Mehl, and M. Schäfer, editors, *Fluid-Structure Interaction II: Modelling, Simulation, Optimisation*, volume 73 of *Lecture Notes in Computational Science and Engineering*, pages 413–424. Springer, 2010.

[126] S. Turek, L. Rivkind, J. Hron, and R. Glowinski. Numerical study of a modified time-steeping theta-scheme for incompressible flow simulations. *Journal of Scientific Computing*, 28:533–547, 2006.

[127] S. Turek and M. Schäfer. Benchmark computations of laminar flow around cylinder. In E.H. Hirschel, editor, *Flow Simulation with High-Performance Computers II*, volume 52 of *Notes on Numerical Fluid Mechanics*, pages 547–566. Vieweg, 1996. co. F. Durst, E. Krause, R. Rannacher.

[128] S. Turek and R. Schmachtel. Fully coupled and operator-splitting approaches for natural convection flows in enclosures. *International Journal for Numerical Methods in Fluids*, 40:1109–1119, 2002.

[129] A. Valencia, D. Ladermann, R. Rivera, E. Bravo, and M. Galvez. Blood flow dynamics and fluid–structure interaction in patient -specific bifurcating cerebral aneurysms. *International Journal for Numerical Methods in Fluids*, 58:1081–1100, 2008.

[130] S.P. Vanka. Implicit multigrid solutions of Navier-Stokes equations in primitive variables. *J. of Comp. Phys.*, 65:138–158, 1986.

[131] H. B. Veiga. On the existence of strong solutions to a coupled fluid structure evolution problem. *J. Math. Fluid Mech*, 6(1):21–52, 2004.

[132] R. P. Vito and S. A. Dixon. Blood vessel constitutive models-1995-2002. *Annual Review of Biomedical Engineering.*, 5:413–439, 2003.

[133] P. Wesseling and C. W. Oosterlee. Geometric multigrid with applications to computational dynamics. *Journal of Computational and Applied Mathematics*, 128(2):311–334, 2001.

[134] H. Wobker and S. Turek. Numerical studies of vanka-type smoothers in computational solid mechanics. In *Advances in Applied Mathematics and Mechanics*, volume 1, pages 29–55. Springer, 2009.

[135] K. Yasuda, R. C. Armstrong, and R. E. Cohen. Shear flow properties of concentrated solutions of linear and star branched polystyrenes. *Rheol. Acta.*, 20(2):163–178, 1981.

[136] G. Zoutendijk. *Methods of Feasible Directions: a study in linear and non-linear programming*. Elsevier Pub. Co, Amsterdam, 1960.